

# ***Waste Form Degradation Model Integration for Engineered Materials Performance***

## **Fuel Cycle Research & Development**

*Prepared for*  
**U.S. Department of Energy**  
**Used Fuel Disposition Campaign**  
*David C. Sassani, Louise J. Criscenti*  
*(Sandia National Laboratories)*  
*Peter Zapol*  
*(Argonne National Laboratory)*  
*Carl I. Steefel*  
*(Lawrence Berkeley National Laboratory)*  
*George S. Goff, David G. Kolman, Xiang-Yang Liu*  
*(Los Alamos National Laboratory)*  
*Christopher D. Taylor*  
*(Ohio State University)*  
*Peter C. Rieke, Joseph V. Ryan, Frances N. Smith*  
*(Pacific Northwest National Laboratory)*  
*Eunja J. Kim*  
*(University of Nevada, Las Vegas)*

**August 22, 2014**

**FCRD-UFD-2014-000051**

**SAND2014-18301 R**



**DISCLAIMER**

This information was prepared as an account of work sponsored by an agency of the U.S. Government. Neither the U.S. Government nor any agency thereof, nor any of their employees, makes any warranty, expressed or implied, or assumes any legal liability or responsibility for the accuracy, completeness, or usefulness, of any information, apparatus, product, or process disclosed, or represents that its use would not infringe privately owned rights. References herein to any specific commercial product, process, or service by trade name, trade mark, manufacturer, or otherwise, does not necessarily constitute or imply its endorsement, recommendation, or favoring by the U.S. Government or any agency thereof. The views and opinions of authors expressed herein do not necessarily state or reflect those of the U.S. Government or any agency thereof.

(Approved for UNCLASSIFIED UNLIMITED RELEASE)

Prepared by:  
Sandia National Laboratories  
Albuquerque, New Mexico 87185

Sandia National Laboratories is a multi-program laboratory managed and operated by Sandia Corporation, a wholly owned subsidiary of Lockheed Martin Corporation, for the U.S. Department of Energy's National Nuclear Security Administration under contract DE-AC04-94AL85000.



**APPENDIX E**  
**FCT DOCUMENT COVER SHEET <sup>1</sup>**

Name/Title of Deliverable/Milestone/Revision No. -- Waste Form Degradation Model Integration for Engineered Materials Performance / M2FT-14SN0804051/ Rev = initial (00)

Work Package Title and Number: Waste Form Degradation Modeling - SNL/ FT-14SN080405

Work Package WBS Number: 1.02.08.04

Responsible Work Package Manager: David Sassani/ 

Date Submitted: 08/22/2014

|  |   |                                |  |   |
|--|---|--------------------------------|--|---|
| Quality Rigor Level for Deliverable/Milestone <sup>2</sup> | <input checked="" type="checkbox"/> QRL-3 | <input type="checkbox"/> QRL-2 | <input type="checkbox"/> QRL-1<br>Nuclear Data | <input type="checkbox"/> Lab/Participant QA Program (no additional FCT QA requirements) |
|--|---|--------------------------------|--|---|

This deliverable was prepared in accordance with Sandia National Laboratories \_\_\_\_\_  
 (Participant/National Laboratory Name)

QA program which meets the requirements of  
 DOE Order 414.1     NQA-1-2000     Other

**This Deliverable was subjected to:**

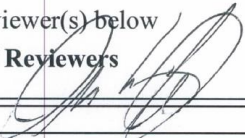
Technical Review

**Technical Review (TR)**

**Review Documentation Provided**

- Signed TR Report or,
- Signed TR Concurrence Sheet or,
- Signature of TR Reviewer(s) below

**Name and Signature of Reviewers**

Carlos Jove-Colon (SNL) 

Peer Review

**Peer Review (PR)**

**Review Documentation Provided**

- Signed PR Report or,
- Signed PR Concurrence Sheet or,
- Signature of PR Reviewer(s) below

**NOTE 1:** Appendix E should be filled out and submitted with the deliverable. Or, if the PICS:NE system permits, completely enter all applicable information in the PICS:NE Deliverable Form. The requirement is to ensure that all applicable information is entered either in the PICS:NE system or by using the FCT Document Cover Sheet.

**NOTE 2:** In some cases there may be a milestone where an item is being fabricated, maintenance is being performed on a facility, or a document is being issued through a formal document control process where it specifically calls out a formal review of the document. In these cases, documentation (e.g., inspection report, maintenance request, work planning package documentation or the documented review of the issued document through the document control process) of the completion of the activity, along with the Document Cover Sheet, is sufficient to demonstrate achieving the milestone. If QRL 1, 2, or 3 is not assigned, then the Lab / Participant QA Program (no additional FCT QA requirements) box must be checked, and the work is understood to be performed and any deliverable developed in conformance with the respective National Laboratory / Participant, DOE or NNSA-approved QA Program.

## AKNOWLEDGEMENTS

This work was supported by the U.S. Department of Energy Office of Nuclear Energy, through the Office of Used Nuclear Fuel Disposition Research and Development within the Office of Fuel Cycle Technologies.

The authors acknowledge our gratitude to William Ebert (ANL), Peter Swift (SNL), Kevin McMahon (SNL), John Vienna (PNNL), Carlos Jove-Colon (SNL), and Philippe Weck (SNL) for discussions on technical aspects and integration of this work. In addition, the authors thank Joseph Price (DOE NE-53), William Spezialetti (DOE NE-53), Prasad Nair (DOE NE-53), Mark Tynan (DOE NE-53), and Tim Gunther (DOE NE-53) for their discussions, oversight and guidance on topics covered in this report.

This report benefitted from internal technical review by Carlos Jove-Colon (Sandia National Laboratories).

## SUMMARY

The contributions presented in this report are being accomplished via a concerted effort among investigators at five national laboratories: SNL, ANL, LANL, LBNL, and PNNL and investigators at two universities (through LANL) OSU and UNLV. This collaborative approach to the glass and metallic waste form degradation modeling activities includes process model development (including first-principles approaches) and model integration—both internally among developed process models and between developed process models and PA models, and cross campaign integration between activities in the Used Fuel Disposition (UFD) Campaign and the Separations (to be Materials Recovery) and Waste Forms (SWF=>MRWF) Campaign. There is some experimental work within the UFD activities in the metallic waste form model development work at LANL. Figures S-1 and S-2 depict summary schematics of the major models, experimental studies, and their primary connections to each other both within the UFD Campaign (shown as solid outline shapes) and in the SWF Campaign (dashed outline shapes), which is executing both extensive experimental investigations and development of models for the integrated post-closure behavior of glass and metallic waste forms. Also shown are the major outputs that are expected to be integrated into performance assessment (PA) models as a result of this work within the SWF (MRWF) Campaign.

The primary outputs of these activities provide essential connections into the PA models. The primary output connection is the fractional degradation rate (FDR) of the waste forms. Within the current PA models, this parameter is sampled from a distribution of reported values in the literature, but would be generated directly from the process-based models developed within the SWF (MRWF) Campaign. In addition, depending on the fidelity of the waste form degradation models, additional parametric couplings for chemical effects would be constructed between the PA model and the waste form degradation models to account for their effects on bulk chemistry within a breached waste package.

Underpinning the continuum modeling approaches are experimental studies and first principles models of glass waste form and metallic waste form degradation and the major corrosion products expected from these processes (e.g., gel and secondary phases such as clays and zeolites for glass waste forms, oxides and oxyhydroxides for metallic waste forms). In addition to providing conceptual guidance to the modeling approaches, the experimental programs provide validation data for the conceptual models and parametric constraints for improving the modeling tools. Detailed mechanistic processes have also been investigated using first principles molecular scale modeling for glass and metallic waste forms and some of the common corrosion products. Such work also provides methods for predicting reaction energetics and activation energies where data are lacking, and can provide insight and validation for processes being incorporated into detailed models.

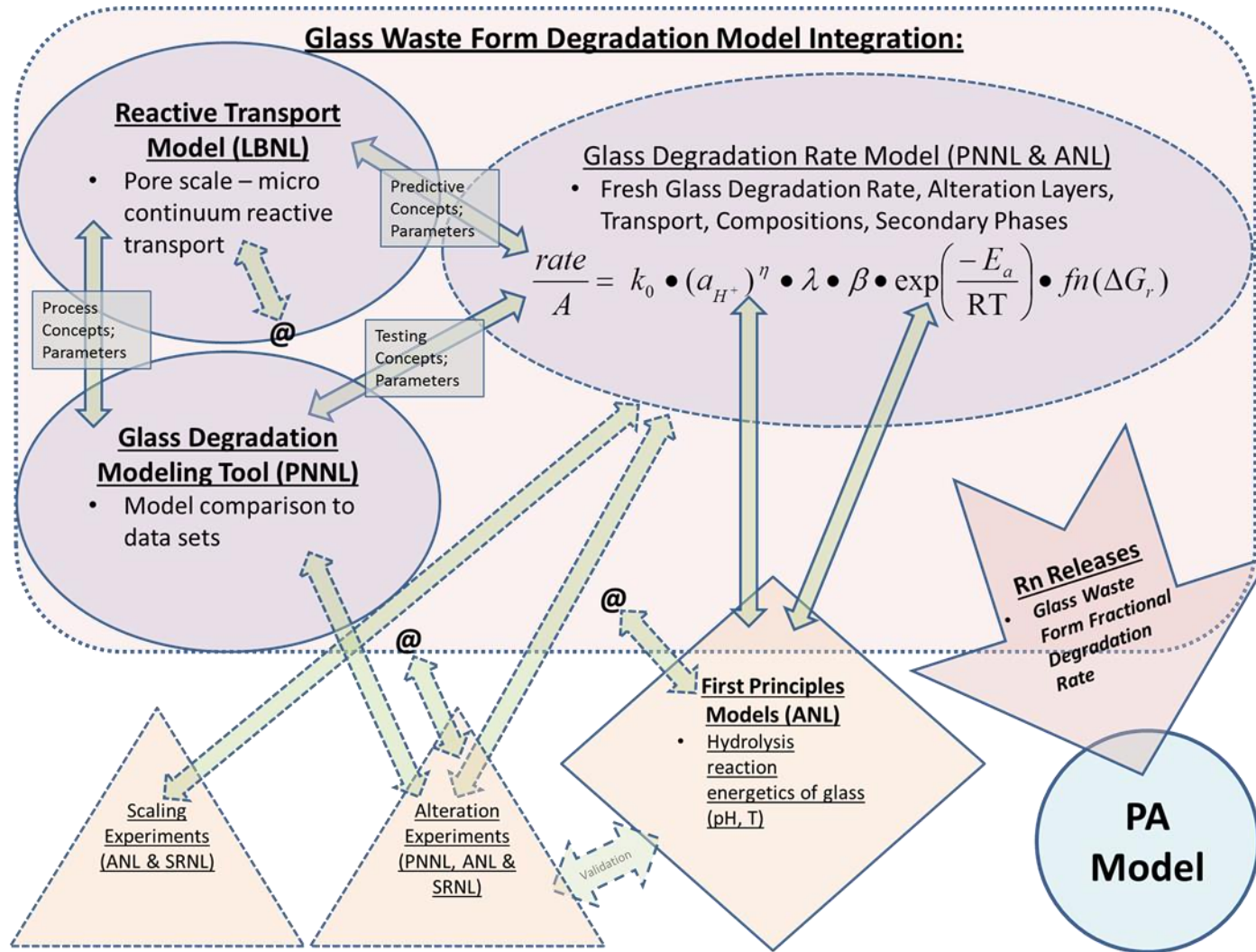


Figure S- 1. Schematic showing the three glass waste form degradation process modeling activities in the FY14 UFD Campaign (shapes with solid outlines and related MRWF Campaign activities (modeling and experiments shown in shapes with dashed outlines).

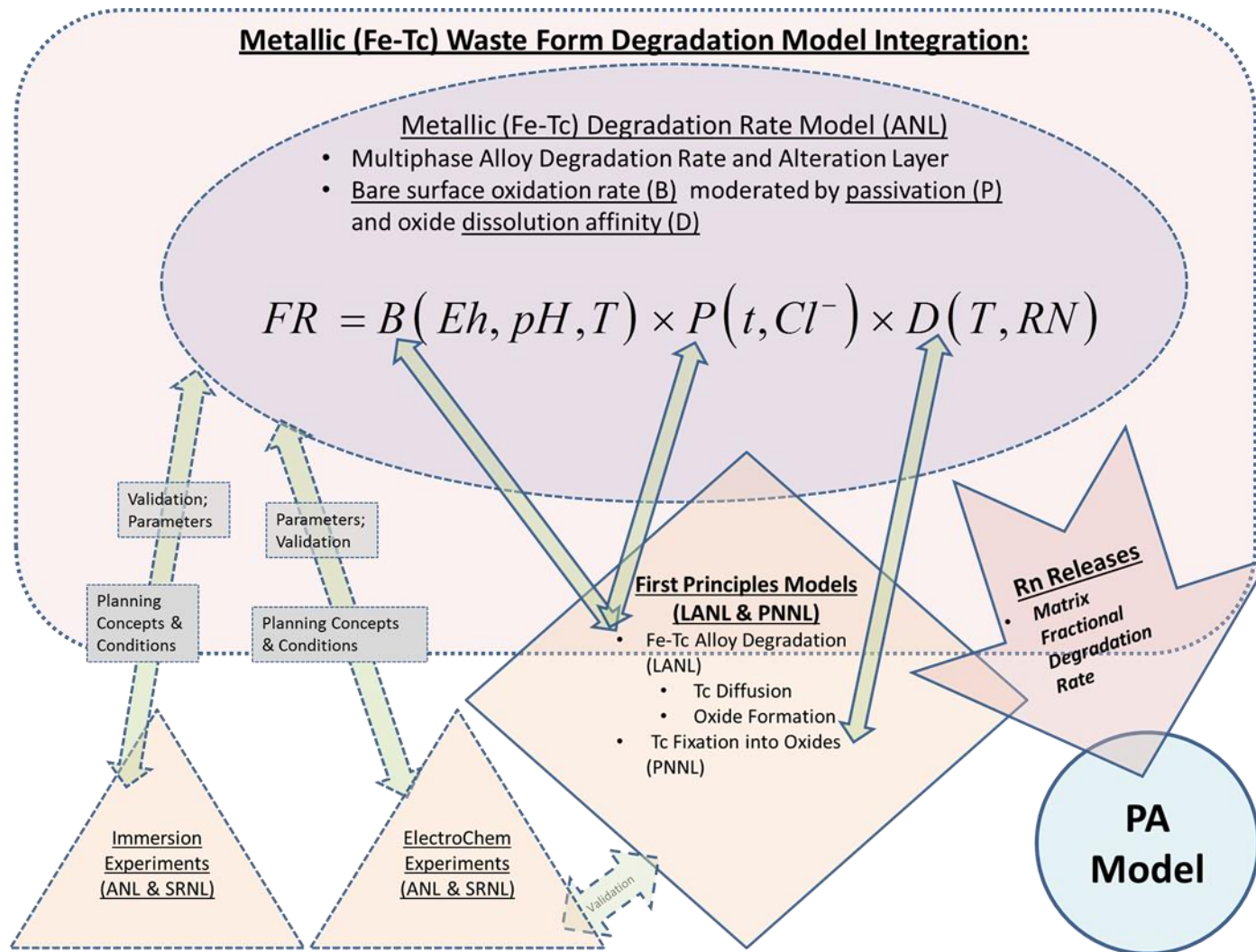


Figure S- 2. Schematic showing the metallic (Fe-Tc) waste form degradation modeling activities in the FY14 UFD Campaign (shapes with solid outlines) and related MRWF Campaign activities (modeling and experiments shown in shapes with dashed outlines).

## Results and Discussion

The activities for glass degradation modeling encompass scales from the molecular to the macroscale for evaluating the breakdown of the glass phase, the development of silica gel at the glass-water interface, and the formation of alteration phases at this interface. These activities are evaluating several different rate laws that have been proposed for these processes based on fitting experimental data and that are currently used to predict corrosion rates into the distant future in repository settings. In general, these rate laws base their limiting rates on either a transition state theory (TST) dissolution affinity rate law or on the rate of mass transport through the amorphous layers formed at the glass-water interface. The lack of a consensus on an integrated quantitative representation of the rate-limiting processes for nuclear waste glass degradation initiated an effort to evaluate these processes in greater detail to enhance the technical bases for glass degradation rate models used in performance assessment of geologic disposal systems.

Molecular-scale first-principles modeling work focuses on calculating the energies and barriers for bond-breaking reactions involving Si-O and B-O bonds at the glass surface. This research effort is designed to develop a more complete constitutive expression for the TST affinity rates based on multicomponent glass surface structure. Reaction barriers and energies for dissolution reactions on protonated, neutral, and deprotonated sites on sodium borosilicate glass surfaces were calculated and reported. For these simple three component glasses ( $\text{Na}_2\text{O} - \text{B}_2\text{O}_3 - \text{SiO}_2$ ), there are only two framework metals (B and Si). However, there are numerous reactions occurring on the surface with different activation barriers and reaction energies depending on the bond saturation state of the B (or Si) atom being removed from the surface, the type and saturation state of the neighboring metal (B or Si) bonded to the same bridging oxygen atom, and the protonation state of the bridging oxygen. Key results of this work include:

- Predicted energies for 22 different surface reactions that play a role in  $\text{Na}_2\text{O}-\text{B}_2\text{O}_3-\text{SiO}_2$  glass dissolution.
- Developed a methodology to resolve discrepancies in bulk reaction energetics that exist in the literature because simple affinity rate laws have been derived from bulk experimental dissolution data, even though different reactions may become rate-limiting for different glass or solution compositions.

Nano-continuum ( $\text{K}\mu\text{C}$ ) modeling focuses on reproducing the nanoscale concentration profiles at the glass-water interface observed for a 25-year degradation experiment for the French SON68 glass. A high resolution model of that interface is developed with a constant grid spacing of 1 nanometer and a continuum model assumption. Although using a continuum model at the nanometer scale is an approximation, it is the only approach available that includes multicomponent chemistry with precipitation and dissolution at this scale. Using this model the compositional gradients reproduced in qualitative and semi-quantitative terms are: (1) Li release from the glass; (2) hydrogen migration into the glass (glass hydration) from the solution and (3) boron release from the glass. The  $\text{K}\mu\text{C}$  model incorporates the possible rate-controlling processes of (a) diffusion-limited glass corrosion, (b) affinity-controlled hydrolysis reactions based on TST rate laws, and (c) precipitation of secondary phases. Results of this work include:

- A key aspect of the  $\text{K}\mu\text{C}$  model is that the primary dissolution reaction of the fresh glass is assumed to follow an affinity rate law, with a cubic dependence on the solution saturation state with amorphous silica. This approach reproduced the sharpness of the B release front and the position of the B release front outside of the Li-H interdiffusion front.
- The simulations predict a linear rate of front propagation over time once the initial period has passed. Sensitivity analyses with the  $\text{K}\mu\text{C}$  model indicate that the amount of glass degradation that occurs is dependent on the fluid compositional boundary condition. Virtually no corrosion of the glass was calculated for amorphous silica saturated fluid ( $1936 \mu\text{M}$ ) as the boundary condition versus the  $10 \mu\text{M}$  composition that results in much larger glass degradation.

- The rate-limiting step for the experiment on SON68 glass corrosion appears to be the rate of diffusion of H (via water) into the pristine glass. An explicit Passive Reactive Interface (PRI) zone is not required. The linear rate that is predicted by the simulations follows from the fact that the amorphous silica gel corrosion layer that forms on the glass is not itself a diffusion barrier, consistent with the constant width of the layer.

The Glass Corrosion Modeling Tool (GCMT) has been developed for several purposes: (1) to examine efficiently the goodness of fit of a variety of glass corrosion models to specific experimental datasets, (2) to provide easy access and evaluation of an extensive database of glass alteration experimental results (consisting primarily of single pass flow through tests—i.e., the ALTGLASS database), with the potential to use this database to derive new glass dissolution constitutive equations, and (3) to provide a platform for the newly developed Diffusive Chemical Reaction (DRCx) model. The DRCx model, like the  $K_{\mu}C$  model, is intended to be used to evaluate the detailed concentration profiles dataset from TOF-SIMS and APT analyses of glass corrosion interfaces. Within the GCMT, the user can choose to implement various other models such as the Aagaard-Helgeson (AH) model with residual rate, the Grambow-Muller (GM) model and the Glass Reactivity with Allowance for the Alteration Layer (GRAAL) model. Key results from this work include:

- A graphical user interface has been constructed for use within the GCMT so that selection of datasets from the ALTGLASS database (being developed at Savannah River National Laboratory by Carol Jantzen) is a streamlined and transparent process.
- Initial GCMT model results using the DRCx model show that, for the TOF-SIMS data on SON68 glass degradation, the DRCx model adequately describes Na, Si, and B profiles but is less useful for describing the behavior of Al and Li.
- Two detailed examples of using the GCMT to evaluate glass corrosion datasets have been generated. In the first example, the long-term residual rate corrosion of low-activity waste (LAW) glass are analyzed using the AH model and optimized parameters are provided. In the second example, time dependent species concentrations for SON68 glass degradation are analyzed with the GRAAL model. Although the GRAAL model does not provide a close approximation to the specific dataset used in the example, it has been used to closely reproduce other relevant experimental data.

A multistep conceptual corrosion model for the release of Tc from any candidate alloy (e.g., Fe-Tc) waste form is described. There are three viable rate-limiting mechanisms for Tc release: (1) cation vacancy annihilation at the metal/oxide interface, (2) transport of Tc through the oxide film, and (3) dissolution of Tc at the oxide/environment interface. Initial molecular-scale first-principles modeling has focused on applying DFT calculations to investigate the relative stability of different Fe-Tc oxides and the diffusion of Tc incorporated into vacancy defect sites in a range of Fe-oxide crystals. To validate the DFT approach used, the relative stabilities of Tc oxides were calculated and predicted properties were compared to measured values. To evaluate potential behavior of Tc in oxide films of a corroding alloy, models of Fe-oxide structures were designed with care to incorporate the magnetic ordering of the Fe atoms. Calculations of the energies for Tc incorporation into simple Fe vacancies in three Fe-oxide crystal structures were completed. In addition, for the first time, the migration energy barrier for Tc diffusion along one channel in  $\alpha$ -Fe<sub>2</sub>O<sub>3</sub> (hematite) was calculated. Finally, calculations in which Tc was incorporated into three spinel phases (potential waste forms) of different crystal structures (Fe<sub>3</sub>O<sub>4</sub>, CaFe<sub>2</sub>O<sub>4</sub>, and YFe<sub>2</sub>O<sub>4</sub>) evaluated the most stable form to host Tc. Integrating modeling efforts focused on larger-scale simulations using kinetic Monte Carlo and force field methods. Preliminary results suggest that the corrosion morphologies and rates would be different for Tc-Fe, Tc-Mo, and Tc-Ni candidate alloy waste forms. The rate of Tc-Fe corrosion decreases with increasing Tc concentration up to 10%. Finally, integrated with the modeling effort, electrochemical corrosion experimental studies have been performed on Tc metal in pH 3.2 H<sub>2</sub>SO<sub>4</sub> solutions. Several experiments were performed to determine if a

passivating film forms on Tc metal, but so far all measurements suggest the films formed are not passivating. Key results of this metallic waste form modeling work include:

- The two oxides ( $\text{TcO}_2$  and  $\text{Tc}_2\text{O}_7$ ) calculated to be the most stable are the only two Tc oxides that have been synthesized and characterized experimentally. Calculated lattice constants, crystal formation energies, and bulk moduli compared reasonably well to experimental measurements.
- The calculated results show that Tc incorporation into FeO is endothermic, Tc incorporation into  $\alpha\text{-Fe}_2\text{O}_3$  is energetically preferred, and the preference for Tc incorporation into  $\text{Fe}_3\text{O}_4$  is site dependent.
- The energy barrier for Tc migration via vacancies is calculated to be larger than for Fe, suggesting slower Tc diffusion than Fe diffusion within hematite.
- Prediction that magnetite is the most stable form to host Tc atoms with concentrations of up to 33%, forming a  $\text{TcFe}_2\text{O}_4$  spinel.
- Kinetic Monte Carlo calculations suggest that the corrosion morphologies and rates would be different for Tc-Fe, Tc-Mo, and Tc-Ni candidate alloy waste forms and that the rate of Tc-Fe corrosion decreases with increasing Tc concentration (up to 10%).

Additional molecular-scale first-principles modeling work is focused on investigating the incorporation of Tc into an iron oxyhydroxide (goethite,  $\alpha\text{-FeOOH}$ ) phase that could represent oxidized corrosion products of the metallic waste form or those of the waste package internal components. These calculations also constrain Tc affinity for bulk goethite versus goethite surface sites, and determining Tc stability on (in) goethite in the presence of adsorbates such as water, oxygen, hydrogen and hydrogen peroxide. The method used to date is unrestricted Hartree Fock (UHF), which should successfully capture the localized electron behavior in goethite. Three different Tc incorporation schemes are proposed: (1) coupled Tc(IV)/Fe(II) substitution for two lattice Fe(III), (2) Tc(IV) substitution of one Fe(III) and one  $\text{H}^+$  balance, and (3) interstitial Tc(IV) addition and removal of four nearest neighbor  $\text{H}^+$  for charge balance. The energetics for these three schemes is under investigation. Results for this work include:

- Established appropriate calculation parameters to assure that the goethite structure used is antiferromagnetic
- Created supercells that allow Tc incorporation at experimentally-relevant levels.

Development of an idealized strategy for integrating glass and metallic waste forms degradation process models with PA model to analyze generic disposal environments includes parametric connections/couplings needed for direct incorporation into PA models. This is based in the methodology developed for integration of the used fuel degradation model into the PA model. The approach begins with basic physical parameter couplings from the PA model with fractional degradation rate feedback to the PA model. However, it is an ongoing task to delineate in the implementation specifics of how these process models will couple to other EBS process submodels (e.g., chemical environment evolution, radionuclide transport) within the PA model for generic disposal environments and evaluations of the safety case. Additional more idealized coupling options are outlined that have fewer open constraints on implementation specifics and provide flexible options for incorporating additional coupling detail as needed.

Future integration of this work into PA models within the UFD Campaign will focus on cross Campaign collaboration with the SWF (MRWF) Campaign, where work in these process model areas and for models developed for use in PA models will continue into the next fiscal year and beyond. The enhanced integration within these process model areas and across campaigns with management and technical staff will prove invaluable in future efforts to integrate glass and metallic waste form degradation models into UFD Campaign PA models as efficiently as possible.

## CONTENTS

|   |     |
|---|-----|
| SUMMARY .....   | iii |
| 1. INTRODUCTION .....   | 1   |
| 1.1 Waste Form Degradation Models .....   | 1   |
| 1.1.1 Glass Waste Form Degradation Activities .....   | 1   |
| 1.1.2 Metallic Waste Form Degradation Activities .....  | 3   |
| 1.2 Integration with Performance Assessment Models .....  | 6   |
| 2. Glass Waste Form Degradation Modeling .....  | 7   |
| 2.1 Molecular-Scale First-Principles Modeling .....   | 7   |
| 2.1.1 MODELING APPROACHES .....   | 8   |
| 2.1.2 REACTION ENERGIES AND BARRIERS IN BOROSILICATE GLASS .....  | 9   |
| 2.1.3 CONCLUSIONS AND RECOMMENDATIONS .....   | 13  |
| 2.1.4 References .....  | 14  |
| 2.2 Pore-(Nano-)Scale Continuum Modeling .....  | 16  |
| 2.2.1 SUMMARY OF 25 YEAR FRENCH GLASS SON68 LEACHING<br>EXPERIMENT .....                                    | 16  |
| 2.2.2 KINETIC-MICROSCOPIC-CONTINUUM MODEL ( $K_{\mu C}$ ) .....   | 17  |
| 2.2.3 MODEL SETUP FOR 25 YEAR FRENCH GLASS EXPERIMENT .....   | 18  |
| 2.2.4 SIMULATION RESULTS .....  | 20  |
| 2.2.5 DISCUSSION .....  | 23  |
| 2.2.6 References .....  | 25  |
| 2.3 Glass Degradation Modeling Tool .....   | 26  |
| 2.3.1 Development of a GUI for the ALTGLASS database .....  | 26  |
| 2.3.2 Addition of Depth Profile Databases .....   | 27  |
| 2.3.3 Formulation of a Model to Predict Depth Profile Data .....  | 27  |
| 2.3.4 Modeling Depth Profiling Data .....   | 29  |
| 2.3.5 Examples of GCMT Uses .....   | 31  |
| 2.3.6 References .....  | 37  |
| 3. Metallic Waste Form Degradation Modeling .....   | 38  |
| 3.1 Fe-Tc Waste Form Modeling and Experiments .....   | 38  |
| 3.1.1 Predictive multistep model for the release of Tc from passive metal alloy<br>waste forms .....        | 38  |
| 3.1.2 Density functional theory modeling of Tc incorporation and transport in<br>intermetallic oxides ..... | 42  |
| 3.1.3 Atomistic scale modeling of Tc corrosion .....  | 48  |
| 3.1.4 Electrochemical Corrosion Studies for Modeling Metallic Waste Form<br>Release Rates .....             | 50  |
| 3.1.5 Summary and Discussion .....  | 55  |

---

|       |   |    |
|-------|---|----|
| 3.1.6 | References.....   | 56 |
| 3.2   | Modeling of Tc Incorporation into Fe-oxyhydroxides.....               | 59 |
| 3.2.1 | Methods.....  | 59 |
| 3.2.2 | Results.....  | 63 |
| 3.2.3 | Discussion.....   | 66 |
| 3.2.4 | References.....   | 69 |
| 4.    | Integrating Waste Form Models into Performance Assessment Models..... | 71 |
| 4.1   | General Approach.....   | 71 |
| 4.2   | Connections to other Processes in the PA Model.....                   | 74 |
| 4.3   | References.....   | 77 |
| 5.    | Summary and Conclusions.....  | 78 |
| 5.1   | Glass Waste Form Modeling Activities.....                             | 78 |
| 5.2   | Metallic Waste Form Modeling Activities.....                          | 80 |
| 5.3   | Waste Form Model Integration into PA Models.....                      | 81 |

## FIGURES

|  |    |
|--|----|
| Figure 1.1-1. Schematic showing the three glass waste form degradation process modeling activities in the FY14 UFD Campaign (shapes with solid outlines): First Principles Models (ANL); Reactive Transport (micro-continuum) Model (LBNL); and Glass Degradation Modeling Tool (PNNL). Also shown are MRWF Campaign activities (modeling and experiments shown in shapes with dashed outlines) and the primary interfacing of those with the UFD glass waste form process modeling activities, and the major handoff into the UFD Campaign PA Model. Note that additional detailed activity connections within the MRWF Campaign activities are not shown here for simplicity. .... | 4  |
| Figure 1.1-2. Schematic showing the metallic (Fe-Tc) waste form degradation First-Principles Models (LANLA & PNNL) modeling activities in the FY14 UFD Campaign (shape with solid outlines-note that there is an experimental component to the LANL activities). Also shown are MRWF Campaign activities (modeling and experiments shown in shapes with dashed outlines) and the primary interfacing of those with the UFD metallic waste form process modeling activities, and the major handoff into the UFD Campaign PA Model. Note that additional detailed activity connections within the MRWF Campaign activities are not shown here for simplicity. ....                     | 5  |
| Figure 2.1-1. Schematic illustration of the hydrolysis reactions at the <sup>3</sup> B-O-Si bridge under (a) acidic (protonated), (b) neutral, and (c) basic (deprotonated) conditions. Boxes illustrate reaction steps calculated using DFT. ....   | 9  |
| Figure 2.1-2. Schematic illustration of the hydrolysis reactions at the 3B-O-3B bridges under (a) acidic (protonated), (b) neutral, and (c) basic (deprotonated) conditions. Boxes illustrate reaction steps calculated using DFT. ....  | 10 |
| Figure 2.1-3. Optimized initial, transition and final state geometries along the hydrolysis reaction pathway at the Si-O-Si bridges under acidic (protonated) conditions. ....   | 11 |
| Figure 2.1-4. Optimized initial, transition and final state geometries along the hydrolysis reaction pathway at the Si-O-Si bridges under neutral conditions. ....   | 12 |
| Figure 2.1-5. Optimized initial, transition and final state geometries along the hydrolysis reaction pathway at the Si-O-Si bridges under acidic (protonated) conditions. ....   | 13 |
| Figure 2.2-1. Experimental setup for the 25 year SON68 glass leaching experiment (Guittonneau et al., 2011) .....  | 17 |
| Figure 2.2-2. Schematic of modeling setup showing nanometer-scale reaction and diffusion zones. ....   | 20 |
| Figure 2.2-3. Figure 3: Schematic of the disposition of elemental leaching zones based on atom probe tomography (from Gin et al., 2013).....   | 20 |
| Figure 2.2-4. High resolution concentration profiles of elemental abundance across the pristine glass-hydrated glass interface (from Gin et al., 2013). ....   | 21 |
| Figure 2.2-5. Simulation results using the K $\mu$ C model. Note the position of the B release front further from the pristine glass than the Li-H interdiffusion front, in qualitative agreement with the observations. ....  | 21 |
| Figure 2.2-6. Simulated corrosion front position versus time. Note the linear (constant) rate of front propagation. ....   | 22 |
| Figure 2.2-7. Simulated distribution of amorphous silica reaction product at 2 and 5 years.....  | 22 |

|  |    |
|--|----|
| Figure 2.2-8. Schematic of modeling setup showing nanometer-scale reaction and diffusion zones used in comparative silica boundary condition simulations (see Figure 2.2-9).....   | 22 |
| Figure 2.2-9. Effect of silica concentration in external fluid at 3 years. In these simulations, the glass coupon begins at 50 nm (Figure 8), which indicates that almost no glass corrosion is predicted when the external solution is at saturation with amorphous silica. ....  | 23 |
| Figure 2.3-1. Proposed chemical reaction model and fit of that model to TOF-SIMS glass corrosion data (see Gin et al., 2013 for data).....   | 29 |
| Figure 2.3-2. Layer thickness and solution concentration for $Q/V = 1e-8$ [1/s]. ....  | 30 |
| Figure 2.3-3. Plots obtained from example of optimizing the AH model against selected LAWA44 data.....   | 32 |
| Figure 2.3-4. Example of output plot for optimization of Exp_12 data to the GRAAL model. ....  | 35 |
| Figure 3.1-1. Schematic of multistep processes in metal alloy waste form corrosion. ....   | 39 |
| Figure 3.1-2. Crystalline structures of binary Tc oxides: (a) TcO, (b) TcO <sub>2</sub> , (c) TcO <sub>3</sub> , and (d) Tc <sub>2</sub> O <sub>7</sub> . The grey and red spheres represent Tc and O atoms, respectively. ....  | 43 |
| Figure 3.1-3. Supercell structures used in defects calculations (a) FeO, (b) $\alpha$ -Fe <sub>2</sub> O <sub>3</sub> , (c) Fe <sub>3</sub> O <sub>4</sub> . Small red balls are oxygen atoms, large blue and green balls are Fe atoms with spin up and spin down, respectively.....   | 44 |
| Figure 3.1-4. Supercell structure in DFT calculation of Tc migration to a nearby Fe vacancy site in $\alpha$ -Fe <sub>2</sub> O <sub>3</sub> . Small red balls are oxygen atoms, and large blue and green balls are Fe atoms with spin up and spin down, respectively. ....  | 45 |
| Figure 3.1-5. Crystalline structures of Tc-Fe-O in (a) cubic (Fd-3m, 227), (b) orthorhombic (Cmcm, 63), and (c) rhombohedral (R-3m, 166) lattices. The gold, grey, and red spheres represent Fe, Tc, and O atoms, respectively. ....   | 46 |
| Figure 3.1-6. Total energies of TcFe <sub>2</sub> O <sub>4</sub> in cubic (Fd-3m), orthorhombic (Cmcm), and rhombohedral phases with respect to Tc concentration. The unit of the energy is eV per formula unit (eV/f.u.).....   | 47 |
| Figure 3.1-7. Compressibility of magnetite. The experimental data were taken from Klotz et al. (2006).....   | 47 |
| Figure 3.1-8. Corrosion morphologies obtained as outputs after the simulation of 1000 dissolution events for candidate alloy waste forms.....  | 49 |
| Figure 3.1-9. Average corrosion rate versus Tc composition for Tc-Fe, Tc-Mo, and Tc-Ni.....  | 49 |
| Figure 3.1-10. Open circuit potential data following 4 hour exposure to pH 3.2 H <sub>2</sub> SO <sub>4</sub> . Black line – from Cartledge and Smith (1955 ). Red line – from Cobble et al. (1953). Dashed line marked (a) represents the cathodic H <sub>2</sub> formation half reaction and dashed line marked (b) represents cathodic H <sub>2</sub> O formation half reaction. .... | 51 |
| Figure 3.1-11. Top - Anodic polarization curves for Tc exposed to pH 3.2 H <sub>2</sub> SO <sub>4</sub> solution. Bottom - selected return scans.....  | 52 |
| Figure 3.1-12. Anodic and cathodic potentiodynamic polarization data. Solid lines are tests using conventionally prepared samples. The heavy dashed line is a sample abraded <i>in-situ</i> at -0.3V <sub>NHE</sub> . ....   | 53 |

- Figure 3.1-13. Electrochemical impedance data (Nyquist (left), Bode magnitude (right top) and Bode phase angle (right bottom)) at potentials that correlate to Tc,  $Tc^{+4}$  and  $Tc^{+7}$  regions of stability. Sample was abraded at  $-0.5V_{NHE}$ . ..... 53
- Figure 3.1-14. Results from fitting of EIS data using the circuit model shown at the top left. OCP (open circuit potential) line is also labeled. .... 54
- Figure 3.2-1. Schematic illustrating one possible charge-compensated substitution scheme where Tc(IV) and Fe(II) replace two lattice Fe(III) in bulk goethite. Blue rectangular prisms represent pure bulk goethite (left) and bulk goethite with substituted impurities (right). The right-hand side is the “Products” and the left-hand side is the “Reactants”. ..... 61
- Figure 3.2-2. A single unit cell of goethite looking down the c axis. Purple spheres are iron, red spheres are oxygen, and white spheres are hydrogen. A scale bar is included for reference. .... 62
- Figure 3.2-3. Four different magnetic structures for goethite represented by a single unit cell: a) ferromagnetic (all Fe(III) are spin up); b) anti-ferromagnetic (edge sharing Fe(III) octahedra have opposite spins); c) anti-ferromagnetic prime (edge-sharing Fe(III) octahedra have the same spin); and d) anti-ferromagnetic double-prime (edge-sharing Fe(III) octahedra have opposite spins; corner sharing Fe(III) octahedra have the same spin). Purple spheres are Fe(III) (spin up), aqua spheres are Fe(III) (spin down), red spheres are O, and white spheres are H. .... 63
- Figure 3.2-4. Goethite supercells ( $3 \times 3 \times 3$ ) representing the anti-ferromagnetic (AFM) spin structure illustrating three different Tc(IV) substitution schemes: a) coupled Tc(IV) (green) / Fe(II) (yellow) substitution for two lattice Fe(III); b) Tc(IV) substitution of one lattice Fe(III) and removal of one  $H^+$  for charge balance; and c) interstitial Tc(IV) addition to the supercell and removal of four nearest-neighbor  $H^+$  for charge balance. A 20 Å scale-bar is included for reference. Purple spheres are Fe(III) (spin up), aqua spheres are Fe(III) (spin down), red spheres are  $O_2^-$ , and white spheres are  $H^+$ ; additionally, green spheres are Tc(IV) spin up and yellow spheres are Fe(II) spin down. .... 66
- Figure 3.2-5. Schematic illustrating how “Metal Corrosion Mechanisms” research at PNNL, LANL, and UNLV contributes to a conceptual model describing fractional release (FR) of radionuclides from MWF. .... 67
- Figure 3.2-6. Schematic illustrating different processes that contribute to an overall understanding of radionuclide source terms for a generic disposal system. The individual “Process Models,” including inventory, waste form, and waste package degradation processes, ultimately feed into the radionuclide source term as part of a “Probabilistic Assessment” (PA) Model (from Freeze et al., 2013, Figure 2-11). .... 68
- Figure 4.1-1. Features and phenomena to be represented in the PA model of a generic disposal system. .... 72
- Figure 4.1-2. Disposal system integrated process model capabilities in codes for the PA model (Freeze et al. 2013). .... 72
- Figure 4.1-3. Schematic example of an idealized chronological evolution of the thermal, hydrologic, mechanical, and chemical (THMC) conditions for a generic shale/argillite disposal environment. Percentages in the hydrological part of the diagram represent percent of water saturation in the media. .... 73
- Figure 4.2-1. Schematic diagram showing the range of possible couplings between the glass waste form, or metallic waste form, degradation model and the other models within the

engineered barrier system (EBS) portion of the PA Model. Primary hand-offs/connections are shown with single-headed arrows. Note that initial connection into the PA Model would be expected to be simply via the fractional degradation rate of the waste form. Potential two-way hand offs (i.e., couplings) are shown with double-headed arrows ..... 76

## TABLES

|  |    |
|--|----|
| Table 2.1-1. Calculated activation barriers $E_a$ and reaction energies $E_{rxn}$ (in kJ/mol) for dissolution reactions at borosilicate glass surface. ....  | 10 |
| Table 2.1-2. Reaction barriers and energies for bond breaking at protonated Si(Q <sub>n</sub> )-O-Si(Q <sub>m</sub> ) bridge (kJ/mol). ....  | 11 |
| Table 2.1-3. Reaction barriers and energies for Si-O-Si bond breaking (kJ/mol) in neutral case .....   | 12 |
| Table 2.1-4. Reaction barriers and energies for Si-O-Si bond breaking (kJ/mol) in basic (deprotonated) case .....  | 13 |
| Table 3.1-1. Structural properties of Tc, TcO <sub>2</sub> and Tc <sub>2</sub> O <sub>7</sub> . Units are in Å and eV per formula unit (eV/f.u) for the lattice constants and formation energy, respectively. Experimental values are from references: a: Kittel, 1996, b: Muller et al., 1964; Lemire and Jobe, 1996, and c: Muller et al., 1964; Krebs, 1969. .... | 43 |
| Table 3.1-2. Spin-polarized PAW-PBE DFT calculated relative energy for different Fe vacancies, and Tc incorporation energy at available Fe vacancy sites in FeO, α-Fe <sub>2</sub> O <sub>3</sub> , and Fe <sub>3</sub> O <sub>4</sub> . ....  | 45 |
| Table 3.1-3. Lattice constant and bulk modulus of magnetite. Units are in Å and GPa for the lattice constant and bulk modulus, respectively. ....  | 47 |
| Table 3.2-1. Total energy versus k-point density in a single, ferromagnetic (FM) goethite unit cell. ....  | 60 |
| Table 3.2-2. Number and type of each atom in a goethite supercell when increasing dimensions by n × n × n unit cells. ....   | 62 |
| Table 3.2-3. Single-point energy versus geometry optimized calculations for single goethite unit cells with different magnetic ordering on the iron sub-lattice. ....  | 64 |

## ACRONYMS AND ABBREVIATIONS

|          |   |
|----------|---|
| AFM      | Anti-Ferromagnetic  |
| AFM-P    | Anti-Ferromagnetic Prime  |
| AFM-DP   | Anti-Ferromagnetic Double Prime   |
| AH       | Aagaard-Helgeson  |
| ALTGLASS | Glass corrosion database prepared by Savannah River National Laboratory |
| ANL      | Argonne National Laboratory   |
| APT      | Atom Probe Tomography   |
| DFT      | Density Functional Theory   |
| DOE      | United States Department of Energy                                      |
| EBS      | Engineered Barrier System   |
| FCRD     | Fuel Cycle Research & Development                                       |
| FM       | Ferromagnetic   |
| FR       | Fractional Release  |
| GCMT     | Glass Corrosion Modeling Tool   |
| GGA      | Generalized Gradient Approximation                                      |
| GM       | Grambow-Muller  |
| GOPT     | Geometry optimized  |
| GRAAL    | Glass Reactivity with Allowance for the Alteration Layer                |
| KMC      | Kinetic Monte Carlo   |
| LANL     | Los Alamos National Laboratory  |
| LAW      | Low Activity Waste  |
| LDA      | Local Density Approximation   |
| MC       | Monte Carlo   |
| MD       | Molecular Dynamics  |
| MWF      | Metallic Waste Form   |
| NE       | Nuclear Energy  |
| PAW      | Projector Augmented Wave (potentials)                                   |
| PBE      | Perdew-Burke-Ernzerhof (functional)                                     |
| PDE      | Partial Differential Equation   |
| PEST     | Parameter Estimation Software Package                                   |
| PIC      | PNNL Institutional Computing  |
| PCT      | Product Consistency Test  |

---

|          |  |
|----------|--|
| PNNL     | Pacific Northwest National Laboratory  |
| PRI      | Passivating Reactive Interface   |
| PUF      | Pressurized Unsaturated Flow   |
| PW91     | Perdew-Wang 91 (functional)  |
| RN       | Radionuclide   |
| SNL      | Sandia National Laboratories   |
| SON68    | Nonradioactive glass developed by French Alternative Energies and Atomic Energy Commission |
| SPFT     | Single Pass Flow Through   |
| SPE      | Single-Point Energy  |
| TOF-SIMS | Time of Flight, Secondary Ion Mass Spectroscopy  |
| UFD      | Used Fuel Disposition  |
| UHF      | Unrestricted Hartree Fock  |
| UNLV     | University of Nevada Las Vegas   |
| VASP     | Vienna Ab-initio Simulation Package  |



# USED FUEL DISPOSITION CAMPAIGN/DISPOSAL RESEARCH ENGINEERED MATERIALS PERFORMANCE: WASTE FORM DEGRADATION MODEL INTEGRATION FOR ENGINEERED MATERIALS PERFORMANCE

## 1. INTRODUCTION

The Used Fuel Disposition Campaign has developed/implemented models for the degradation of spent (used) nuclear fuel (SNF) over the last few fiscal years, which are in the process of being implemented into Performance Assessment (PA) models to serve as a more process-based foundation of the fractional degradation rate of SNF currently sampled from distributions within the PA model (Sassani et al., 2013; Sassani et al., 2013). Similarly in this fiscal year (FY14), modeling activities focused on the degradation rates of the high-level waste glass waste form and of the metallic (Fe-Tc alloy) waste form were executed within the UFD Campaign as part of a larger effort across the Materials Recovery and Waste Forms (MRWF) Campaign (formerly the Separations and Waste Forms Campaign, in which these activities previously were executed). The management and integration of the glass and metallic waste form modeling activities within the UFD Campaign were performed within the Disposal Research Engineered Materials Performance (DREMP) technical work area (control account). This waste form degradation work was managed and directed within work package FT-14SN080405 and this report fulfills milestone M2FT-14SN0804051 and covers waste form degradation activities in this control account.

### 1.1 Waste Form Degradation Models

The work covered in this report represents a set of primarily modeling activities that feed into additional primarily experimental with model development activities within the Separations (Materials Recovery) and Waste Forms (SWF/MRWF) Campaign. The activities within the MRWF Campaign are those that will develop and provide models that are meant to interface with the Performance Assessment model for both glass and metallic waste form degradation rates. Figures 1.1-1 and 1.1-2 depict the activities described within this report (shapes with solid borders) and those within the MRWF Campaign (shapes with dotted boundaries), as well as the major connection pathways between them and into the PA Models. Achieving a high degree of integration both within the set of activities in the UFD Campaign, as well as across the UFD and MRWF Campaigns, for these technical topics was a larger challenge than solely within-campaign integration. However, the efforts by program management and all the investigators involved across these two campaigns have led to an increased awareness of technical interfaces and development across both these campaigns. This enhanced level of integration should facilitate incorporation of waste form degradation models for glass and metallic waste forms being developed in the MRWF Campaign for use in PA Models developed within the UFD Campaign.

#### 1.1.1 Glass Waste Form Degradation Activities

The activities for glass degradation modeling encompass scales from the molecular to the macroscale for evaluating the breakdown of the glass phase, the development of silica gel at the glass-water interface, and the formation of alteration phases at this interface. These activities are evaluating several different rate laws that have been proposed for these processes based on fitting experimental data and that are currently used to predict corrosion rates into the distant future in repository settings. In general, these rate laws base their limiting rates on either a transition state theory (TST) dissolution affinity rate law or on the rate of mass transport through the amorphous layers formed at the glass-water interface. The lack of a consensus on an integrated quantitative representation of the rate-limiting processes for nuclear waste

glass degradation initiated an effort to evaluate several processes of glass degradation in greater detail to enhance the technical bases for glass degradation rate models used in performance assessment of geologic disposal systems.

Molecular-scale first-principles modeling work on glass degradation mechanisms (Section 2.1) focuses on calculating the energies and barriers for bond-breaking reactions involving Si-O and B-O bonds at the glass surface. Figure 1.1-1 shows this work in the solid diamond titled “First Principles Models (ANL)”. This research effort is designed to develop a more complete constitutive expression for the TST affinity rates based on multicomponent glass surface structure. Reaction barriers and energies for dissolution reactions on protonated, neutral, and deprotonated sites on sodium borosilicate glass surfaces were calculated and reported. For these simple three component glasses ( $\text{Na}_2\text{O} - \text{B}_2\text{O}_3 - \text{SiO}_2$ ), there are only two framework metals (B and Si). However, there are numerous reactions occurring on the surface with different activation barriers and reaction energies depending on the bond saturation state of the B (or Si) atom being removed from the surface, the type and saturation state of the neighboring metal (B or Si) bonded to the same bridging oxygen atom, and the protonation state of the bridging oxygen. The tables in Section 2.1 report energies for 22 different surface reactions that play a role in  $\text{Na}_2\text{O}-\text{B}_2\text{O}_3-\text{SiO}_2$  glass dissolution.

Nano-continuum modeling (Section 2.2) focuses on reproducing the nanoscale concentration profiles at the glass-water interface observed for a 25-year degradation experiment for the French SON68 glass. Figure 1.1-1 shows this work in the solid ovoid titled “Reactive Transport Model (LBNL)”. A high resolution model of that glass-water interface is developed with a constant grid spacing of 1 nanometer and a continuum model assumption. Although using a continuum model at nanometer scale is an approximation, it is the only approach available that includes multicomponent chemistry with precipitation and dissolution at this scale. Using this model the compositional gradients reproduced are: (1) Li release from the glass; (2) hydrogen migration into the glass (glass hydration) from the solution and (3) boron release from the glass. The Li and H concentrations exhibit 15 nm wide gradients between the pristine glass and the hydrated glass layer that are anti-correlated (i.e., an interdiffusion layer). The B concentration defines a sharp profile (~3 nm width) located just outside (away from the pristine glass interface) of the Li/H interdiffusion layer. The  $K\mu\text{C}$  model incorporates the possible rate-controlling processes of (a) diffusion-limited glass corrosion, (b) affinity-controlled hydrolysis reactions based on TST rate laws, and (c) precipitation of secondary phases.

The Glass Corrosion Modeling Tool (GCMT; Section 2.3) has been developed for several purposes: (1) to examine efficiently the goodness of fit of a variety of glass corrosion models to specific experimental datasets, (2) to provide easy access and evaluation of an extensive database of glass alteration experimental results (consisting primarily of single pass flow through tests—i.e., ALTGLASS database being developed at Savannah River National Laboratory by Carol Jantzen), with the potential to use this database to derive new glass dissolution constitutive equations, and (3) to provide a platform for the newly developed Diffusive Chemical Reaction (DRCx) model. Figure 1.1-1 shows this work in the solid ovoid titled “Glass Degradation Modeling Tool (PNNL)”. The DRCx model, like the  $K\mu\text{C}$  model, is intended to be used to evaluate the detailed concentration profiles dataset from time-of-flight secondary ion mass spectrometry (TOF-SIMS) and atom probe tomography (APT) analyses of glass corrosion interfaces. Within the GCMT, the user can choose to implement various other models such as the Aagaard-Helgeson (AH) model with residual rate, the Grambow-Muller (GM) model and the Glass Reactivity with Allowance for the Alteration Layer (GRAAL) model. The ALTGLASS datasets could be used within the GCMT to develop new glass degradation constitutive equations. To facilitate this usage, a graphical user interface has been constructed in GCMT so that selection of datasets from the ALTGLASS database is a streamlined and transparent process.

### 1.1.2 Metallic Waste Form Degradation Activities

A multistep conceptual corrosion model for the release of Tc from any candidate alloy (e.g., Fe-Tc) waste form is described (Section 3.1). Figure 1.1-2 shows this work in the solid diamond titled “First Principles Models (LANL & PNNL)” as the first set of bullets. There are three viable rate-limiting mechanisms for Tc release: (1) cation vacancy annihilation at the metal/oxide interface, (2) transport of Tc through the oxide film, and (3) dissolution of Tc at the oxide/environment interface. Initial molecular-scale first-principles modeling has focused on applying DFT calculations to investigate the relative stability of different Fe-Tc oxides and the diffusion of Tc incorporated into vacancy defect sites in a range of Fe-oxide crystals. To validate the DFT approach used, the relative stabilities of Tc oxides were calculated and predicted properties were compared to measured values. To evaluate potential behavior of Tc in oxide films of a corroding alloy, models of Fe-oxide structures were designed with care to incorporate the magnetic ordering of the Fe atoms. Calculations of the energies for Tc incorporation into simple Fe vacancies in three Fe-oxide crystal structures were completed. This work evaluated energetics of Tc incorporation into three spinel phases (potential waste forms) of different crystal structures ( $\text{Fe}_3\text{O}_4$ ,  $\text{CaFe}_2\text{O}_4$ , and  $\text{YFe}_2\text{O}_4$ ).

Integrating modeling efforts focused on larger-scale simulations using kinetic Monte Carlo and force field methods. Finally, integrated with the modeling effort, electrochemical corrosion experimental studies have been performed on Tc metal in pH 3.2  $\text{H}_2\text{SO}_4$  solutions.

In related work (Section 3.2), additional molecular-scale first-principles modeling work is focused on investigating the incorporation of Tc into an iron oxyhydroxide (goethite,  $\alpha\text{-FeOOH}$ ) phase that could represent oxidized corrosion products of the metallic waste form or those of the waste package internal components. Figure 1.1-2 shows this work in the solid diamond titled “First Principles Models (LANL & PNNL)” as the second set of bullets. These calculations also constrain Tc affinity for bulk goethite versus goethite surface sites, and determining Tc stability on (in) goethite in the presence of adsorbates such as water, oxygen, hydrogen and hydrogen peroxide. All of these models provide quantitative constraints on the various mechanisms for metallic Tc waste for corrosion release of Tc and potential solid phases that may attenuate that release.

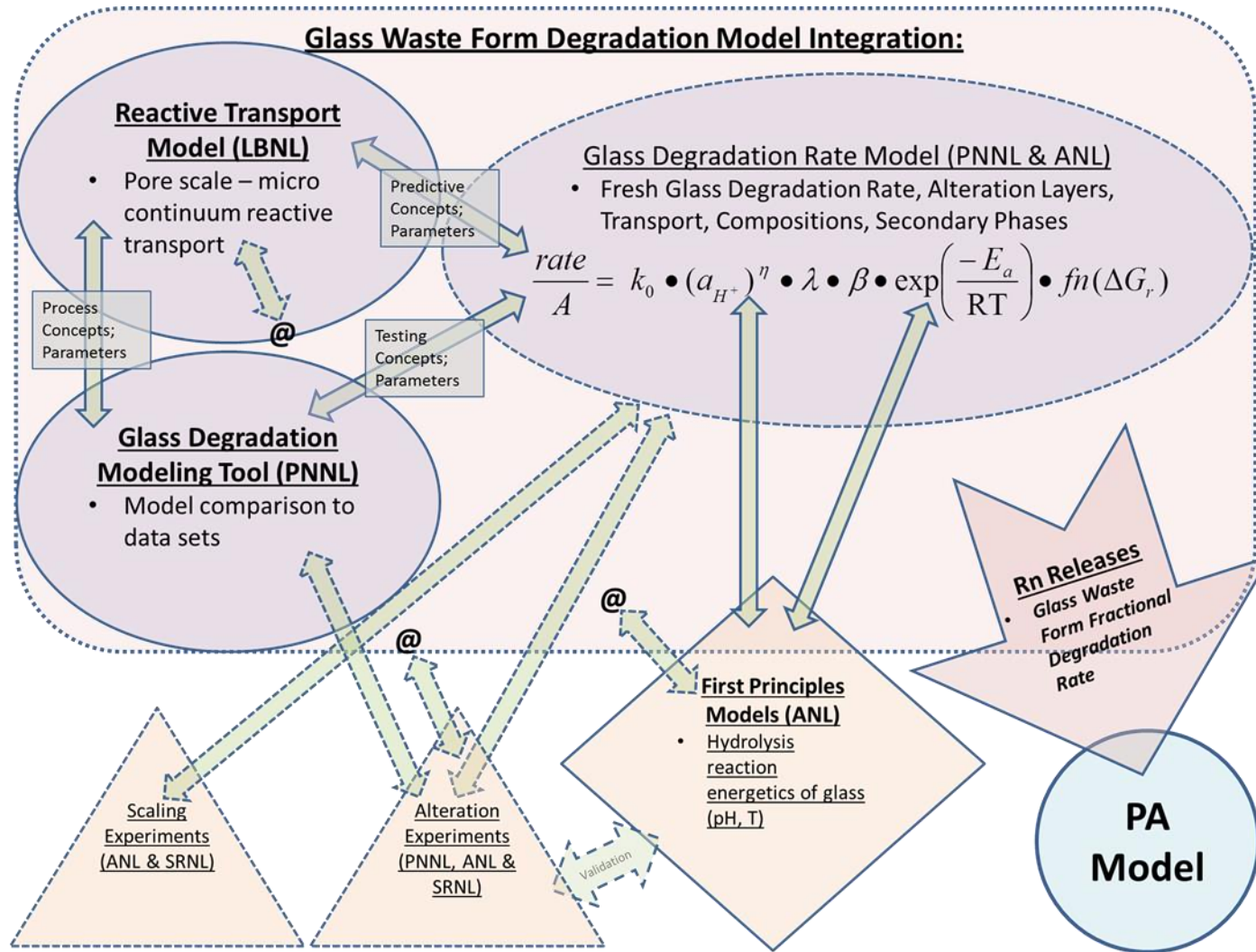


Figure 1.1-1. Schematic showing the three glass waste form degradation process modeling activities in the FY14 UFD Campaign (shapes with solid outlines): First Principles Models (ANL); Reactive Transport (micro-continuum) Model (LBNL); and Glass Degradation Modeling Tool (PNNL). Also shown are MRWF Campaign activities (modeling and experiments shown in shapes with dashed outlines) and the primary interfacing of those with the UFD glass waste form process modeling activities, and the major handoff into the UFD Campaign PA Model. Note that additional detailed activity connections within the MRWF Campaign activities are not shown here for simplicity.

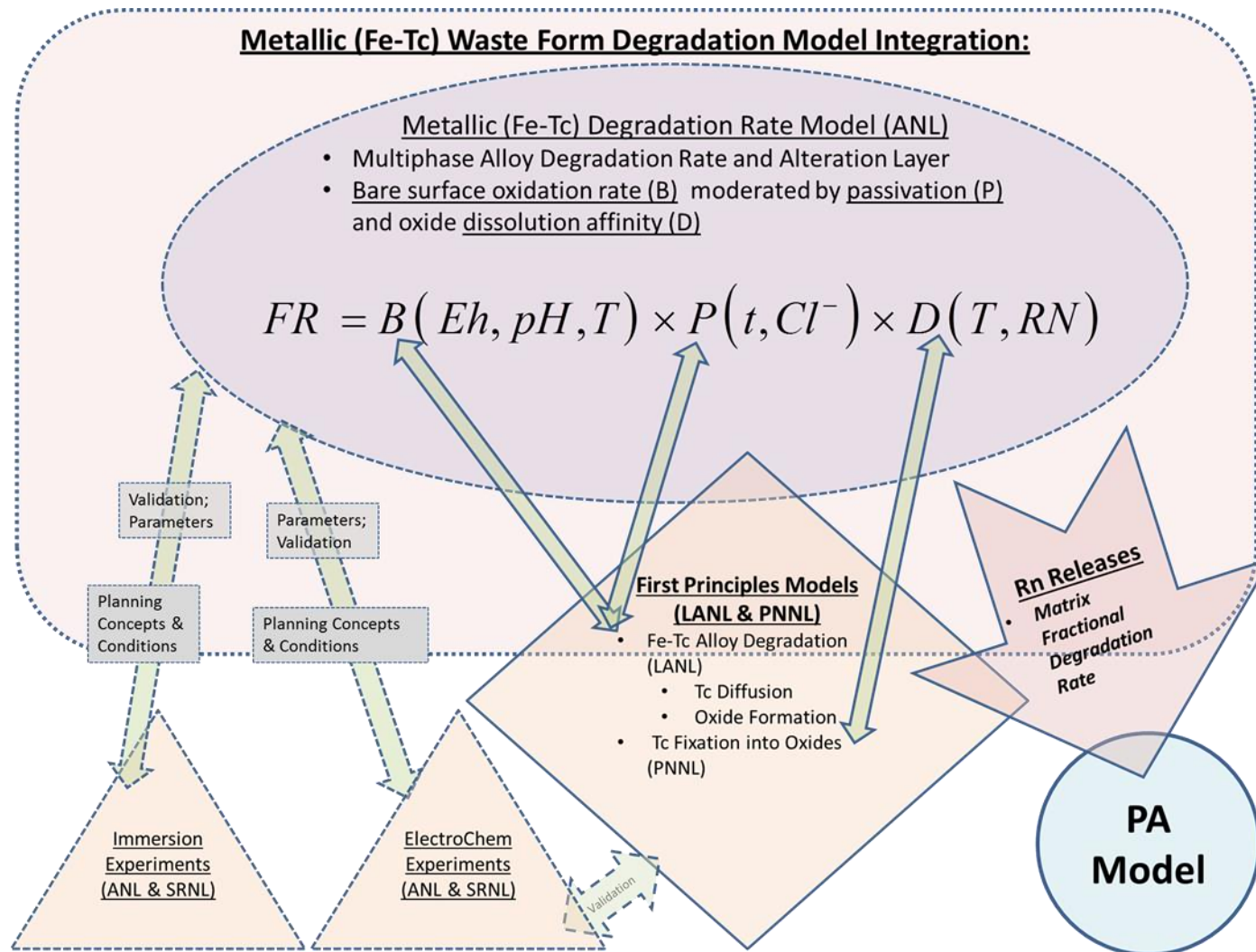


Figure 1.1-2. Schematic showing the metallic (Fe-Tc) waste form degradation First-Principles Models (LANLA & PNNL) modeling activities in the FY14 UFD Campaign (shape with solid outlines-note that there is an experimental component to the LANL activities). Also shown are MRWF Campaign activities (modeling and experiments shown in shapes with dashed outlines) and the primary interfacing of those with the UFD metallic waste form process modeling activities, and the major handoff into the UFD Campaign PA Model. Note that additional detailed activity connections within the MRWF Campaign activities are not shown here for simplicity.

## 1.2 Integration with Performance Assessment Models

The primary initial connection into the current performance assessment models for the glass and metallic waste form degradation models is the fractional degradation rate (FDR) parameter, which is currently sampled from a distribution (Section 4.1). This primary coupling allows for development of more process-based models that are able to supplant the FDR distribution by supplying that parameter directly as a result of the process model. This is the initial connection that is needed for implementation of the UF MPM described above. Additionally, if secondary phases are formed that will incorporate some fraction of the radionuclides being released from the glass or metal waste form, quantification of the amounts so sequestered and the rate of dissolution of the secondary phase would be another set of connections that could be defined.

For initial integration, the preferred approach is the direct incorporation of the coupled process model into the PA models (Section 4.2), as will be done with the spent fuel degradation model as the initial case. Such an approach can start simply (the PA model supplying basic physical parameters such as T) and progress to a more thorough coupling that would entail passing water compositional parameters (potentially from other internal chemistry models) as input to waste form degradation models, which would analyze the waste form degradation in that particular environment and provide the fractional degradation rate for those specific water compositions. This would be a bidirectional connection example (i.e., inputs and outputs both ways). Further coupling of the waste form degradation models into the PA model with a full suite of coupled thermo-hydro-chemical (THC) processes would allow a fully coupled feedback where, for example, in addition to the fractional degradation rate being provided to the performance assessment models, the change to water composition based on the glass waste form degradation could be supplied back to the PA model as well. The potential connections between the glass or metallic waste form degradation models and the other PA model subsystems are shown in Section 4.2. Such a staged developmental strategy facilitates incorporation of process-level detail as it is available and permits an evolving level of model complexity to be incorporated in a deliberate manner.

## 2. Glass Waste Form Degradation Modeling

The activities for glass degradation modeling encompass scales from the molecular-scale to the macro-scale for evaluating processes occurring within the glass structure, the breakdown of the glass phase, and the formation of alteration phases of the glass waste form. All of these processes result in the rate at which glass degradation releases radionuclides to the solution phase, in which radionuclide migration can then occur. The three model areas detailed below provide fundamental pieces of the foundation of process understanding to constrain those rates, and an integrated tool for analyzing experimental data to constrain the main processes occurring within the tests. Models constraining the degradation rate behavior of glass waste forms for use in performance assessment (PA) models are being developed within the Materials Recovery and Waste Forms (MRWF) Campaign. These activities provide process-level feeds into those additional activities in the MRWR Campaign.

### 2.1 Molecular-Scale First-Principles Modeling

The purpose of this Section is to provide results for using first-principles modeling of barriers and energies for elementary reactions to provide energetic parameters needed to model atomistic chemical processes and upscaling the results of those simulations (and their associated accuracies and uncertainties) into constitutive relations. The borosilicate glass structure used in these calculations contains Na, B and Si. The structure is derived from the molecular dynamics models. The particular emphasis is placed on calculations of reaction barriers for breaking Si-O bonds. The materials in this Section are from the Fuel Cycle Research and Development milestone M4FT-14AN0804013 in work package FT14AN080401.

Subcontinuum methods can play a major role in modeling glass dissolution processes where properly used and interfaced with continuum scale models by applying appropriate upscaling procedures. This report provides a set of energy barriers calculated from first principles for borosilicate glass that can be used for kinetic modeling, e.g. using Kinetic Monte Carlo (KMC), to provide a first-principles basis for investigations of the affinity term used in the reaction affinity dissolution model. First-principles methods have been applied to calculate the energies and barriers for bond-breaking surface reactions involving Si-O and B-O bonds. This section provides an overview of the problem.

Degradation model for borosilicate glass waste forms is needed to provide uncertainty quantification of the source term in geological disposal models. The dissolution of borosilicate glass nuclear waste forms has been studied extensively for more than thirty years, yet a full understanding of the processes that will govern long-term glass dissolution following geological disposal remains elusive (Van Iseghem et al., 2004). Some researchers believe that the long-term rate will be controlled by the residual dissolution affinity (i.e., free energy), while others believe that the long-term rate may be controlled by the mass transport rate through a thin protective restructured silicate layer that is formed on the surface of the corroding glass (Casey et al., 1993; Van Iseghem et al., 2004; Frugier et al., 2008). Incomplete understanding resulted in use of different rate laws to extrapolate the corrosion rate into the distant future (Van Iseghem et al., 2004). These rate laws are based either on a transition state theory chemical dissolution affinity rate law that was originally developed for silicate minerals (Aargaard and Helgeson, 1982) or on the rate of mass transport across the restructured silicate layer (referred to as the *Passivating Reactive Interface* layer) that is formed at the surface of the glass (Frugier et al., 2008). Another uncertainty is related to the role of secondary phase formation. Recent study suggests importance of inter-diffusion coupled with hydrolysis reactions of the silicate network in determining the long-term dissolution rate (Gin et al., 2013).

One fruitful path to achieving understanding of dissolution processes is likely to be through modeling and experiments designed to study the surface processes at the molecular level (Lasaga 1998). Examples of calculations of reaction barriers relevant to dissolution processes in minerals and glasses at the density functional theory (DFT) level of theory have been numerous and provided valuable information for development of reaction mechanisms (Gibbs, 1982; Gibbs et al., 1987; Lasaga and Gibbs, 1990; Xiao and

Lasaga, 1994; 1996; Strandh et al., 1997; Du et al., 2003; Ma et al., 2005). It is desirable to gain further insights by applying first-principles methods to realistic glass models. At the same time, it is recognized that investigation of surface processes involved in the dissolution rate of glass is particularly difficult because there is no ordered surface structure and because the surfaces may reorganize extensively as they interact with water during the dissolution process (Casey et al., 1993). Thus, only a few quantum chemical studies addressed hydrolysis in sodium borosilicate glasses. Monte Carlo simulations of glass dissolution (Cailleteau et al., 2008; Kerisit and Pierce, 2012) gained valuable insights on relationships between the composition and dissolution rates and mechanisms of nuclear waste glasses. Commonly, the rates for different reaction steps are postulated in these simulations, e.g. B release is assumed to be instantaneous once in contact with the bulk aqueous solution. First-principles calculations of hydrolysis reactions can determine energies and barriers for hydrolysis reactions on the surface to achieve understanding of rate-limiting steps and build better models for determining long-term dissolution rate.

Our previous work using first-principles methods has addressed some aspects of the dissolution model. Work on crystalline analogs has been performed to develop experimentally validated constitutive models for the forward dissolution rates. This work established sub-continuum models for the pH dependence of the dissolution rates and provided comparison to experimental data (Fenter et al., 2014). It was also demonstrated that, for acidic conditions, the pH-dependence of the glass dissolution rate is controlled primarily by the rate of protons arriving at the mineral surface. Previous work has addressed pH dependence of B-O bond dissociation and explained changes in glass dissolution mechanism with pH (Zapol et al., 2013).

Here we report calculated reaction barriers and reaction energies for dissolution reactions on protonated, neutral and deprotonated sites on sodium borosilicate glass surfaces for different configurations involving Si-O and B-O bonds. The results can provide useful insights in understanding surface reactions and forward rates in the more complex waste glass systems.

### 2.1.1 MODELING APPROACHES

This section provides description of computational methods used to obtain reaction barriers on glass surfaces provided in the subsequent sections. Primarily, first-principles computational methods used are based on DFT. One of the main advantages of first-principles compared to empirical based modeling is the capability to rigorously take into account events beyond the limits of experimental measurements, such as contributions of slow reaction pathways that could dominate the effective rates at long time scales. Direct atomistic modeling of a glass surface in contact with solution at a given pH and temperature is not always feasible. Therefore, the use of first-principles methods requires judicious choice of approximations that are suitable for specific applications.

All the calculations were done within the framework of the density functional theory (DFT) as implemented in the VASP program (Kresse and Furthmuller, 1996). Periodic boundary conditions are applied, which makes it possible to take into account geometry constraints during reactions. In a periodic model, the boundary conditions are satisfied for bulk crystals by virtue of Bloch theorem. Application of periodic boundary conditions to surfaces requires an additional approximation, a slab model. The PBE exchange-correlation functional form was used. The plane-wave basis set and the PAW potentials were used. The energy cutoff for plane waves was 400 eV. Transition states along the reaction pathways were located using the Climbing Image Nudged Elastic Band algorithm (Henkelman, and Jonsson, 2000).

The description of the procedure to obtain models of the glass structure is provided in Zapol et al. (2013). For borosilicate glass calculations, the surface  $\text{Na}^+$  ions were substituted with protons in considering the fast ion-exchange effect near surface in contact of water. These surfaces are then used to explore reaction pathways for water reactions with neutral, protonated and deprotonated sites of constituting network formers Si and B. A typical supercell has about ~120 atoms and a vacuum of 15 Å in the z direction of the supercell. All the barrier calculations are done for charge-neutral systems. In case of protonation, either a charge-compensating H (overall charge balanced) or an extra H is introduced. In case of deprotonation, an

extra OH is introduced. Effectively, after reaching the self-consistency of electron distribution, H and OH species become  $H^+$  and  $OH^-$ , respectively. The charges of  $H^+$  and  $OH^-$  are compensated by the complementary  $OH^-$  and  $H^+$ , respectively, on the other side of the slab.

## 2.1.2 REACTION ENERGIES AND BARRIERS IN BOROSILICATE GLASS

This subsection describes calculated reaction barriers and reaction energies for dissolution reactions on protonated, neutral and deprotonated sites on sodium borosilicate glass for different configurations involving B-O bonds. While the results are summarized for a simple sodium borosilicate glass, it can be generalized for the more complex waste glass systems.

### 2.1.2.1 Reaction Barriers for Hydrolysis of B-O Bonds on Glass Surface

Reaction energies and barriers for hydrolysis reactions in sodium borosilicate glass were calculated for deprotonated, neutral and protonated sites for various Q configurations of B and Si atoms. The results for reaction energies/barriers are summarized in Table VI. Schematic of hydrolysis reactions is given in Figure 2.1-1 (B-O-Si) and Figure 2.1-2 (B-O-B). In cases when multiple pathways were investigated, only the pathway with the lowest barrier is given in Table 2.1-1.

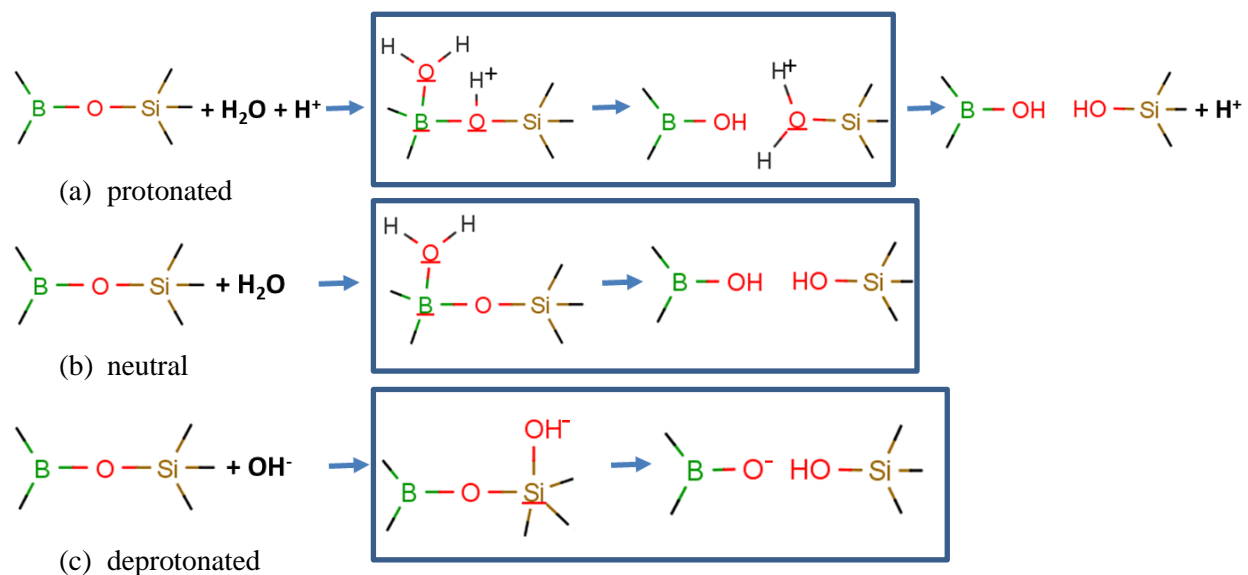


Figure 2.1-1. Schematic illustration of the hydrolysis reactions at the  $^3B-O-Si$  bridge under (a) acidic (protonated), (b) neutral, and (c) basic (deprotonated) conditions. Boxes illustrate reaction steps calculated using DFT.

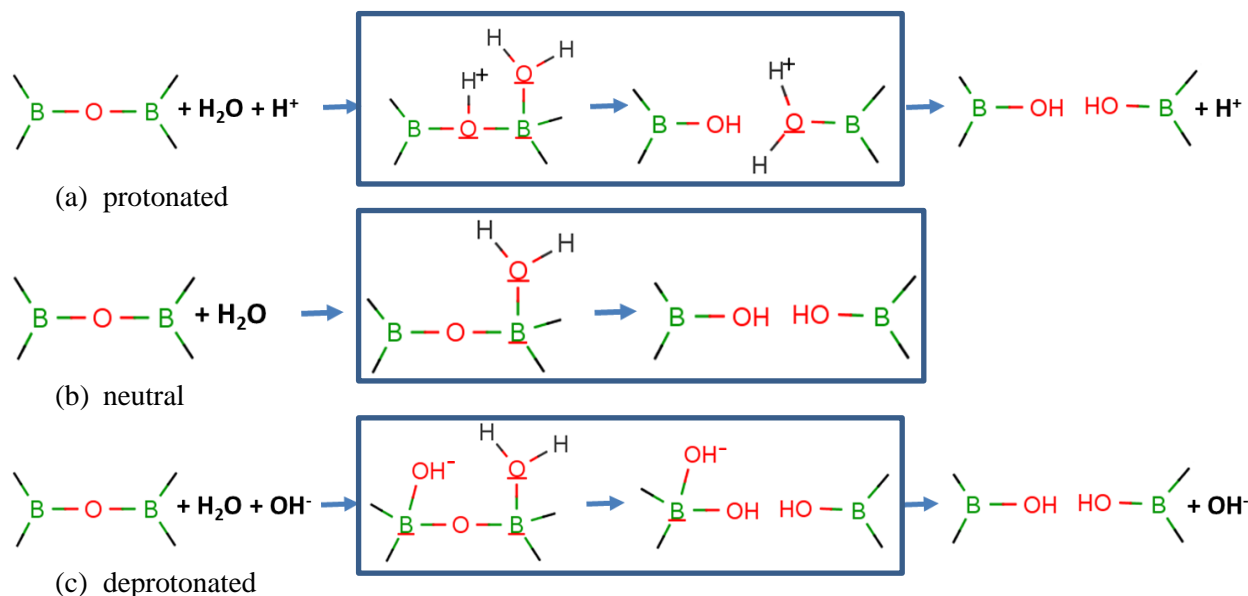


Figure 2.1-2. Schematic illustration of the hydrolysis reactions at the 3B-O-3B bridges under (a) acidic (protonated), (b) neutral, and (c) basic (deprotonated) conditions. Boxes illustrate reaction steps calculated using DFT.

Table 2.1-1. Calculated activation barriers  $E_a$  and reaction energies  $E_{rxn}$  (in kJ/mol) for dissolution reactions at borosilicate glass surface.

|  | $E_a$ (kJ/mol) |         |              | $E_{rxn}$ (kJ/mol) |         |              |
|--|----------------|---------|--------------|--------------------|---------|--------------|
|  | Protonated     | Neutral | Deprotonated | Protonated         | Neutral | Deprotonated |
| ${}^3\text{B}(\text{Q}^1)\text{-O-}{}^3\text{B}(\text{Q}^3)$ | 23             | 102     | 39           | -228               | -67     | -168         |
| ${}^3\text{B}(\text{Q}^2)\text{-O-}{}^3\text{B}(\text{Q}^2)$ | 18             | 129     | 145          | -53                | -3      | 42           |
| ${}^3\text{B}(\text{Q}^2)\text{-O-}{}^3\text{B}(\text{Q}^3)$ | 53             | 98      | 115          | -5                 | 47      | 73           |
| ${}^3\text{B}(\text{Q}^3)\text{-O-}{}^4\text{B}(\text{Q}^4)$ | 60             | 113     | -            | 48                 | -21     | -            |
| ${}^3\text{B}(\text{Q}^2)\text{-O-Si}(\text{Q}^3)$           | 60             | 106     | 108          | -1                 | 48      | 45           |
| ${}^3\text{B}(\text{Q}^2)\text{-O-Si}(\text{Q}^4)$           | 80             | 102     | 120          | -70                | 1       | 64           |
| ${}^4\text{B}(\text{Q}^4)\text{-O-Si}(\text{Q}^2)$           | 72             | 151     | -            | 17                 | 20      | -            |

It was found that  ${}^4\text{B}$  is easily converted into  ${}^3\text{B}$  in the presence of proton near the B-O bond. For  ${}^3\text{B}$  reactions, reaction barriers are low ( $\leq \sim 50$  kJ/mol) under acidic conditions.

Under neutral conditions, reaction barriers are around 100-110 kJ/mol and not sensitive to the Q value. These values are lower than comparable values for Si-O bonds, suggesting that B dissolution is faster than Si, in general agreement with experimental observations. In contrast to results for Si-O bonds, deprotonation under basic conditions does not help to reduce the reaction barriers for B-O bonds.

### 2.1.2.2 Reaction Barriers for Hydrolysis of Si-O Bonds on Glass Surface

Reaction energies and barriers for hydrolysis reactions of Si-O-Si bridges in sodium borosilicate glass were calculated for deprotonated, neutral and protonated sites for various Q configurations Si atoms. The results for reaction energies/barriers are summarized in Tables 2.1-2 through 2.1-4. The geometries are given in Figures 2.1-3 through 2.1-5.

Table 2.1-2. Reaction barriers and energies for bond breaking at protonated Si(Q<sub>n</sub>)-O-Si(Q<sub>m</sub>) bridge (kJ/mol).

|   | E <sub>a</sub> (kJ/mol) | Er <sub>xn</sub> (kJ/mol) |
|---|-------------------------|---------------------------|
| Si(Q <sup>1</sup> )-O-Si(Q <sup>3</sup> ) | 85.9                    | -36.7                     |
| Si(Q <sup>2</sup> )-O-Si(Q <sup>3</sup> ) | 68.5                    | -56.9                     |
| Si(Q <sup>2</sup> )-O-Si(Q <sup>4</sup> ) | 135.1                   | -50.2                     |
| Si(Q <sup>3</sup> )-O-Si(Q <sup>2</sup> ) | 99.4                    | -1.0                      |
| Si(Q <sup>3</sup> )-O-Si(Q <sup>3</sup> ) | 127.4                   | 98.4                      |
| Si(Q <sup>4</sup> )-O-Si(Q <sup>3</sup> ) | 129.3                   | 97.4                      |

In this case, we calculate reaction barriers to be lower for lower Q values, consistently with the general trends in previous studies. Reaction energies are negative for low Q values and positive for high Q values, which was also the case in orthoclase simulations. In general, we do not observe much lower reaction barriers for Si-O bond dissociation in glass than in orthoclase.

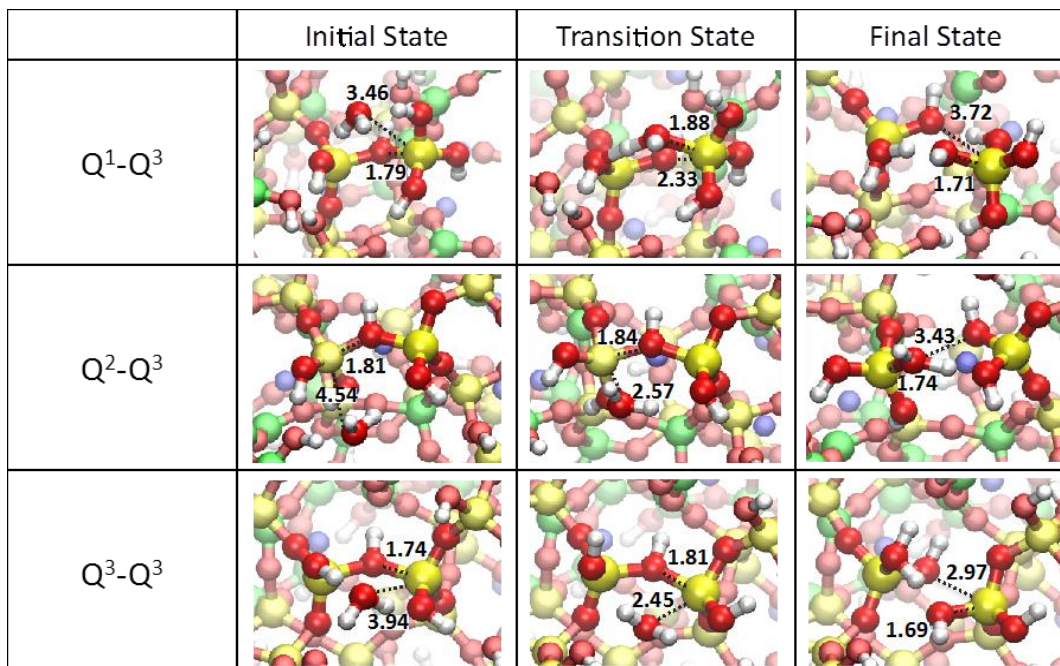


Figure 2.1-3. Optimized initial, transition and final state geometries along the hydrolysis reaction pathway at the Si-O-Si bridges under acidic (protonated) conditions.

Table 2.1-3. Reaction barriers and energies for Si-O-Si bond breaking (kJ/mol) in neutral case

| Reaction Barriers (kJ/mol) | Q <sup>1</sup> | Q <sup>2</sup> | Q <sup>3</sup> | Q <sup>4</sup> |
|----------------------------|----------------|----------------|----------------|----------------|
| Q <sup>1</sup>             |                | 170.8          | 158.2          | 243.1          |
| Q <sup>2</sup>             |                | 151.5          | 166.9          | 205.5          |
| Q <sup>3</sup>             | 214.2          | 190.1          | 214.2          | 250.8          |
| Q <sup>4</sup>             |                | 248.0          | 272.1          |                |
| Reaction Energies (kJ/mol) | Q <sup>1</sup> | Q <sup>2</sup> | Q <sup>3</sup> | Q <sup>4</sup> |
| Q <sup>1</sup>             |                | 81.0           | 94.6           | -1.9           |
| Q <sup>2</sup>             | 32.8           | 63.7           | 178.5          | 74.3           |
| Q <sup>3</sup>             |                | 70.4           | 92.6           | 0.0            |
| Q <sup>4</sup>             |                | 81.0           | 94.6           | -1.9           |

As in the other studies by us and others, the barriers are much higher compared with either protonated or deprotonated case.

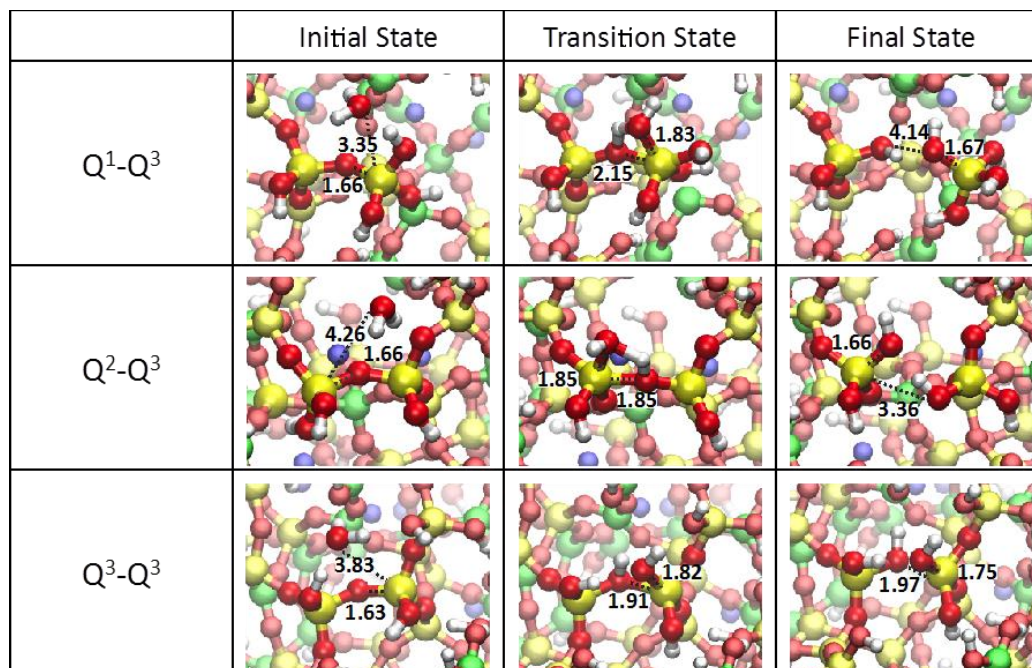


Figure 2.1-4. Optimized initial, transition and final state geometries along the hydrolysis reaction pathway at the Si-O-Si bridges under neutral conditions.

Table 2.1-4. Reaction barriers and energies for Si-O-Si bond breaking (kJ/mol) in basic (deprotonated) case.

|   | $E_a$ (kJ/mol) | $E_{rxn}$ (kJ/mol) |
|---|----------------|--------------------|
| Si(Q <sup>1</sup> )-O-Si(Q <sup>3</sup> ) | 28.0           | -63.7              |
| Si(Q <sup>2</sup> )-O-Si(Q <sup>3</sup> ) | 55.0           | 14.5               |
| Si(Q <sup>2</sup> )-O-Si(Q <sup>4</sup> ) | 29.9           | -83.9              |
| Si(Q <sup>3</sup> )-O-Si(Q <sup>2</sup> ) | 53.1           | 29.9               |
| Si(Q <sup>3</sup> )-O-Si(Q <sup>3</sup> ) | 59.8           | 33.8               |

The barriers are calculated for the Si-O bond dissociation starting with five-coordinated intermediate. The barriers in deprotonated case are lower than in the neutral case.

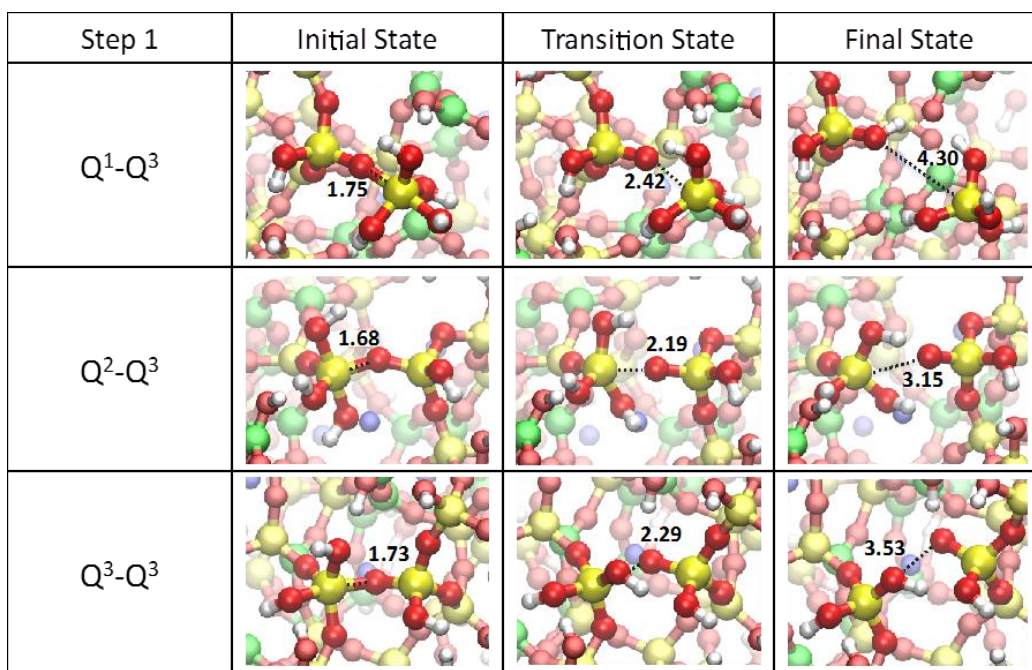


Figure 2.1-5. Optimized initial, transition and final state geometries along the hydrolysis reaction pathway at the Si-O-Si bridges under acidic (protonated) conditions.

### 2.1.3 CONCLUSIONS AND RECOMMENDATIONS

The molecular-scale models above provide a set of energy barriers for silica hydrolysis reactions developed from the first principles calculations that can be used for modeling borosilicate glass dissolution. Calculations of elementary reactions steps should be followed by Kinetic Monte Carlo for purposes of upscaling simulations of glass dissolution. Subsequent sensitivity analysis should be used to determine rate-limiting steps. These simulations provide a connection between glass structure/composition and the dissolution rate in order to form a basis for investigations of the affinity term used in the reaction affinity model.

## 2.1.4 References

- Aagaard, P., and H.C. Helgeson, 1982, Thermodynamic and kinetic constraints on reaction rates among minerals and aqueous solutions: I. Theoretical considerations, *American Journal of Science* 282 (1982), pp. 237–285
- Cailleteau, C., F. Angeli, F. Devreux, S. Gin, J. Jestin, P. Jollivet, O. Spalla, 2008, Insight Into Silicate-Glass Corrosion Mechanisms, *Nat. Mater.* 7 (2008) 978–983.
- Casey, W. H., H. R. Westrich, J. F. Banfield, G. Ferruzzi, and G. W. Arnold, 1993 Leaching and Reconstructing at the Surface of Dissolving Chain-Silicate Minerals, *Nature*, 366, 1993.
- Du, M. H., A. Kolchin and H. P. Cheng, 2003, Water-silica surface interactions: A combined quantum-classical molecular dynamic study of energetics and reaction pathways, *J. Chem. Phys.* 119 6418, 2003.
- Fenter, P., P. Zapol, H. He, N. Sturchio, 2014, On the Variation of Dissolution Rates at the Orthoclase (001) Surface with pH and Temperature, *Geochim. Cosmochim. Acta*, 2014, DOI: 10.1016/j.gca.2014.06.019
- Frugier, P., S. Gin, Y. Minet, T. Chave, B. Bonin, N. Godon, E. E. Lartigue, P. Jollivet, A. Ayrat, S. De Windt, and G. Santarini, 2008, SON68 Nuclear Glass Dissolution Kinetics: Current State of Knowledge and Basis of the New GRAAL Model, *Journal of Nuclear Materials*, 380, pp 8-21, 2008.
- Gibbs, G. V., 1982, Molecules as Models for Bonding in Silicates, *Am. Mineral.* 1982, 67, 421.
- Gibbs, G. V., D'Arco, P.; Boisen, M. B., Jr., 1987, Molecular Mimicry of Bond Length and Angle Variations in Germanate and Thiogermanate Crystals: A Comparison with Variations Calculated for C-, Si-, and Sn-Containing Oxide and Sulfide Molecules, *J. Phys. Chem.* 1987, 91, 5347.
- Gin et al., 2013. S. Gin, J.V. Ryan, D.K. Schreiber, J. Neeway, M. Cabié, Contribution of atom-probe tomography to a better understanding of glass alteration mechanisms: Application to a nuclear glass specimen altered 25 years in a granitic environment, *Chemical Geology*, 349–350, (2013), 99-109.
- Henkelman, and Jonsson, 2000. Henkelman, G. and H. Jonsson, Improved tangent estimate in the nudged elastic band method for finding minimum energy paths and saddle points. *J. Chem. Phys.*, 2000, 113(22): 9978-9985.
- Kerisit, S., and E.M. Pierce, 2012, Monte Carlo Simulations of the Dissolution of Borosilicate Glasses in Near-Equilibrium Conditions, *Journal of Non-Crystalline Solids* 358 (2012) 1324–1332.
- Kresse, G. and J. Furthmuller, 1996, Efficient iterative schemes for ab initio total-energy calculations using a plane-wave basis set, *Physical Review B* 1996, 54(16): 11169-11186.
- Lasaga, A.; Gibbs, G. V. 1990, *Ab-Initio* Quantum Mechanical Calculations Of Water-Rock Interactions; Adsorption And Hydrolysis Reactions, *Am. J. Sci.* 1990, 290, 263.
- Lasaga, A. C., 1998, *Kinetic Theory in the Earth Sciences*, 728 (Princeton Univ.Press, 1998).
- Ma, Y., A. S. Foster, and R. M. Nieminen, 2005, Reactions and clustering of water with silica surface, *J. Chem. Phys.* 122144709, 2005.
- Strandh, H., Pettersson, L. G. M., Sjöberg, L., Wahlgren, U., 1997, Quantum Chemical Studies of the Effect on Silicate Mineral Dissolution Rates by Adsorption of Alkali Metals, *Geochim. Cosmochim. Acta* 1997, 61, 2577.
- Van Iseghem, P., M. Aertsens, S. Gin, D. Deneele, B. Grambow, P. McGrail, D. Strachan, and G. Wicks, 2004, A Critical Evaluation of the Dissolution Mechanisms of High Level Waste Glasses in

Conditions of Relevance for Geological Disposal, European Commission, 5th Euratom Framework Programme 1998-2002, Contract NO. FIKW-CT-2001-20140, Final Report 2001-11-01 to 2004-10-31.

Xiao, Y., and Lasaga, A., 1994, *Ab Initio* Quantum Mechanical Studies Of The Kinetics And Mechanisms Of Silicate Dissolution:  $H^+(H_3O^+)$  Catalysis, *Geochim. Cosmochim. Acta* 1994, 58, 5379;

Xiao, Y., and Lasaga, A., 1996, *Ab initio* quantum mechanical studies of the kinetics and mechanisms of quartz dissolution:  $OH^-$  catalysis, *Geochim. Cosmochim. Acta* 1996, 60, 2283.

Zapol, P., H. He, K. D. Kwon and L. J. Criscenti, 2013, First-Principles Study of Hydrolysis Reaction Barriers in a Sodium Borosilicate Glass, *International Journal of Applied Glass Science*, 4, 395–407 (2013)

## 2.2 Pore-(Nano-)Scale Continuum Modeling

The purpose of this Section is to report on preliminary nano-continuum scale modeling of nuclear waste glass corrosion. The focus of the modeling is an experiment involving a French glass SON68 specimen leached for 25 years in a granitic environment (Guittonneau et al., 2011; Gin et al., 2011; Gin et al., 2013). The 25-year experiment carried out by French scientists offers a unique opportunity to examine the controls on the rate of nuclear glass corrosion under controlled experimental conditions using a borosilicate glass of the kind widely considered for nuclear waste storage. The information in this Section comes from milestone: M4FT-14LB0804031 generated in work package FT-14LB080403.

This long term experiment makes it possible to move beyond the initial rate stage, with direct measurements of the longer term, residual rates of corrosion. Important in this regard is whether the rate of corrosion shows a parabolic dependence on time, as would be expected from a conventional diffusion model in which the reaction products (amorphous silica-rich gel) create a diffusion barrier that grows in width over time, or whether the time dependence is linear (Guittonneau et al., 2011). A linear dependence on time would call into question the model of a Passive Reactive Interface (PRI) presented by Cailleteau et al. (2008), although it does not entirely preclude such a model if the interface maintains a constant width over time (forming at the leading edge next to the pristine glass and dissolving at the trailing edge). The leachate concentration measurements collected every 56 days over 25 years by Guittonneau et al. (2011) provide data to constrain the long term corrosion rate and its time dependence.

Equally important for understanding the actual mechanisms involved was the use of high spatial resolution chemical profiling of the nuclear glass leach layer. In this regard, the width of the reaction zone constrains to some extent the mechanisms involved, since a sharp boundary is not compatible with models presented earlier in which leaching occurs by inter-diffusion over a significant width of the gel corrosion layer. In addition, the spatial ordering of concentration profiles (coincident or non-coincident) may offer constraint on the mechanisms involved (Gin et al., 2013).

In this report, we focus on evaluating the nano-scale concentration profiles reported in Gin et al. (2013). Carrying out the numerical analysis all the way to 25 years would require a larger grid, albeit in one dimension, so this will be reported on in subsequent reports. We use a high resolution continuum model with a constant grid spacing of 1 nanometer to investigate the glass corrosion mechanisms. While the continuum assumption is a severe approximation given the fact that the pores themselves are close to this size, this is currently the only way we have to consider the longer spatial and time scales for this problem. In addition, it allows us to include full multicomponent chemistry (including precipitation and dissolution), something which is not possible with molecular modeling approaches (Bourg and Steefel, 2012).

### 2.2.1 SUMMARY OF 25 YEAR FRENCH GLASS SON68 LEACHING EXPERIMENT

Guittonneau et al. (2011) report on a 25.75-year leaching experiment (Figure 2.2-1) designed to improve our understanding of the mechanisms controlling glass dissolution in geological disposal conditions. A SON68 glass block was leached in slowly renewed synthetic groundwater (at 90°C, 100 bars) in contact with sand, granite and Ni–Cr–Mo alloy specimens. One hundred and sixty-three samples were collected over the entire duration of the experiment and were used to calculate the mean thickness of the altered glass ( $28 \pm 9 \mu\text{m}$ ) and the glass dissolution rate. After several months, the corrosion rate remained very constant at  $6 \times 10^{-3} \text{ g m}^{-2} \text{ d}^{-1}$  over the 25 years of the experiment, which is about 20 times higher than the residual rate measured in a batch reactor at the same temperature. The glass alteration layers investigated by Scanning Electron Microscopy (SEM) at the end of the experiment, however, showed neither a homogeneous thickness nor a homogeneous morphology.

The location of the sampling valve (at half the height of the glass block) seems to divide the glass block into two parts. In the upper half (above the sampling valve), the general morphology of the alteration

layer consists of a relatively simple and uniform gel with some secondary phases that include rare earth phosphates. The mean measured thickness of this alteration layer is  $6.7 \pm 0.3 \mu\text{m}$ . However, in the lower half of the glass block, the gel layer is thicker, with a mean measured thickness of  $81.3 \pm 1.1 \mu\text{m}$ . These results indicate that the chemistry of the leachate solution was not homogeneous, presumably due to the effects of local transport within the experimental reactor. This led the authors to conclude that rate of glass corrosion is very sensitive to the composition of the leachate solution close to the glass surface, and thus to the rate of water renewal (flow). The study clearly shows that the overall rate of corrosion (aside from the variations in corrosion rate presumably due to local transport effects) was constant (linear) over nearly 25 years.

While the Guittonneau et al. (2011) study presented important information on the bulk leaching rate of the nuclear glass specimen over 25 years, the ground-breaking study by Gin et al. (2013) on the SON68 glass specimen presented extremely high spatial resolution post-mortem chemical profiles using atom probe tomography (APT) and Energy-Filtered Transmission Electron Microscopy (EFTEM). The APT technique allows the 3D reconstruction of the elemental distribution at the reactive interphase with sub-nanometer precision. The results show that (1) Li from the glass and hydrogen from the solution exhibit anti-correlated 15 nm wide gradients located between the pristine glass and the hydrated glass layer, and (2) boron exhibits an unexpectedly sharp profile ( $\sim 3 \text{ nm}$  width) located just outside (away from the pristine glass interface) of the Li/H interdiffusion layer. The authors interpreted the sharp profile as being consistent with a dissolution front rather than a diffusion-controlled release of boron. As a result, the accessibility of water to the pristine glass could be the rate-limiting step under these conditions. More generally, these findings strongly support the importance of inter-diffusion coupled with hydrolysis of the pristine glass silicate network as the primary controls on the long-term dissolution rate. The primary objective of the nano-continuum approach presented here is to determine whether this conceptual model proposed by Gin et al. (2013) is supported by quantitative numerical modeling.

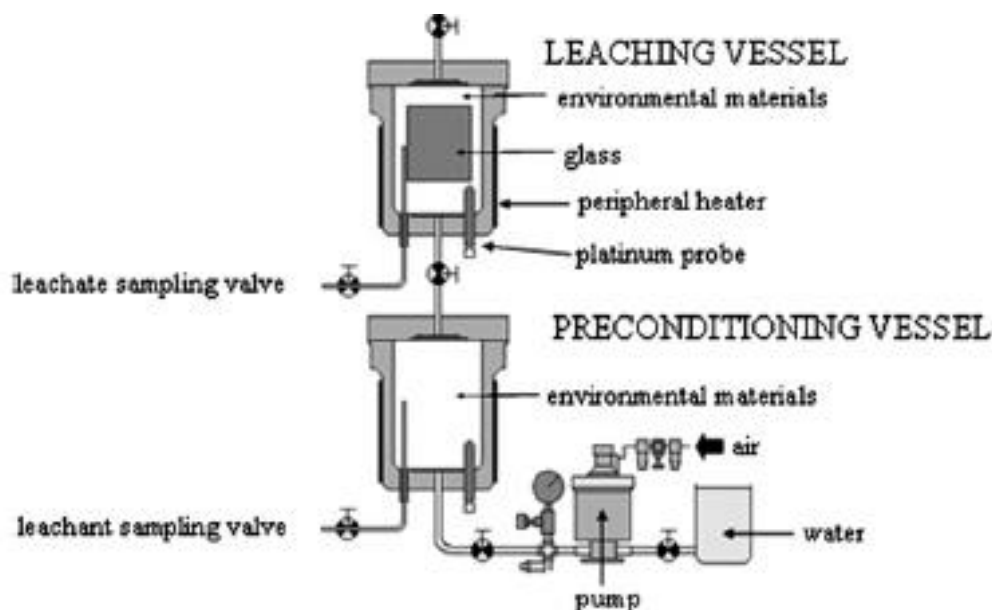


Figure 2.2-1. Experimental setup for the 25 year SON68 glass leaching experiment (Guittonneau et al., 2011)

## 2.2.2 KINETIC-MICROSCOPIC-CONTINUUM MODEL ( $K\mu C$ )

A new Kinetic Micro-Continuum ( $K\mu C$ ) model for glass corrosion has been developed that avoids *a priori* assumptions about rate-limiting steps in the overall corrosion process. The  $K\mu C$  model provides a flexible approach in which individual parameters and processes are tunable, but in every case coupled within an overall dynamic framework. The  $K\mu C$  model may currently be run with either a single glass

composition, which requires initially congruent dissolution, or it may be run with one or more glass end-member compositions that show differing thermodynamic and kinetic behavior. Since the single glass composition can be used to model overall incongruent reaction by incorporating rapid re-precipitation and/or ripening reactions, it is the preferred approach. The model currently includes the following processes

- Diffusion of water through the pristine glass and its alteration products;
- Ion exchange between water and the cations in the glass;
- Kinetically controlled hydrolysis reactions resulting in breaking of glass network bonds (Si, B, Al, etc.). The rate may be described by either a linear or a nonlinear TST law with an affinity control supplied by a specific phase (e.g., amorphous silica), or with an irreversible rate law with no affinity control. In either case, far from equilibrium dependencies of the rate on other dissolved (e.g., pH, Al, silica) or sorbed species can be included;
- Multicomponent diffusion of ions through the glass corrosion products;
- Precipitation reactions for amorphous and/or crystalline phases of variable composition that are kinetically and thermodynamically controlled;
- Kinetically controlled ripening and/or densification reactions that can reduce the porosity and/or pore connectivity (and thus the diffusivity) of the corrosion products;
- Kinetically and thermodynamically controlled formation of new crystalline phases (e.g., smectite, zeolite), with possible consequences for the transport properties of the corrosion layer;
- Flow and diffusion in the aqueous phase adjacent to the glass surface.

The K $\mu$ C model incorporates the possibility of diffusion-limited glass corrosion by considering explicitly the kinetically-controlled densification of either (1) a residual silica-rich glass network in which other important components (e.g., the cations and network former boron) have been leached, or (2) of a newly precipitated silica-rich gel layer. However, in contrast to the GRAAL model (Frugier et al., 2008; Cailleteau et al., 2008), a diffusion-limited corrosion rate is not assumed *a priori* in the K $\mu$ C model. Whether a passivating layer (i.e., defined as the *Passivating Reactive Interface* (PRI) by Frugier et al., 2008) forms in the K $\mu$ C model depends on the relative rates of (1) silica recrystallization and densification, (2) leaching of the glass constituents, and (3) dissolution and/or recrystallization of the corrosion products.

The dissolution rate of the glass in the K $\mu$ C model is not artificially limited by the approach to amorphous silica saturation (e.g., Grambow, 2006), although this formulation can be used if required. Thus, non-zero corrosion rates are allowed under conditions of silica saturation. Since the K $\mu$ C model is formulated with an explicit treatment of multicomponent diffusion, kinetically-controlled mineral dissolution and precipitation, and glass corrosion, it can take into account the possibility that local chemical conditions within the nano- and micropores in the reaction products (i.e., the silica gel layer) may differ from conditions in the bulk solution adjacent to the corroding glass. In the absence of a reaction layer that limits diffusive transport to the pristine glass surface, silica saturation may not occur and the long-term rate of glass corrosion may remain high. In this case, the reduction in rate due to silica will be largely due to the ambient silica concentrations in the groundwater.

### 2.2.3 MODEL SETUP FOR 25 YEAR FRENCH GLASS EXPERIMENT

Ideally, the treatment of the corrosion of the SON68 glass over 25.75 years would involve a 3D analysis so as to capture the strong variations in the width of the corrosion zone on the glass surface within the experimental reactor. Clearly, there is some form of combined transport control at work here, potentially reflecting the role of both flow (the solution is renewed completely about once every five years, i.e., at a

rate of 22% of the total reactor porosity per year) and molecular diffusion. In addition to the 3D geometry, however, there is also the challenge of representing adequately the multiple scales involved here, with the experimental reactor involving scales of 10s of centimeters, while the corrosion layers on the glass require discretization on the order of nanometers.

Because our preliminary focus is on representing the width of the various reaction zones close to the pristine glass surface and their relative positions, we assume a pure diffusion-controlled regime in an idealized 1-dimensional geometry, and a constant grid spacing of 1 nanometer (Figure 2.2-2). The first 25 nanometers correspond to the granite and sand-filled zone upon which the SON68 rests. The assumption that a continuum model applies at this spatial scale is a severe approximation, given that pore sizes are close to this value, but the approach allows us to compare results with elemental profiles and avoids the additional constraints of a computationally expensive and chemically simplified atomistic treatment.

As a boundary condition at one end of the reactor-glass specimen system, we consider a Dirichlet condition corresponding to the water used to replenish periodically the experimental reactor (Guittonneau et al., 2011). The fixed concentration (Dirichlet) boundary condition is probably the best approximation to a flow-through system. At the other end of the 1D system, we assume a no-flux condition, which is reasonable as long as the corrosion front does not fully penetrate the glass specimen.

Within the first 25 nanometers of the reaction model, the system is characterized by a porosity of 0.41 (as in the experimental system reported by Guittonneau et al., 2011) and a mixture of quartz sand and granite. A diffusivity of  $10^{-11}$  m<sup>2</sup>/s for all ions was assumed for the sand-granite mixture. The alloy specimens included in the experiments were not considered in the modeling. From 25 nanometers out to 225 nanometers, the system was assumed to consist of a SON68 borosilicate glass with a porosity of 1%.

The diffusivity of the borosilicate glass was assumed to follow a threshold type of model (Navarre-Sitchler et al., 2009), with a value of  $10^{-23}$  m<sup>2</sup>/s (in approximate agreement with the value proposed by Gin et al., 2013) for values of the porosity below 30% and a value of  $10^{-11}$  m<sup>2</sup>/s for porosity values above 30%. Previous model results (Navarre-Sitchler et al., 2011) indicate that a simple porosity dependence using an unmodified Archie's Law formulation cannot replicate the observed concentration profiles, as shown by the model reaction front continuously widening due to the simulated porosity and diffusivity enhancement. Therefore a threshold model based on the idea that dissolution and porosity enhancement increase the rate of diffusivity by increasing connectivity (Navarre-Sitchler et al., 2009; 2011), was determined to be more appropriate.

The dissolution of the glass is assumed to follow an affinity rate law (Grambow, 2006), but with a cubic dependence on the saturation state (departure from equilibrium) with respect to amorphous silica. A linear Transition State Theory (TST) dependence does not capture the sharp B front and places the B (and Na) dissolution front closer to the Li-H interdiffusion front. The rate of glass corrosion, in addition to following a cubic dependence on the departure from equilibrium, also depends on the hydration state of the glass. In other words, if the H<sub>2</sub>O diffusion front has not yet penetrated the pristine glass, the rate is effectively zero. So the rate law used is given by

$$R_{corr} = k a_{H-hydrated}^5 \left( 1 - \frac{Q_{am-silica}}{K_{am-silica}} \right)^3 \quad \text{Eqn 2.2-(1)}$$

where  $k$  is the rate constant and  $a_{H-hydrated}$  is the concentration of hydrated sites in the glass, and  $Q_{am-silica}$  and  $K_{am-silica}$  are the ion activity products and equilibrium constants with respect to amorphous silica. A higher-order dependence on the concentration of hydrated sites in the borosilicate glass is also required so as to locate the boron release front further from the Li-H interdiffusion front. This formulation could be reconciled with a model in which the number of hydrated sites needs to reach some threshold value before the dissolution of the glass accelerates appreciably.

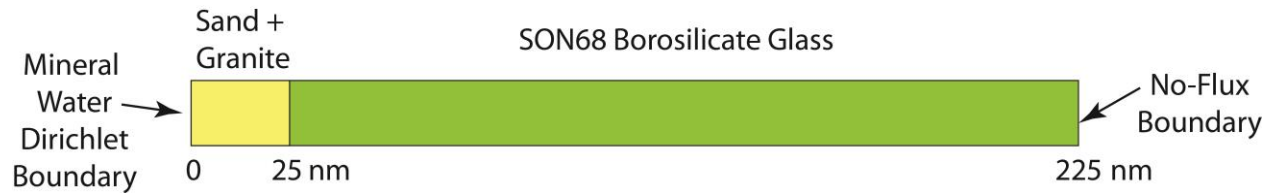


Figure 2.2-2. Schematic of modeling setup showing nanometer-scale reaction and diffusion zones.

## 2.2.4 SIMULATION RESULTS

In the simulations presented here, we present a semi-quantitative comparison of the modeling results and the data. In the modeling, concentration in the pore solution, rather than in the glass, is presented, so a quantitative comparison is not possible. The focus is on the relative position of the fronts, and in general, the width of the fronts as they evolve over time. Schematically, the geometry that we wish to capture in the modeling is given in Figure 2.2-3 taken from Gin et al. (2013). Most important is the relatively constant width of the reaction zones and the position of the sharp boron profile further from the pristine glass interface than is the Li-Water inter-diffusion zone. A more detailed Atom Probe Tomography (APT) profile from Gin et al. (2013) is given in Figure 2.2-4.

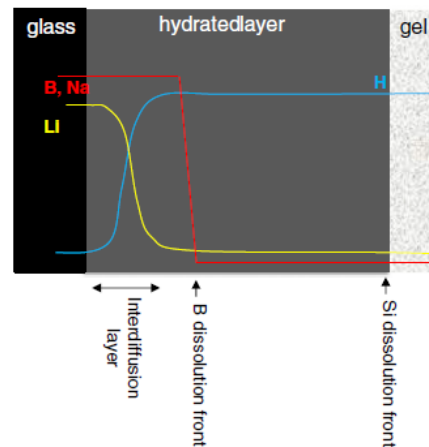


Figure 2.2-3. Figure 3: Schematic of the disposition of elemental leaching zones based on atom probe tomography (from Gin et al., 2013).

The model results for the 1D run are shown in Figure 2.2-5 over a period of 4 years. Larger times than these require extending the grid (and the borosilicate glass) to larger distances, which will be presented in subsequent reports. The modeling results show that both the Li-H inter-diffusion front and the B release (dissolution) front are relatively sharp, and remain so over the course of the 4 year simulation. In addition, the B release front is located further from the pristine glass interface than is the Li-H inter-diffusion front, which makes sense insofar as the dissolution of the glass is promoted by its hydration.

In addition, the simulations predict a linear rate of front propagation over time once the initial period (less than 1 year) is passed (Figure 2.2-6). This can be explained by the maintenance of a constant-width zone over which diffusion is limiting (in agreement with the results of Navarre-Sitchler et al., 2011). Again, if the silica-rich gel layer were limiting, the dependence on time would be parabolic since this zone grows with time (Figure 2.2-7).

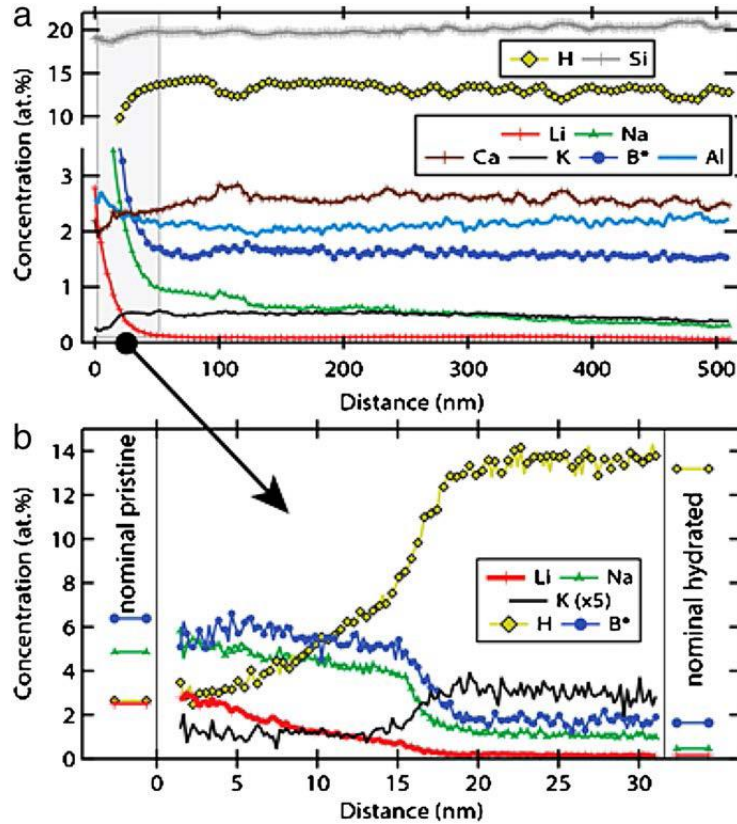


Figure 2.2-4. High resolution concentration profiles of elemental abundance across the pristine glass-hydrated glass interface (from Gin et al., 2013).

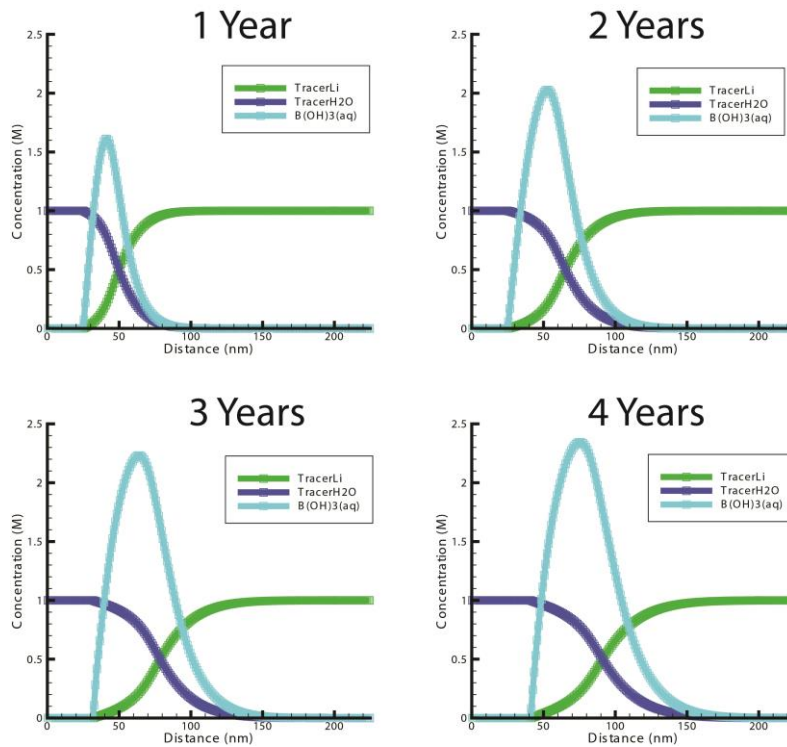


Figure 2.2-5. Simulation results using the  $K\mu C$  model. Note the position of the B release front further from the pristine glass than the Li-H interdiffusion front, in qualitative agreement with the observations.

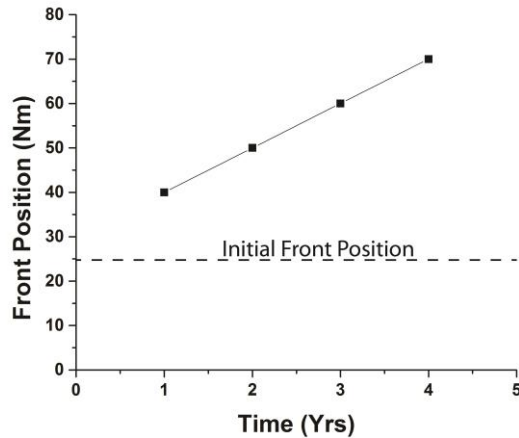


Figure 2.2-6. Simulated corrosion front position versus time. Note the linear (constant) rate of front propagation.

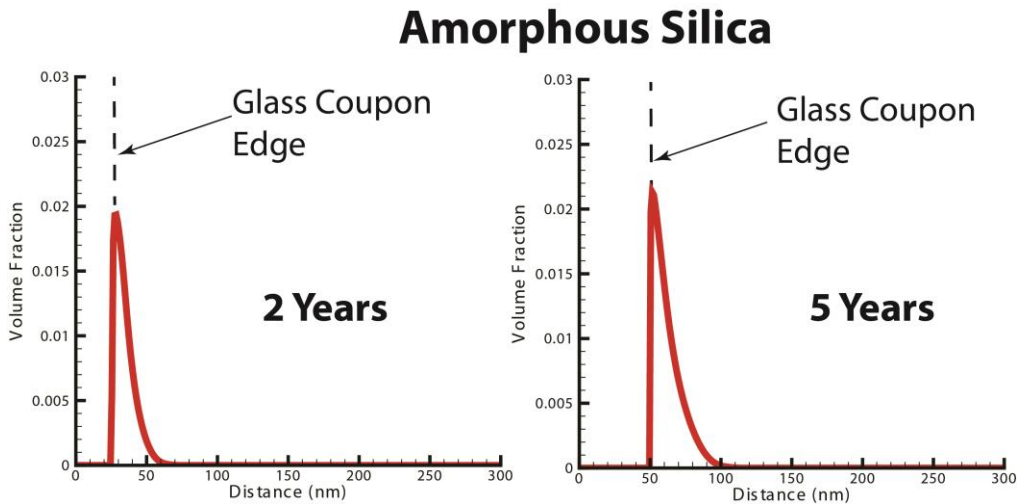


Figure 2.2-7. Simulated distribution of amorphous silica reaction product at 2 and 5 years.

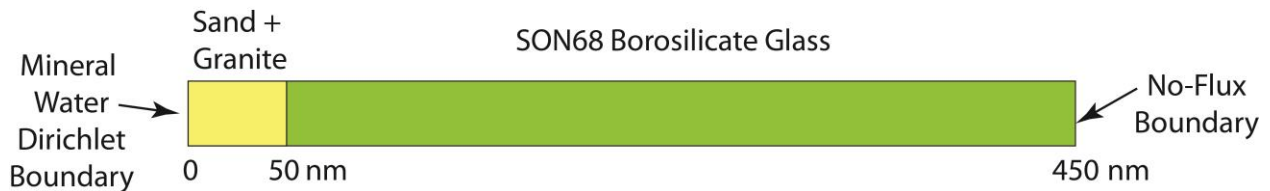


Figure 2.2-8. Schematic of modeling setup showing nanometer-scale reaction and diffusion zones used in comparative silica boundary condition simulations (see Figure 2.2-9).

Another potential effect has to do with the concentration of the external pore fluid, which is particularly important since the glass coupon in the 26 year experiment shows very different corrosion rates depending on position within the reactor. In these simulations, the grid spacing has been changed so that the glass coupon begins at 50 nm (as in Figure 2.2-8, in contrast to the 25 nm shown in Figure 2.2-2). Since the external fluid in the reactor was not well-mixed, it appears that diffusion gradients developed within the reactor. If the concentration of silica (the

principal component known to inhibit glass corrosion) is lower close to the preconditioning vessel where the corrosion distances were greatest, then this suggests that slower corrosion rates at the top of the reactor may have been due to higher silica concentrations there.

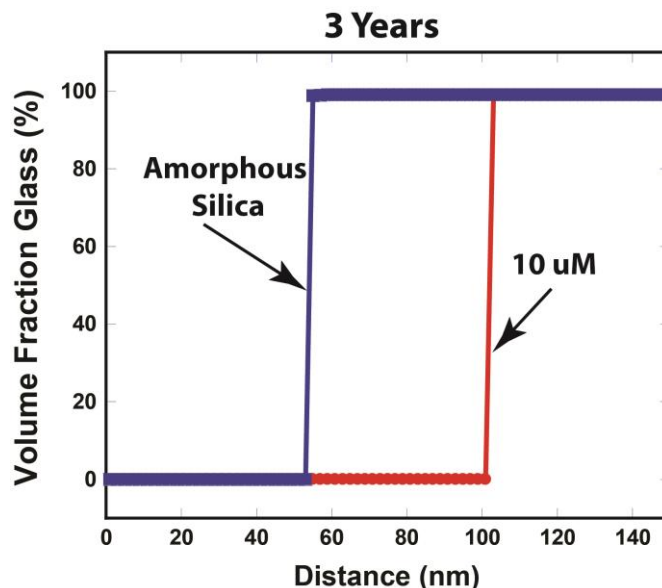


Figure 2.2-9. Effect of silica concentration in external fluid at 3 years. In these simulations, the glass coupon begins at 50 nm (Figure 8), which indicates that almost no glass corrosion is predicted when the external solution is at saturation with amorphous silica.

Using the K $\mu$ C model, we compare two different simulations (Figure 2.2-9). The first simulation was run using 10  $\mu$ M silica in the preconditioning vessel; whereas the second was run with the preconditioning vessel fixed at amorphous silica saturation (1936  $\mu$ M). In these simulations, the glass coupon begins at 50 nm, so the amorphous silica boundary condition results in very little glass corrosion. In contrast, corrosion depths are greater in the case of the 10  $\mu$ M silica boundary condition.

## 2.2.5 DISCUSSION

To the extent that the simulations agrees with the observations of the sharpness of the reaction fronts, the non-coincidence of the B and Li-H fronts, and the constant (linear) rate of corrosion, they support the conceptual model proposed by Gin et al. (2013). The rate-limiting step for corrosion appears to be the rate of diffusion of H (via water) into the pristine glass. The slow rate of diffusion, which is approximately  $10^{-23}$  m<sup>2</sup>/s, controls the overall rate of glass corrosion. An explicit Passive Reactive Interface (PRI) zone is not required. Moreover, the linear rate that is predicted by the simulations follows from the fact that the amorphous silica gel corrosion layer that forms on the glass is not itself a diffusion barrier. If it were, one would observe a parabolic dependence on time for the corrosion rate in the simulations and experiments, since the width of the diffusion barrier would grow with time in this case (Figure 2.2-7). A linear rate of advance is only possible when the width of the diffusion barrier remains approximately constant, in agreement with Navarre-Sitchler et al. (2011).

The conceptual model for glass corrosion based on modeling of these experiments needs to involve one in which H diffusion into the glass is coupled to glass dissolution. Once the glass is hydrated, the rate of dissolution is relatively fast, as indicated by the relatively large rate constants required, as well as by the sharpness of the dissolution front. Before hydration occurs, however, the borosilicate glass corrosion is effectively zero. So the proposed model is one in which diffusion into the pristine glass, which leads to

hydration and ion exchange, is coupled to glass corrosion. The rate must depend on the extent of hydration (going from effectively zero at low hydration to very high rates when hydration is more nearly complete).

Another effect explored here has to do with the effect of the chemical composition of the external diffusion, effectively the boundary condition for the diffusion-reaction calculations. The major effect is likely to be from silica concentration based on previous studies documenting its inhibiting effect on corrosion. Since dramatically different corrosion rates were observed on the SON68 glass coupon as a function of position within the reactor, with the slowest rates observed at the top farthest from the connection to the preconditioning vessel (Figure 2.2-1), it appears that strong chemical gradients developed in the reactor (which was not mixed). The simulations presented here in Figure 2.2-9 support the idea that solution composition closer to equilibrium with respect to amorphous silica will result in slower glass corrosion rate. This highlights the importance of coupling performance assessment models of glass corrosion with larger scale calculations to provide the boundary conditions for the waste packages.

## 2.2.6 References

- Bourg, I.C., C.I. Steefel (2012). Molecular dynamics simulations of water structure and diffusion in silica nanopores. *J. Phys. Chem., C* **116**, 11556-11564.
- Cailleteau C., F. Angeli, F. Devreux, S. Gin, J. Jestin, P. Jollivet, O. Spalla (2008). Insight into silicate-glass corrosion mechanisms. *Nature Materials*, **7**, 978-983.
- Frugier P., S. Gin, Y. Minet, T. Chave, B. Bonin, N. Godon, J-E. Lartigue, P. Jollivet, A. Ayrat, L. De Windt, G. Santarini (2008). SON68 nuclear glass dissolution kinetics: Current state of knowledge and basis of the new GRAAL model, *Journal of Nuclear Materials*, **380**, 8-21.
- Grambow, B. (2006). Nuclear waste glasses – How durable? *Elements*, **2**, 357-364.
- Gin S., J.Y. Ryan, D.K. Schreiber, J. Neeway, D. Cabie (2013). Contribution of atom-probe tomography to a better understanding of glass alteration mechanisms: Application to a nuclear glass specimen altered 25 years in a granitic environment. *Chemical Geology*, **349-350**, 99-109.
- Gin S., C. Guittonneau, N. Godon, D. Neff, D. Rebiscoul, M. Cabie, S. Mostefaoui (2011). Nuclear glass durability: New insight in alteration layer properties. *Journal of Physical Chemistry, C* **115**, 18696-19706.
- Guittonneau, C., S. Gin, N. Godon, J.P. Mestre, O. Dugne, P. Allegri (2011). A 25-year laboratory experiment on French SON68 nuclear glass leached in a granitic environment—First investigations. *Journal of Nuclear Materials*, **408**, 73-89.
- Navarre-Sitchler A., C.I. Steefel, L. Yang, L. Tomutsa, S.A. Brantley (2009). Evolution of porosity and diffusivity associated with chemical weathering of a basalt clast. *Journal of Geophysical Research*, **114**, DOI:10.1029/2008JF001060.
- Navarre-Sitchler, A., C.I. Steefel, P.B. Sak, S.L. Brantley (2011). A reactive transport model for weathering rind formation on basalt. *Geochimica Cosmochimica Acta*, **75**, 7644-7667.

## 2.3 Glass Degradation Modeling Tool

The Glass Corrosion Modeling Tool (GCMT) allows the user to evaluate the goodness of a glass degradation model by fitting the model to a selected experimental dataset. The GCMT returns the best estimate of the model parameters. The GCMT allows comparison of different models and ultimately allows a statistical method of choosing the best possible model. By this means researchers can understand how particular models succeed or fail in explaining certain results and allow them to modify the models on a rational basis. Engineers can use the tool to quantitatively justify the choice of a certain model of glass dissolution and the associated parameters values used in the model. Those models can then be used in codes used to predict the durability and lifetime of nuclear waste glass. The information in this Section comes from milestone: M4FT-14PN0804045 generated in work package FT-14PN080404.

The GCMT consists of a set of software packages that interact to statistically optimize key parameters, such as rate constants or activation energies, in a glass alteration model to a selected set of experimental data. Glass alteration data imported into the GCMT may be of any type provided the model is capable of predicting those data. Four databases are current supplied with the tool.

Within the GCMT, the user can choose to implement various models such as the Aagaard-Helgeson (AH) model with residual rate, the Grambow-Muller (GM) model and the Glass Reactivity with Allowance for the Alteration Layer (GRAAL) model. Additionally, a new model is being developed to predict depth profiling data provided by Time of Flight, Secondary Ion Mass Spectrometry (TOF-SIMS) and Atomic Probe Tomography (APT) studies. The Aagaard-Helgeson (AH) model (Aagaard and Helgeson, 1982) was developed to describe mineral dissolution, is based upon kinetic rate theory of activated complexes (Eyring, 1935; Laidler, 1983), and has been applied to glass alteration more recently (Gin et al., 2008). The AH model is reasonably successful in accounting for many dissolution data and was used by Pierce et al. (2004; 2008) to interpret the results of their glass dissolution study. The Grambow-Muller (GM) model was developed to account for the possible formation of a barrier gel layer that hinders water transport (Grambow and Muller, 2001). The GM model uses the AH model for the dissolution rate of the pristine glass, upon which forms an interface covered by an amorphous layer formed by multiple processes including selective dissolution of some elements from the glass and precipitation of silica gel. This gel layer impedes diffusion of dissolved species such that the rate of glass dissolution at the pristine interface becomes limited by, and equal to, the diffusion rate through the gel.

Combining more coupled processes throughout the glass degradation regime, the GRAAL model (Frugier et al., 2008; 2009; Minet et al., 2010) represents the exterior layer of glass as dissolving at a rate based on chemical affinity, similar to that given in the AH model. Outside of the pristine glass a series of zones form with very narrow (nanometers) zones where only hydration and alkali inter-diffusion take place, followed by an additional layer that is formed from hydrolysis and leaching of the glass (the passivating reactive interface, PRI), with formation of depleted gel beyond it. The PRI thickness is from a few nanometers to a few hundred nanometers. Overall rate control of glass degradation may shift from purely forward dissolution of the glass, to diffusive rate limitations especially while the PRI is non-reacting.

For a given choice of database and model, the GCMT repeatedly implements the model solver until the statistical fitting package determines the best estimate of the parameters has been found. The model solver may be a simple code of a few lines embedded in the GCMT or it may be an advanced computational fluid dynamics code interacting with a chemical kinetics and thermodynamics package. Complex geometries or experimental configurations may be evaluated.

### 2.3.1 Development of a GUI for the ALTGLASS database

A graphical user interface (GUI) was constructed for easy access to the very large ALTGLASS database put together by Carol Jantzen at Savannah River National Laboratory. ALTGLASS contains a wealth of information for each experimental point including the glass oxide composition, the leachate concentrations, temperature, flow rate, pH etc. Some 68 values are reported for each for the nearly 2000

experiments. This makes it very difficult to parse through the database and find similar experiments or identify possible trends. In addition the ALTGLASS database could provide a useful input to the GCMT provided there was a convenient way to select desired data. Towards this end, a GUI for ALTGLASS was constructed using MatLab (<http://www.mathworks.com>). The GUI allows any of the 68 values to be narrowed by either text value, e.g. sample ID, or by numerical value, e.g. leachate pH. After down selecting desired datasets, the values can be plotted for visual examination. The data sets can then be imported into the GCMT. Details for its use are covered in the GCMT User Manual.

The ALTGLASS database contains mostly single-pass, flow-through (SPFT) test data taken at one, or at most a few, sampling times. Hence it lacks important information necessary to develop new chemistry and physics based models. However the database covers a very wide range of glass compositions and could allow rate constant to be expressed in terms of glass composition. The glass corrosion model to be used for the radionuclide source term in the Performance Assessment (PA) model is still being developed. The ALTGLASS database used in the GCMT allows for specification of, and testing of, a generalized yet simplified glass corrosion model that may be useful for PA models.

### 2.3.2 Addition of Depth Profile Databases

Glass alteration has been characterized in detail using TOF-SIMS and APT experimental techniques to quantify the depth profiles of elements (e.g., Na, Li, B, Al, Si) in leached SON68 glass. Further an isotopic swap technique allowed ambiguities in the time evolution of the elemental distributions to be resolved. The leachate elemental concentrations were also determined using ICP allowing the results to be compared with other leaching data such as that in the ALTGLASS database. Our intent is to utilize the GCMT to quantitatively analyze this data. However, the datasets are very large, not particularly amenable to direct importation and the signal intensities do not represent mole fraction units needed in the models in GCMT. MatLab was used to import the experimental data files and select, convert, and organize the important numerical information.

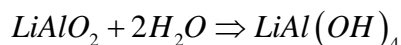
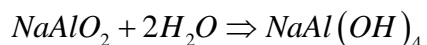
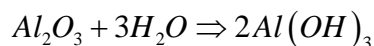
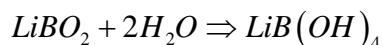
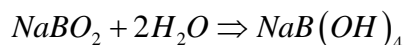
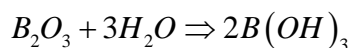
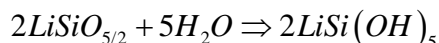
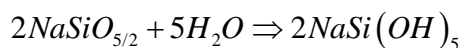
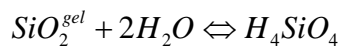
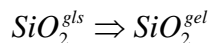
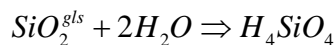
More importantly each data set was also converted to a value representing the local elemental mole fraction. To date we have reduced the importation of the TOF-SIMS and APT data to a series of numerical steps that allow adjustment of the “calibration” process. This has been completed for the TOF-SIMS data and an example of the data is discussed below. The APT data sets have been collected and imported in the original numerical form and we are in the process of converting the signal intensity data to mole fraction data. Generally speaking the first steps are to account for instrumental artifacts and then to normalize the data to the known composition of the pristine glass. The TOF-SIMS and APT data have associated data (via ICP analysis) for the leachate solutions. Each of these analytical techniques has a numerical uncertainty associated with the signal acquisition process and the data calibration process. These uncertainties are being converted to an appropriate weighting factor for input into the Parameter Estimation Software Package (PEST) optimization module in the GCMT.

### 2.3.3 Formulation of a Model to Predict Depth Profile Data

The detailed concentrations with depth (i.e., profiles) data described above are not readily modeled using the existing glass corrosion models included in the GCMT. It is noted that the AH, GM and GRAAL models all assume the formation of one or more layers and/or interfaces to predict the rate at which the mass of glass is leached into solution, but it is not clear that these models predict how these interfaces are formed in as much detail as is shown within the K $\mu$ C model (Section 2.2).

A new model was formulated and implemented in the GCMT in an effort to provide an idealized method for predicting the formation of such interfaces within a continuous medium. The model is based upon an extensible set of chemical reactions with these reactions forming species that may then diffuse out of the glass and be leached into the solution. Hence this model is referred to here as the Diffusive Chemical Reaction (DCRx) model. A brief review of the primary assumptions behind the model is given below with a description of the main chemical constituents considered.

The set of chemical reactions considered here are



The immobile species found in glass (as determined from NMR data for example) on the left side of these stoichiometric equations react with water, to form neutral or ion pair species. These species - on the right of the equations - are, along with water, assumed to be mobile. The model is extensible in that new secondary or intermediate reactions can be added as needed to explain experimental data. For example, this current version of the model clearly ignores the formation of ionic species but provides a set of reactions that encompass those chemical possibilities. Although the species in this model may be more applicable at high pH values, additional complexity of dissolved silica, boron, alkalis, and aluminum species would likely exist in the solution. This idealized approach does not explicitly address solution chemistry of the species, rather it uses the above simple set of reactions to account for diffusive transport.

In addition, the diffusivity of various species is assumed to be impacted primarily by the local concentration of water with a minimal diffusivity as determined by solid state diffusion in the “dry” or pristine glass. This allows transport of most species to be described by simple Fickian diffusion except that of water. This diffusivity of each species may be described by a power dependence of diffusivity on water content such as

$$D_i = D_i^0 \left( X_{\text{H}_2\text{O}} \right)^n + D_i^{gls}$$

where  $X_{\text{H}_2\text{O}}$  is the local mole fraction of water,  $D_i^0$  is the diffusivity in pure water, and  $D_i^{gls}$  is the diffusivity in dry glass. There are other rational approaches to determine the diffusivity but this discussion is beyond the scope of this report and we believe this is an adequate approach until the set of relevant chemical reactions is more clearly defined.

Water in this model is unique in that it is assumed to: (1) be the species diffusing into a region left vacant by any other diffusing species (i.e., as  $\text{H}_4\text{SiO}_4$  diffuses out of the glass,  $\text{H}_2\text{O}$  can diffuse into it); and (2) diffuse into dry glass using a free volume model. This significantly simplifies the transport and source terms in the partial differential equations (PDE) needed in the model.

These transport and source equations were implemented as a COMSOL (<http://www.comsol.com>) file that can be initiated through MatLab. Selected TOF-SIMS data were then fit by optimizing the model parameters using the GCMT. More details of the results are discussed below.

The DCRx is a model of glass dissolution that specifies which fundamental physical transport equations are used, the approximations that may be made, the set of chemical reactions and species being considered and the dependence of diffusivity on local composition. It is often a challenge to determine what equations are being used in other “continuum” models of glass alteration. The DCRx is based upon a set of PDEs describing fundamental physics and chemistry of a simple set of idealized species, and it is an extensible model. Any simplification can be addressed or additional chemical reactions added as needed to this initial idealized version. This may allow more flexibility than the AH, GM and GRAAL phenomenological models (see above) which, although they may predict the correct dissolution rate of the glass, in some cases extend their governing equations beyond their applicability or impose non-physical assumptions on the rate of dissolution. It is a challenge to modify these other models in light of new experimental evidence.

### 2.3.4 Modeling Depth Profiling Data

Single pass flow through (SPFT) was used in combination with isotopic labeling experiments and TOF-SIMS and APT analysis techniques to characterize the corrosion of nuclear waste glasses. These have provided unparalleled nanometer resolution depth profiles of the elemental distributions within the glass. Above we briefly outlined the DCRx model and report here on the initial analysis of the TOF-SIMS data using the GCMT to fit the model parameters.

Figure 2.3-1 illustrates how the DCRx model in GCMT was used to model TOF-SIMS data and the associated chemical reaction set. In brief, the DCRx model does an adequate job of explaining Na, Si and

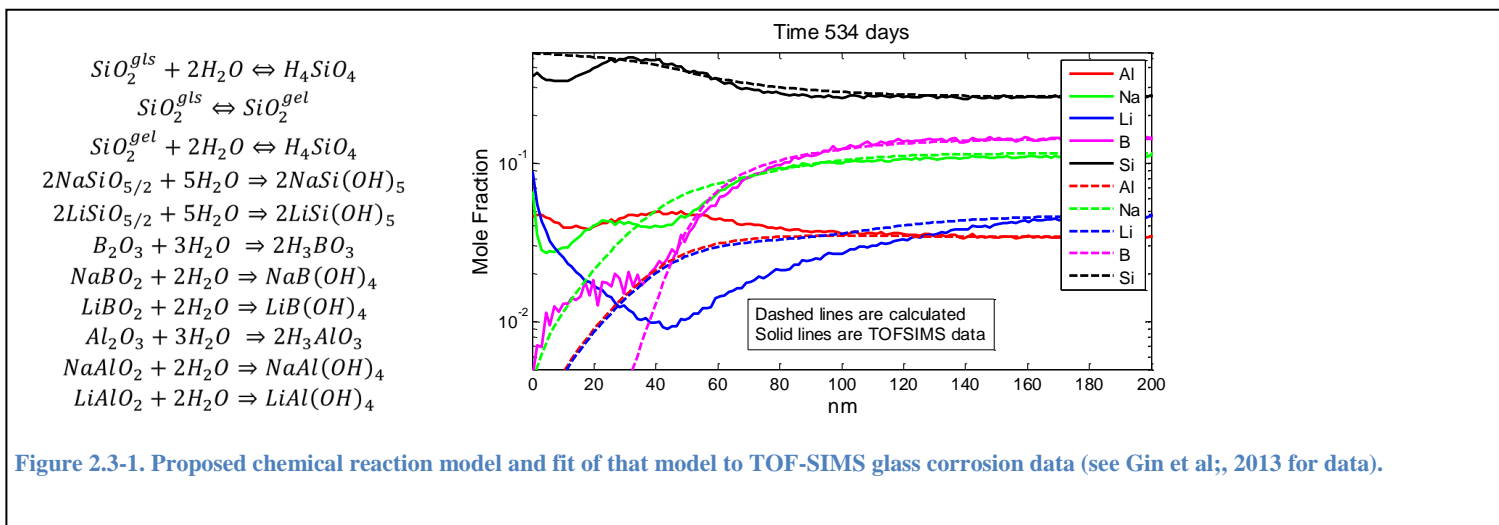


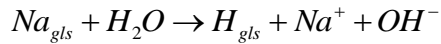
Figure 2.3-1. Proposed chemical reaction model and fit of that model to TOF-SIMS glass corrosion data (see Gin et al., 2013 for data).

B leaching but fails to even qualitatively describe how Al and Li are leached from the glass. To remedy this deficit, the model will need to be modified to account for more realistic species behavior such as how  $Al(OH)_4^-$  and/or related Al species are bound to the leached portion of the glass. While Li is not expected to bind strongly to leached glass, the comparison of model and data suggest that solid state diffusion may be important for Li because of the mismatch of the model to the data at less than 40 nm.

We note that TOF-SIMS is considered semi-quantitative because of unknowns in the sputtering rate. However these results illustrate that even a poor qualitative fit provides significant information on how to modify the proposed dissolution mechanism and an improved model can be proposed and tested with the GCMT. This basic model and improved models will be more fully tested once the ICP and APT databases can be fully accessed by the GCMT.

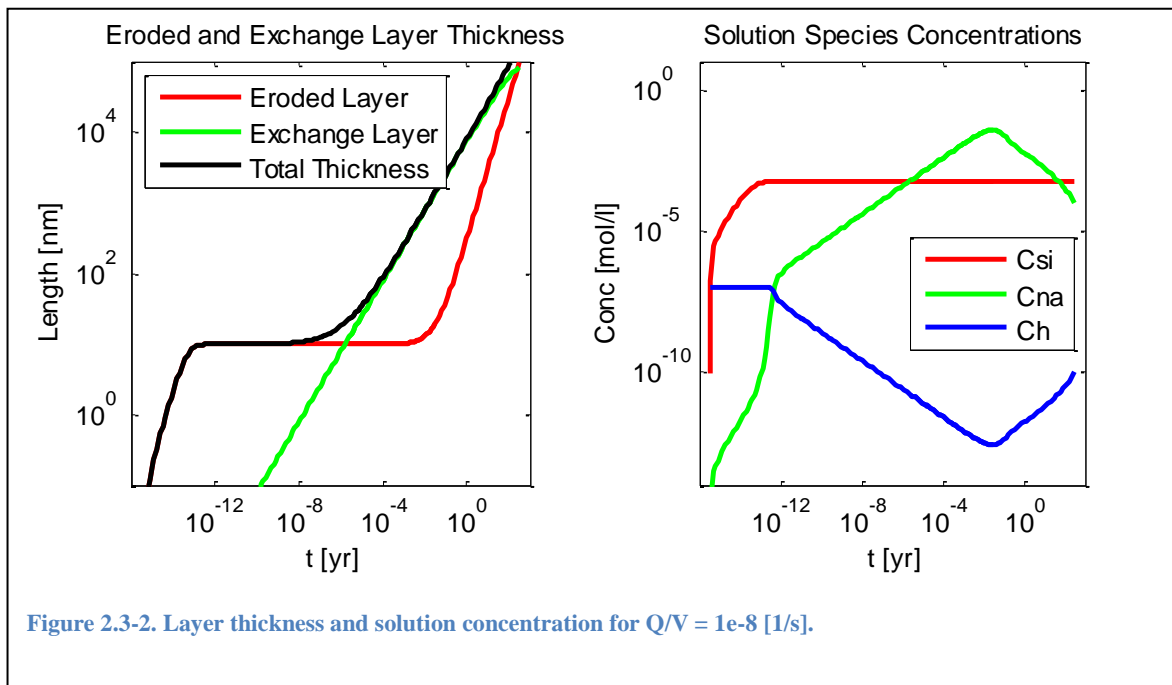
### Residual Rate Effects in ILAW Glasses

Additional consideration is being given to experiments to study corrosion of Immobilized Low-Activity Waste (ILAW) glasses. The role of “Residual Rate” corrosion is important in this task and to address this issue the GCMT was used to compare the Constant Residual Rate (CRR) and the GRAAL models. Both assume the exterior layer of glass is eroded (i.e. completely dissolved) at some rate controlled by the pH in solution as well as the degree of saturation with respect to a silica gel phase. They differ in that a second term describing how the glass is more easily leached of some species, such as Na and B, leaving behind an altered layer. In this instance, investigation focused on the ion exchange process



in which the release of sodium results in a rise in the pH of the solution that may increase the rate of glass dissolution.

Figure 2.3-2 shows a typical result for analysis of the GRAAL model using rate constants reported by Bacon and McGrail (2005) for LAWA44 glass. The objective here was to explore if the exchange layer growth influences the eroded layer thickness. Elements of interest such as radionuclides will be released depending upon how strongly they bind to glass. Technetium, for example, will bind strongly to glass and its release will follow a pattern similar to that of silicon. Cesium on the other hand, being singly charged, is expected behave similar to sodium. This behavior is a result of the GRAAL model representing release of these elements as two congruent release patterns. In reality each species would be released from the



exchange layer in a slightly different manner and thus would not be entirely congruent with each other.

From these results, the release of radionuclides may or may not be associated with the residual rate as determined by the exchange layer growth rate. It can be seen that ion exchange is related to pH change, but the degree of super-saturation of aqueous silica is more directly related to the precipitated silica phase from the alteration. In the limited solution chemistry model used here, pH does not have a major influence on the rate of dissolution even though there is direct correlation to the Na exchange.

### 2.3.5 Examples of GCMT Uses

Note that the GCMT is a set of MatLab routines that makes calls to other software packages and was developed using MatLab. Contact Dr. Peter Rieke, PNNL to obtain the GDMT and for additional information on other modules required. For basic operation of the GCMT the basic MatLab package should be adequate. The parameter optimization package, PEST, can be obtained free from <http://www.pesthomepage.org/Downloads.php> . Version 13.0 was used in this work.

The AH and GM models are implemented as MatLab routines and no additional software are required to analyze these models but the user has the option of using PhreeqC with the IPhreeqC module obtained from [http://wwwbr.cr.usgs.gov/projects/GWC\\_coupled/phreeqc](http://wwwbr.cr.usgs.gov/projects/GWC_coupled/phreeqc). Only the IPhreeqC module is needed but the PhreeqC and GUI packages can be useful in understanding how PhreeqC works. To use the GRAAL and DCRx models the user needs the “m” or MatLab version of the files for the GCMT implementation controlled by MatLab. The basic COMSOL and MatLab LiveLink package are needed also for this. These can be obtained from COMSOL at <http://www.comsol.com> . Although some databases may be obtained directly with the GDMT, the ALTGLASS database has not yet been formally released and is not included.

#### 2.3.5.1 Example1. Optimizing the AH model against LAWA44 SPFT data

The AH model is the simplest possible model of glass dissolution and is often used to characterize SPFT data at a single time point. In this example we step through the GCMT main code and explain what each feature does. MatLab, IPhreeqC, and PEST are required to run this example. The following steps are outlined and also shown in their script file format below this listing:

1. Initialize() deletes all files created in any possible previous analysis and sets paths
2. getPNNL14805data() gets all the SPFT data for three glass compositions which are contained in a Excel spreadsheet 'PNNL14805\_AppA\_SPFT\_data.xlsx'. The original data was reported in grams of glass dissolved per unit surface area. This data is back converted to the original moles per unit volume that would have been present in the contacting solution. It also returns information on the glass composition and a list of molecular weights. Only the LAWA44 data is used in further analysis.
3. SelectDataSubset(SPFT, irange) selects certain experimental sets as determined by irange and this can be amended by the user. It also eliminates any data that does not contain all four Si, Al, Na and B concentrations.
4. calcIAP\_aH\_wPhreeqc(GlsComp, MW, SPFT, Exp\_, nExp) uses Phreeqc and the reported solution concentrations to calculate the ion activity product (IAP) and the hydrogen activity needed in the AH model. It adds these data to the SPFT array but only for experiments in the irange.
5. writeParamFiles(par) takes the initial guess at the parameters values (etta, Ea, k and K<sub>gls</sub>) and writes these to a file “initialParam.dat” and also makes a copy “estimatedParam.dat” for use by pest.
6. firstRun(GlsComp, SPFT, Exp\_, nExp, fnPar) runs the model using these initial guesses and writes a file that can be read by PEST and compared to the experimental data.
7. writePCFinputFile() writes a file containing the experimental data in the same format as the firstRun file output above but this file becomes part of the larger PEST Control File (PCF).
8. initCheckPestFiles(FileNameXLSX, SheetNameXLSX, nPar, nObs) uses a series of templates to prepare the PCF. It uses an Excel file 'PCF/PCF\_Input\_All\_AH.xlsx' to input needed values. The rather cumbersome PEST setup routine is avoided and automated by this process. The routine runs PEST routines that check for a correct file format.

9. `initHandShaking()` ensure that certain signal files created by MatLab and PEST are not present.
10. `runPestModel(fnPar, SPFT, Exp_, nExp, GlsComp)` starts PEST in the background using `getML.exe` to get the model results. `getML.exe` does not actually start the model but loops until a signal file is created by MatLab denoting that new model results are available. After starting PEST, the MatLab routine then falls into a continuous loop that looks for a signal file from PEST indicating that new parameter values are available. It then executes the AH model and writes a new data estimate file. The process continues until PEST determines the best parameter estimate has been reached and ceased to write a new parameter estimate file. If MatLab determines that no new parameter file is present after a suitably long time,  $\sim 10X$  that required to solve the model, it also terminates and reports the results in the data structure AH.
11. `Plot_AH(GlsComp,AH,SPFT, nExp, Exp_)` then creates four plots of the data and the AH with the best parameter estimate for four different temperatures.

The plots are reproduced in Figure 2.3-3 below for easy comparison

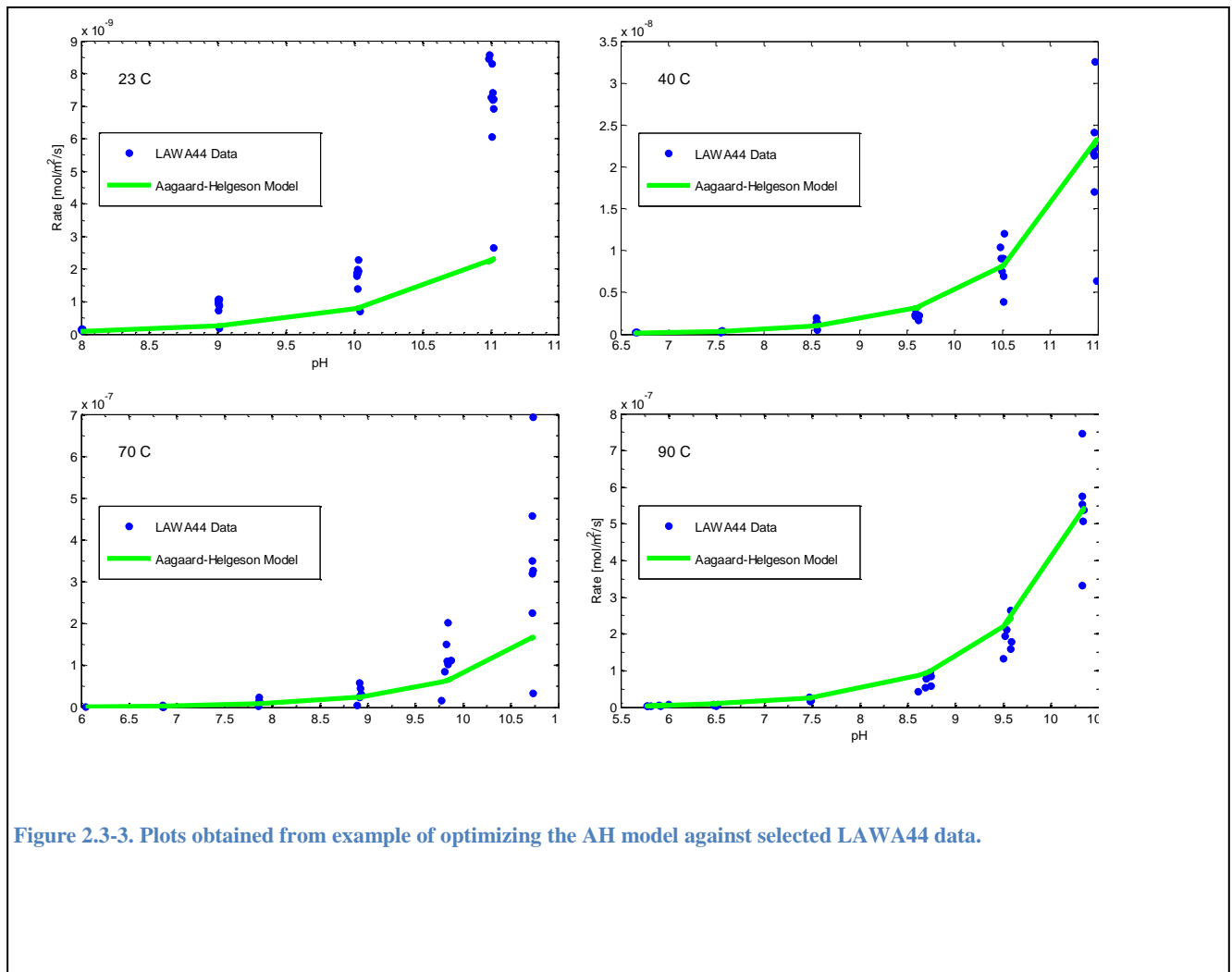


Figure 2.3-3. Plots obtained from example of optimizing the AH model against selected LAW A44 data.

Script file listing of the steps given above:

```
% Initialize MatLab and Paths
clear all; close all;
```

```

Initialize()

%% Import data from 'PNNL14805_AppA_SPFT_data.xlsx'
[GlsComp, MW, SPFT] = getPNNL14805data();

%% Select data subset for analysis, write to 'selectedMeas.dat'
irange = [08 39 51 45 ...
          09 40 52 46 ...
          12 41 53 47 ...
          14 42 54 48 ...
          16 43 55 49 ...
          44 56 50];
[Exp_ nExp] =SelectDataSubset(SPFT,irange);

%% Phreeqc Calc. of IAP and a_H for each data set in irange
[SPFT] = calcIAP_aH_wPhreeqc(GlsComp, MW, SPFT, Exp_, nExp);

%% Write 'inititalParam.dat' 'estimatedParam.dat' 'PCF/PCF_Param_Data.input'
'PCF/PCF_Param_Gps.input'
% 'inititalParam.dat' is copied to 'estimatedParam.dat' initial for use by PEST.
clearvars par; % prevents inadvertently adding anything to this later on ??
par.etta = 0.5; % H+ power coefficient
par.Ea = 60.0*1e3; % kJ/mol -> J/mol
par.k = 1.3e4/(MW.LAWA44*24*3600); % g/m2/d -> mol of glass/m2/s
par.Kgls = 5.45e-4*1e3; % glass equil coef, mol/L -> mmol/kgw

[fnPar, nPar] = writeParamFiles(par);

%% 1st model run on 'estimatedParam.dat' output to 'initialModelOutput.dat' and copied
to 'estimatedModelOutput.dat'
[nObs] = firstRun(GlsComp, SPFT, Exp_, nExp, fnPar);

%% Write 'PCF/PCF_Obs_Data_Synth.input'
writePCFinputFile()

%% Initialize Pest Files
FileNameXLSX = 'PCF/PCF_Input_All_AH.xlsx';
SheetNameXLSX = 'PCF_Input';
initCheckPestFiles(FileNameXLSX, SheetNameXLSX, nPar, nObs)
clearvars FileNameXLSX SheetNameXLSX
fclose('all');

%% initialize Handshaking loop
initHandShaking()

%% Start Pest with getML.exe
[AH] = runPestModel(fnPar, SPFT, Exp_, nExp, GlsComp);

%% Plot the results by Temperature and pH
close all;
Plot_AH(GlsComp,AH,SPFT, nExp, Exp_);
    
```

### 2.3.5.2 Example2. Optimizing the GRAAL Model against Time Dependent SON68 Data

Example 2 illustrates how the GCMT can be used with time dependent data and a model run via the COMSOL PDE solver. The MainDriver.m file listed below outlines the general procedure. It is similar to that of Example 1 but is more complex because of the call to COMSOL. IPhreeqc is not used in this example but has been used in other cases involving COMSOL. To run this example will require MatLab, COMSOL with the MatLab LiveLink, and PEST.

The steps are as follows:

1. Initialize MatLab by clearing the workspace, deleting unneeded files and adding paths
2. User supplies the name of the particular Frugier data set by, for example, names.Exp = 'Exp\_12' and providing a "Try" number. The Try number uniquely identifies a particular run and has no other significance. Import\_Frugier\_Data\_V4() as the name suggest imports of all 12 of the SON68 experimental datasets.
3. Next the initial guess for the model parameters (rd, rh, km, D, Csatr, Cmsatr, S\_V, Q\_V, Csi\_gls, Cb\_gls) are given. In this case the values provided by Frugier are used and modified by multiplication by the vectors synthVec and guessVec using initParam()
4. The initial values for the GRAAL variables (C0si, C0b, C0m, E0, G0) are supplied. These are usually set to zero for a pristine piece of glass.
5. Then one can choose to make and fit synthetic data. Noise is added to the data. This process is primarily used to test assumptions about the model and observe the result behavior. It can also be used to test the fitting process. If makeSynthData = false then experimental data is analyzed.
6. Main\_V136() then runs the PEST GRAAL optimization process.
  - a. First a series of empty data arrays are created
  - b. The model is then run with the initial guess of the parameters to create a results file that PEST can compare to the experimental values. The process here for extracting data from COMSOL still works but COMSOL now provides better methods.
  - c. initPestFiles\_V3() creates the PCF needed by PEST
  - d. The handshaking loop in then initialized
  - e. Pest is started in the background and the MatLab wait loop is initiated.
  - f. Steps c, d, e. are identical to steps 8, 9, and 10 in Example 1 except for minor variations.
7. The data are then plotted and the workspace and figures saved.
8. The final piece of code allows the user to reload a data set and plot a figure.

An example of the plot prepared by the code is given in the Figure 2.3-4 below. Note that the GRAAL model does not do a particularly good job of reproducing this experimental data, although it reproduces

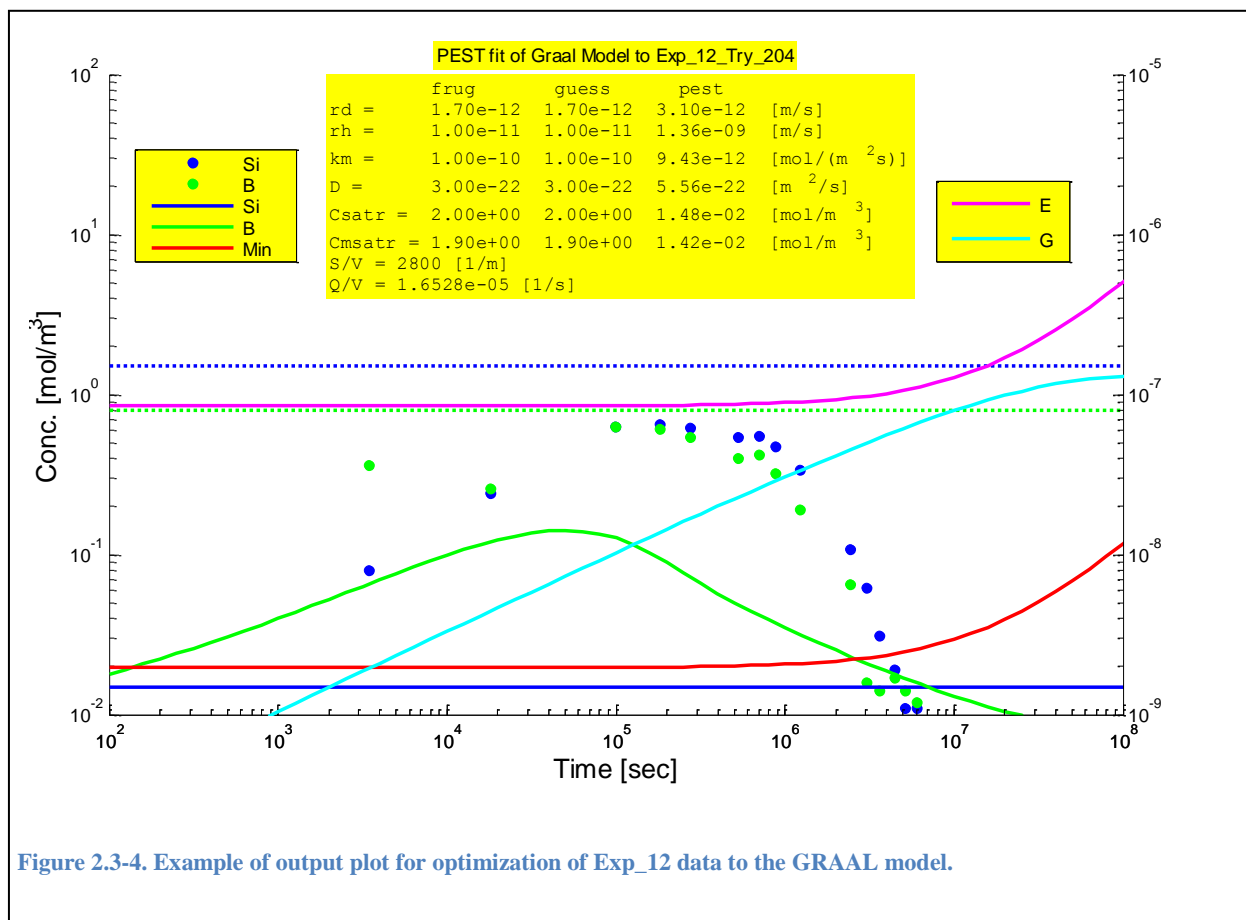


Figure 2.3-4. Example of output plot for optimization of Exp\_12 data to the GRAAL model.

other experimental results more closely.

### 2.3.5.3 Example3. GUI for the ALTGLASS database

Carol Jensen of Savannah River National Laboratory has compiled an extensive database, ALTGLASS, covering many glass leaching experiments usually of the SPFT type. The database is not yet officially released but a copy can be obtained by contacting Dr. Jensen directly. Most of the data in ALTGLASS is not time dependent but 3 or 4 times are reported for a few samples. Unfortunately this is probably not sufficient for parameter optimization with the GRAAL model and the AH and GM with or without consideration of a residual rate is probably the best choice for fitting to this database.

ALTGLASS contains a wealth of information on each experimental point including the glass oxide composition, the leachate concentration, temperature, flow rate, pH etc. Some 68 values are reported for each for the nearly 2000 experiments.

To facilitate data selection from this extensive set, a graphical user interface for ALTGLASS was constructed using MatLab. The interface to the data set is utilized in the following manner:

1. Start the code by running Main.m
2. A browser window will pop-up. Browse to the ALTGLASS database and open it
3. After a few seconds to load the database, a table of the entire database will appear as well as a window with four buttons across the top. These are:

- a. Add Column Selection
  - b. Update Selected Data Table
  - c. Hide/Show Columns
  - d. Plot Data
4. Below these appears a selection box entitled “Select a column from drop down menu” with an initial value of “None” in the drop down menu. The supplied menu represents the columns of data in ALTGLASS. Select a desired category. Depending upon whether the column contain text or numerical values a new interface will appear
    - a. For text values such as “Glass ID”, a text entry box will appear as well as a drop down menu. Either type in a value in the text entry box or select a value from the drop down menu. Once a text value is selected it will appear in the text box and may be edited. Usually one will want to shorten the text to include a series of similar data.
    - b. For numerical data such as “pH” two sliders will appear representing the minimum and maximum limits that can be selected. These can be adjusted in the conventional manner or specific values entered into the text box.
  5. Clicking the “Add Column Selection” button will add up to four selection criteria.
  6. Clicking the “Update Selected Data Table” button will create and/or update a table containing only the rows in the database matching the criteria. The criteria can be modified and then the table updated.
  7. Hide/Show Columns provide a series of tick boxes that allow one to select which columns are shown in the Selected Data Table. Click the “Update Selected Data Table” after closing the window in view the changes.
  8. After making the desired selection, the Boron concentration can be plotted versus time be clicking “Next Step Plot Data” button. Since Boron is often taken as a primary indicator of the degree of glass leaching it provides a rough manner to visualize glass alteration.
  9. A model selection box would then appear, but this not currently fully implemented. This is intended to be the interface to the GCMT as illustrated in other examples.

### 2.3.6 References

- Aagaard, P. and H.C. Helgeson, 1982, Thermodynamic and kinetic constraints on reaction rates among minerals and aqueous solutions I. Theoretical considerations. *American Journal of Science*, 282: p. 237-285.
- Bacon DH, and BP McGrail, 2005, Waste Form Release Calculations for the 2005 Integrated Disposal Facility Performance Assessment, PNNL-15198, Pacific Northwest National Laboratory, Richland, WA.
- COMSOL (<http://www.comsol.com>)
- Eyring, H., 1935, The Activated Complex in Chemical Reactions. *J. Chem. Phys*, 3: p. 107.
- Frugier, P., Gin, S., Minet, Y., Chave, T., Bonin, B., Godon, N., Lartigue, J.-E., Jollivet, P., Ayral, A., De Windt, L., and Santarini, G., 2008, SON68 nuclear glass dissolution kinetics: Current state of knowledge and basis of the new GRAAL model. *Journal of Nuclear Materials*, 380(1-3): p. 8-21.
- Frugier, P., T. Chave, S. Gin, and J.-E. Lartigue, 2009, Application of the GRAAL model to leaching experiments with SON68 nuclear glass in initially pure water. *Journal of Nuclear Materials*, 392(3): p. 552-567.
- Gin, S., Jegou, C., Frugier, P., and Minet, Y., 2008, Theoretical consideration on the application of the Aagaard-Helgeson rate law to the dissolution of silicate minerals and glasses. *Chemical Geology*, 255(1-2): p. 14-24.
- Gin S., J.Y. Ryan, D.K. Schreiber, J. Neeway, and D. Cabie, 2013, Contribution of atom-probe tomography to a better understanding of glass alteration mechanisms: Application to a nuclear glass specimen altered 25 years in a granitic environment. *Chemical Geology*, **349-350**, 99-109.
- Grambow, B. and R. Müller, 2001, First-order dissolution rate law and the role of surface layers in glass performance assessment. *Journal of Nuclear Materials*, 298(1-2): p. 112-124.
- MatLab (<http://www.mathworks.com>)
- Minet, Y., Bonin, B., Gin, S., and Frugier, P., 2010, Analytic implementation of the GRAAL model: Application to a R7T7-type glass package in a geological disposal environment. *Journal of Nuclear Materials*, 404(3): p. 178-202.
- Laidler, K.J. and M.C. King, 1983, Development of transition-state theory. *The Journal of Physical Chemistry*, 87(15): p. 2657-2664.
- Pierce EM, BP McGrail, EA Rodriguez, HT Schaefer, P Saripalli, RJ Serne, KM Krupka, PF Martin, SR Baum, KN Geiszler, LR Reed, and WJ Shaw, 2004, Waste Form Release Data Package for the 2005 Integrated Disposal Facility Performance Assessment, PNNL-14805, Pacific Northwest National Laboratory: Richland, WA.
- Pierce, E. M., Rodriguez, E. A., Calligan, L. J., Shaw, W. J., and McGrail, B. P., 2008, An experimental study of the dissolution rates of simulated aluminoborosilicate waste glasses as a function of pH and temperature under dilute conditions. *Applied Geochemistry*, 23(9): p. 2559-2573.

### 3. Metallic Waste Form Degradation Modeling

The activities for metallic waste form (Fe-Tc) degradation modeling encompass scales from the molecular-scale to the macro-scale for evaluating the corrosion of the metallic waste form and the formation of alteration phases (oxidation products) of the Fe-Tc alloy. All of these processes result in the rate at which the Fe-Tc waste form degrades and releases Tc to the solution phase, in which migration of dissolved Tc can then occur. The two model areas detailed below provide fundamental pieces of the foundation of process understanding to constrain those degradation rates. Models constraining the degradation rate behavior of the Fe-Tc waste form for use in performance assessment (PA) models are being developed within the Materials Recovery and Waste Forms (MRWF) Campaign. These activities provide process-level feeds into those additional activities in the MRWF Campaign.

#### 3.1 Fe-Tc Waste Form Modeling and Experiments

One pathway under consideration for spent nuclear fuel is to separate the various fission products and remaining fuel elements using electrochemical pyrolysis. The separated metals, including technetium (Tc) could then be alloyed together to form stainless ingots, engineered to resist corrosion over long time scales (Keiser et al., 2000; Crumm et al., 2013). The resistance of stainless metal alloys to corrosion is imparted by the formation of oxide scales that have extremely slow transport kinetics, thus constraining the rate at which material from the bulk of the alloy can interact with the environment (MacDougall and Graham, 2002). Using electrochemical testing, it is possible to examine the corrosion properties of candidate metal alloy waste forms under conditions such as variable composition, temperature or chemical exposure (Kolman et al., 2011). Experiments are constrained to relatively short testing times and a small number of possible materials/environment combinations. For this reason, it is helpful to also develop a comprehensive model based on first-principles that can be reliably applied to screen a variety of possible materials and environment combinations. The model can be used for the purposes of prediction of corrosion rates, design of alloys, and to provide fundamental insights that will complement the experimental synthesis and characterization of these candidate alloy waste forms.

In this Section, the multistep corrosion mechanism is described that is responsible for the release of Tc from any candidate alloy waste form, and the first-principles approach is outlined that will be used to build a predictive model for candidate alloy waste form corrosion, useful for both alloy design, and making long-term predictions. The materials in this Section are from milestone M4FT-14LA0804024 generated in work package FT-14LA080402.

##### 3.1.1 Predictive multistep model for the release of Tc from passive metal alloy waste forms

The dissolution of Tc alloy waste forms will follow a multistep corrosion mechanism, following the general presentation made by MacDonald's point-defect model for passive oxide films (Chao et al., 1981; Lin et al., 1981; Macdonald, 2011), as listed below (and as shown in Figure 3.1-1):

*Metal/Oxide interface:*



Transport of a metallic Tc atom into a cation vacancy site in the oxide film, leaving a vacancy in the metal site and releasing electrons (oxidation)



Conversion of a metal atom site into a cation site, with creation of an accompanying oxide vacancy and release of electrons (oxidation).

Transport of defects in the oxide:

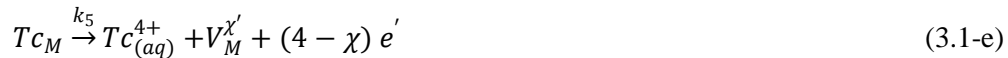


Migration of technetium cations through the oxide film. Possibly with interchange with Fe, Cr or Mo cations depending on the composition and activation barriers.



Migration of oxide anions through the oxide.

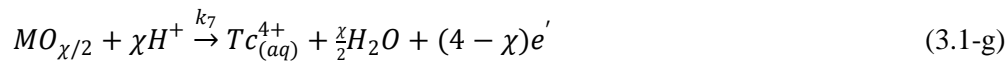
Oxide/Environment interface:



Dissolution of the metal cation from the oxide surface into solution.



Uptake of oxygen into the vacancy sites at the oxide lattice from water.



Dissolution of the metal oxide via acid-base reaction between the oxide base and acid in solution.

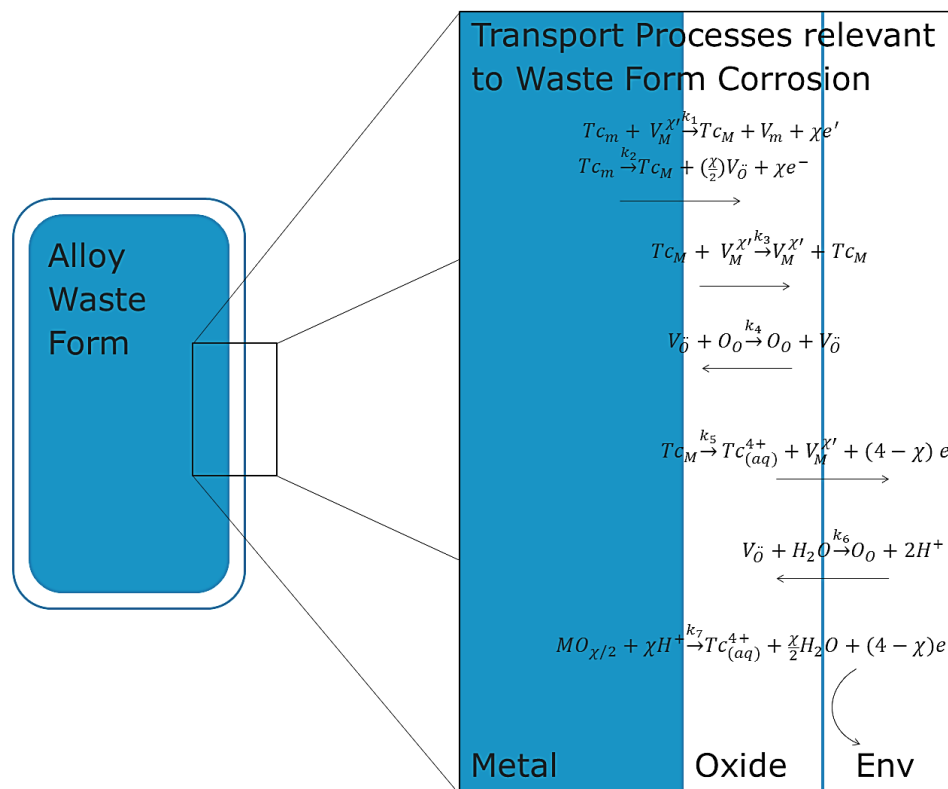


Figure 3.1-1. Schematic of multistep processes in metal alloy waste form corrosion.

The relative rates  $k_1$ ,  $k_2$ ,  $k_3$ ,  $k_4$ ,  $k_5$ ,  $k_6$  and  $k_7$  and their interdependence will determine the steady state corrosion rate of the metal alloy waste form. The slowest rate will represent the rate-determining step that will control the overall corrosion process. The rates will also be a function of the open circuit potential (OCP).

A combination of experiment and theory will be used to establish the mechanism and provide information for the rate constants  $k_1$ ,  $k_2$ ,  $k_3$ ,  $k_4$ ,  $k_5$ ,  $k_6$  and  $k_7$ . As noted in the above presentation of the mechanistic steps, for alloy waste forms, there will be multiple types of cation defect sites corresponding to the presence of different intermetallic phases, solid solutions and oxide structures. For example, if the film is predominantly  $\text{Fe}_2\text{O}_3$  above an Fe solid-solution containing Tc, then the appropriate steps likely involve the migration of Tc metal, as a defect in the bcc Fe lattice, into an Fe cation vacancy in the iron-oxide. If the oxide film is a spinel (e.g.,  $\text{Fe}_2\text{CrO}_4$ ), then the appropriate crystallographic relations and point-defects will need to be considered. The candidate alloy waste forms that have been prepared to date have a multiphase composition, which includes some ferritic phases, and Fe-Cr-Mo solid solutions. Thus the corrosion of the waste form will proceed according to the proportions of each phase that forms on the exterior surface of the alloy. Some other factors to consider are the requirement for charge balance, given that Fe ions are in a +2 or +3 state, whereas Tc prefers the +4 state. Thus density functional theory calculations or classical molecular dynamics or statics will be needed to find the appropriate defect state for Tc cations in the iron-oxide or spinel lattice.

### 3.1.1.1 *First-principles approach*

Contemporary solid-state physics allows the prediction of crystal structures for materials of arbitrary composition, including intermetallic compounds and ceramics, with a high-degree of accuracy, using the method known as density functional theory (Kresse and Furthmüller 1996; Liu et al., 2012). Not only can crystal structures be computed with this method, but also the structure and properties of point-defects, surfaces and transition states associated with the transport of defects and chemical reactions (Hafner et al., 2006; Nørskov et al., 2011; O Runevall and Sandberg, 2011). Density functional theory can be used to make these predictions because it follows the principles developed in the early 20th century for the basic quantum mechanical interactions between the atomic nuclei and the electrons that give rise to atomic structure and bonding: the principles upon which crystallography and chemical reactivity are based (Levine, 2000; Kaxiras, 2003). In this section we lay out how density functional theory will be applied to predict the kinetic parameters associated with the relevant migration processes outlined in the previous section.

#### **Characterization of point-defects**

In coordination with experimental characterization efforts, the predominant crystallographic forms for the oxide films will need to be identified and the appropriate electronic structure method (i.e. exchange-correlation functional and/or self-interaction approach) selected for modeling the crystal structure of the oxide film. The two oxides that have been identified in the Alloy Waste Form effort are hematite ( $\text{Fe}_2\text{O}_3$ ) and the iron-chromium spinel ( $\text{Fe}_2\text{CrO}_4$ ). Based on this finding, Tc migration through the oxide scale will occur through point-defects in both of these phases, and the total Tc migration will be a linear combination of the rate constants for these two phases based on their relative abundance in terms of fractional surface area of the alloy. Prior to modeling the kinetics of Tc transport, it is important to establish the equilibrium structure of Tc incorporated into these two oxide phases. This can be performed using molecular statics: that is, using a combination of density functional theory and interatomic potentials to determine the lowest energy (i.e. most likely) state for Tc to adopt as it substitutes for Fe (or Cr or Mo) in these oxide films. This approach can be used as well as to model the structure of vacancies in the vicinity of Tc, as the migration of Tc to a neighboring vacancy site is likely to comprise the transport mechanism, according to reaction (3.1-c) above. Once the reactant and product states for the migration of Tc point-defects in the oxide films have been elucidated, it will then be possible to use transition state theory to model the rate at which Tc cations will migrate within the oxide film.

It is possible that Tc will transport through grain-boundaries in the oxide film, rather than as point-defects. Although it is possible to model grain-boundary transport from a first-principles standpoint, we will need to consider that possibility in a future work, since those models will build off the bulk models, and so the work outlined in the present phase would be a necessary starting point anyway.

Transport of oxide anion in the iron-rich oxide phases is not likely to differ based on Tc content, hence, rate constants available in the literature should be sufficient for modeling reaction (3.1-d).

### Characterization of interfaces

Reactions (3.1-a) and (3.1-b) occur at the metal/oxide interface, and reactions (3.1-e)-(3.1-g) occur at the oxide/environment interface. Previously, models were initiated for the Tc/TcO<sub>2</sub> interface using density functional theory (Taylor, 2014). The next step is to model the Fe/FeO<sub>x</sub> interface and the interfaces between solid-solution and intermetallic phases with the spinel Fe<sub>2</sub>CrO<sub>4</sub>. Similar to the preceding section on point-defect structure, the interfaces will also possess an equilibrium structure. Using density functional theory and variable charge interatomic potentials (like ReaxFF or COMB; Jeon et al., 2011; Martinez et al., 2013), it is possible to find these equilibrium structures, and to consider how they will be perturbed by the presence of dissolved Tc. Subsequently, one can perturb these structures to examine transport processes, again, using transition state theory. In this way, the rate constants for reactions (3.1-a) and (3.1-b) can be predicted.

Reactions (3.1-e) and (3.1-g) are dissolution reactions, in which the Tc cation, having migrated through the oxide film, reacts with water to form the solubilized pertechnetate ion. This process can also be modeled using density functional theory, or by using suitable interatomic potentials, parameterized using density functional theory data. The models for Tc point-defects in iron oxide phases developed previously (Skomurski et al., 2010) will be generalized to surface states and applied to uncover the rate constants for reactions (3.1-e) and/or (3.1-g).

Reaction (3.1-f) is the incorporation of oxygen from the environment into the oxide film. As with reaction (3.1-d) we do not expect this rate constant to be heavily dependent upon the presence of Tc, so we plan to use literature data for this reaction rate for the hematite and spinel phases.

### Integration into a kinetic model

Once the rate constants are established, one of three predominant conditions will be revealed:

#### 1. Cation vacancy annihilation at the metal/oxide interface is rate-limiting

If it is found that the rate constant for reaction (3.1-a) or (3.1-b) is lower than the rate for diffusion across the oxide film (for reaction (3.1-c)) or dissolution (reaction (3.1-e) or (3.1-g)) then the loss of Tc from the candidate alloy waste form will be limited by the rate at which Tc enters the passive layer. This information could then be used to investigate alloy compositions or interface engineering strategies for further decreasing this rate constant, if further optimization of this value is required.

#### 2. Transport of Tc through the film is rate-limiting

In this case, equilibrium conditions will exist at the metal/film and film/environment interfaces, and the rate at which the Tc is released into the environment will be equal to the diffusion rate across the oxide film, given by the rate constant for reaction (3.1-c). We assume here that the rate of counter flow of the oxide anion in the film will not impact the rate of outward Tc migration, because other cations, such as Fe(II) and Fe(III) will predominantly be providing the necessary charge balance. Experimentally determined oxide thicknesses will be used to estimate the rate of Tc transport across the film, along with the rate constants for point-defect migration obtained from density functional theory. The rate will also depend on the concentration gradient, which we can estimate based on background Tc levels and the desired alloy composition.

### 3. Dissolution of Tc at the oxide/environment interface

In this condition, there will exist an equilibrium between the Tc concentrations in the alloy and the oxide film, and the limitation will come from the rate at which Tc can dissolve from the oxide film via reactions (3.1-e) or (3.1-g). The equilibrium concentration of Tc in the oxide film can be determined from Boltzmann distribution and the formation energies for Tc point-defects in the oxide film, as well as the chemical potential of Tc in the alloy itself.

#### 3.1.2 Density functional theory modeling of Tc incorporation and transport in intermetallic oxides

##### 3.1.2.1 Computational approach

First-principles total energy calculations were performed using density functional theory (DFT) as implemented in the *Vienna ab initio simulation package* (VASP; Kresse and Furthmüller 1996). The exchange–correlation energy was calculated using the generalized gradient approximation (GGA) with the parameterization of Perdew, Burke, and Ernzerhof (PBE; Perdew et al., 1996). The interaction between valence electrons and ionic cores was described by the projector augmented wave (PAW) method (Blochl 1994). The Tc (4p,5s,4d) electrons were treated explicitly as valence electrons in the Kohn–Sham (KS) equation and the remaining core electrons, together with the nuclei, were represented by PAW pseudopotentials. The plane-wave cutoff energy for the electronic wavefunctions was set to a value of 400 eV. Periodic unit cells were used to calculate the total energy of iron oxides in which Tc atoms are incorporated. Electronic relaxation was performed with the conjugate gradient method accelerated using the Methfessel–Paxton Fermi-level smearing (Methfessel and Paxton, 1989) with a Gaussian width of 0.2 eV. Ionic relaxation was carried out using the Hellmann–Feynman forces acting on atoms. The Brillouin zone was sampled using the Monkhorst–Pack special k-point scheme (Monkhorst and Pack, 1976) for structural optimization and total energy calculations.

##### 3.1.2.2 Previous results of binary Tc oxides

In line with the efforts to develop metal alloy waste-forms that can immobilize Tc, the present research activities are focused on screening possible oxide candidates that can incorporate Tc and that can also provide insights into the surface oxide properties that are crucial for gaining fundamental understandings of the corrosion process of metal surfaces. A first attempt was made to understand possible polymorphism in the Tc-O binary system. So far, two oxides of technetium have been synthesized and characterized experimentally: (i) black-colored technetium dioxide ( $\text{TcO}_2$ ; Schwochau, 2000) and (ii) pale-yellow heptoxide ( $\text{Tc}_2\text{O}_7$ ; Muller et al., 1964; Krebs, 1969). Single crystal of  $\text{Tc}_2\text{O}_7$  was synthesized by combustion of  $^{99}\text{Tc}$  in a stream of oxygen at 400 °C (Muller et al., 1964), which crystallizes in the orthorhombic space group (Pbca; Krebs, 1969). According to Muller et al. (1964),  $\text{TcO}_2$  is stabilized in the  $\text{MoO}_2$  structure type, which is a distorted rutile structure. A systematic study was carried out to investigate the relative structural stability of possible Tc binary oxides including TcO,  $\text{TcO}_2$ ,  $\text{TcO}_3$ , and  $\text{Tc}_2\text{O}_7$  using DFT and the results were compared with experimental data available in the literature. Figure 3.1-2 depicts the optimized crystalline structures of Tc oxides. In the case of TcO, which has not been synthesized yet, the hypothetical B1 structure - since it is the most commonly found in transition metal-monoxides (Schweika et al., 1995) - was selected. The calculated lattice constants of  $\text{TcO}_2$  are  $a=5.77$ ,  $b=4.86$ , and  $c=5.65$  Å (see Table 3.1-1), in excellent agreement with experimental values (Muller et al., 1964). The estimated formation energy of  $\text{TcO}_2$  in a monoclinic phase is 4.25 eV per formula unit (f.u.), which is close to the experimental value of 4.75 eV/f.u. (Lemire and Jobe, 1996).

Our DFT calculations predict that the bulk modulus of  $\text{TcO}_2$  is 203 GPa, revealing a hardness comparable to AlN (Aluminum Nitride hardness 1100 Kg/mm<sup>2</sup>; Sherwin and Drummond, 1991). Such high hardness is due to the three-dimensional edge and corner-sharing network of  $\text{TcO}_6$  octahedra. In  $\text{TcO}_2$  each edge-shared oxygen is also corner-shared with an adjacent infinite chain of edge-sharing octahedral.  $\text{Tc}_2\text{O}_7$  is one of the few known transition metal oxides having a molecular structure in the solid state (Krebs,

1969). Each  $\text{Tc}_2\text{O}_7$  molecule consists of two  $\text{TcO}$  tetrahedra sharing one oxygen atom. The van der Waals forces between  $\text{Tc}_2\text{O}_7$  molecules play a major role in holding them together in an orthorhombic lattice. The calculated lattice constants are highly overestimated compared with experimental values, pointing out the fact that DFT may handle the weak van der Waals interactions poorly, resulting in the predicted bulk modulus of about 3 GPa. A hypothetical  $\text{TcO}_3$  structure, in which has the  $\text{MoO}_3$  structure as shown in Figure 3.1-2, is less energetically stable than  $\text{TcO}_2$ . According to the estimated formation of binary Tc oxides,  $\text{TcO}_2$  is the most energetically favorable form, followed by  $\text{Tc}_2\text{O}_7$ .

**Table 3.1-1. Structural properties of Tc,  $\text{TcO}_2$  and  $\text{Tc}_2\text{O}_7$ . Units are in Å and eV per formula unit (eV/f.u) for the lattice constants and formation energy, respectively. Experimental values are from references: a: Kittel, 1996, b: Muller et al., 1964; Lemire and Jobe, 1996, and c: Muller et al., 1964; Krebs, 1969.**

|                            | Tc (HCP)         |                    | $\text{TcO}_2$ (Monoclinic) |                            | $\text{Tc}_2\text{O}_7$ (Orthorhombic) |                             |
|----------------------------|------------------|--------------------|-----------------------------|----------------------------|--|-----------------------------|
|                            | DFT              | Expt. <sup>a</sup> | DFT                         | Expt. <sup>b</sup>         | DFT                                    | Expt. <sup>c</sup>          |
| Lattice constant (Å)       | a=2.75<br>c=4.40 | a=2.74<br>c=4.40   | a=5.77<br>b=4.86<br>c=5.65  | a=5.53<br>b=4.79<br>c=5.53 | a=15.09<br>b=8.19<br>c=6.19            | a=13.76<br>b=7.44<br>c=5.62 |
| Formation energy (eV/f.u.) | 6.97             | 6.85               | 4.25                        | 4.75                       | 10.88                                  | 11.53                       |

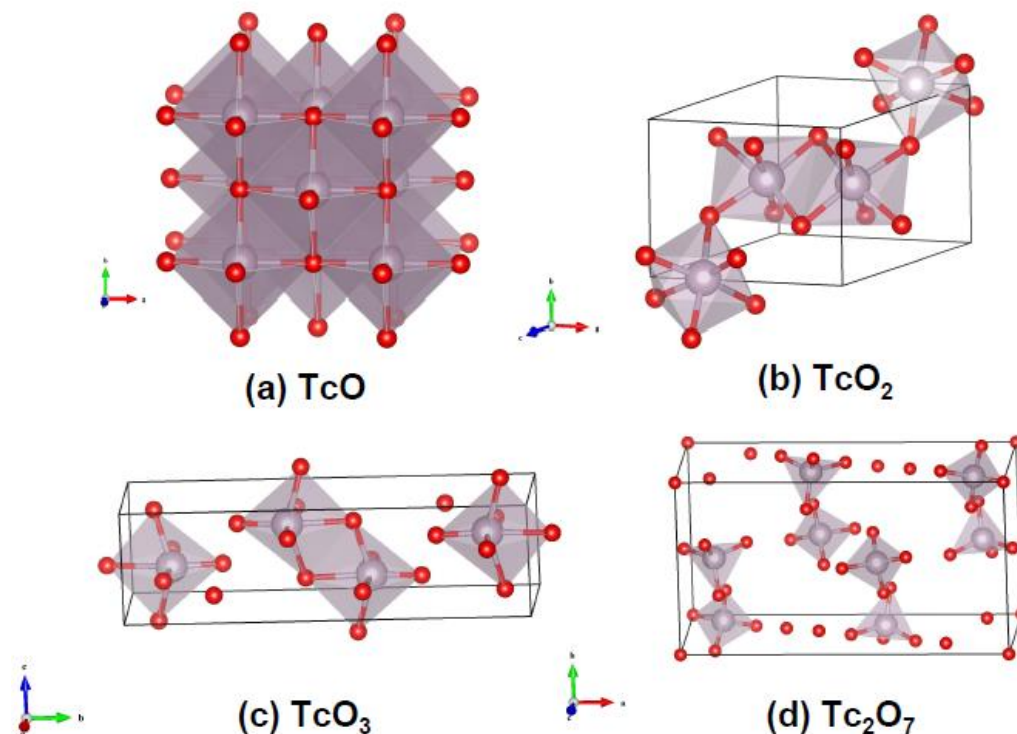


**Figure 3.1-2. Crystalline structures of binary Tc oxides: (a)  $\text{TcO}$ , (b)  $\text{TcO}_2$ , (c)  $\text{TcO}_3$ , and (d)  $\text{Tc}_2\text{O}_7$ . The grey and red spheres represent Tc and O atoms, respectively.**

### 3.1.2.3 Dilute Tc incorporation and diffusion in FeO, Fe<sub>2</sub>O<sub>3</sub>, and Fe<sub>3</sub>O<sub>4</sub>

As stated in previous sections, how Tc is incorporated into iron oxides is one of the most important processes in the Tc release model. In this section, spin-polarized DFT calculations were firstly attempted to understand the energetics of Tc incorporation in the vacancy defect sites for a range of iron oxides, FeO,  $\alpha$ -Fe<sub>2</sub>O<sub>3</sub>, and Fe<sub>3</sub>O<sub>4</sub>.

Magnetism is known to play an active role in the electronic structures of these iron oxides. FeO, or wüstite, is dominant in the early stages of iron oxidation or in the formation of ultrathin films (Jeon et al., 2011). FeO has rock salt (NaCl) B1 type crystal structure. Below Néel temperature, this oxide has an antiferromagnetic ordering, denoted as AFM II (Roth, 1958). In this ordering, the spin moments of Fe atoms in alternating (111) planes are anti-parallel in spin directions (Schrön et al., 2012; Forti et al., 2012). Figure 3.1-3a describes such magnetic spin ordering in FeO. For DFT supercell calculations that require periodic boundaries, a rhombohedral supercell is employed (see also Figure 3.1-3a).

Hematite ( $\alpha$ -Fe<sub>2</sub>O<sub>3</sub>) is the most abundant phase among all of the iron oxides. Hematite has a hexagonal corundum-type ( $\alpha$ -Al<sub>2</sub>O<sub>3</sub>) structure, with space group R $\bar{3}c$ . The complete hexagonal unit cell of hematite is used in the DFT calculations. Below Néel temperature, this oxide also has an antiferromagnetic ordering. As noted previously (Rollmann et al., 2004), there are two types of Fe-Fe pairs in this oxide, with one type (denoted as type A) shorter, and another type (denoted as type B) larger in distance. The minimum energy state corresponds to AF + + - - state, that atoms belonging to type A pairs have equal magnetic moments while atoms belonging to type B pairs have opposite magnetic moments. This result agrees with recent other DFT calculations (Lee and Han, 2013). Figure 3.1-3b describes the magnetic spin ordering and the crystal structure in the hexagonal supercell.

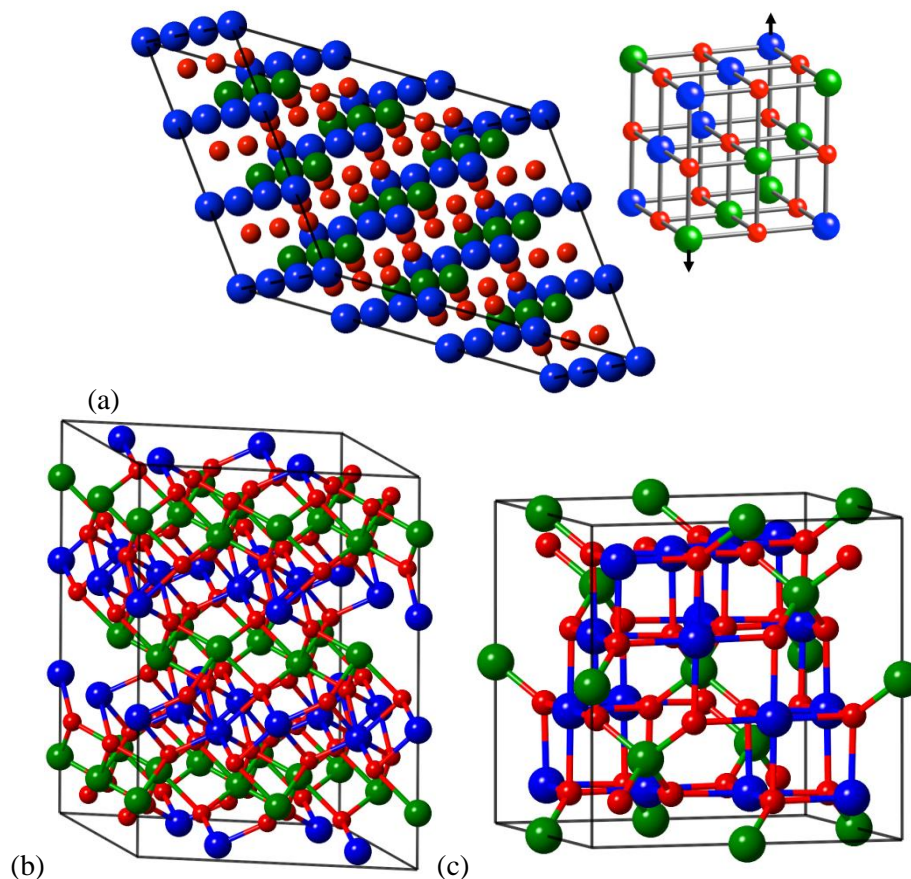


Figure 3.1-3. Supercell structures used in defects calculations (a) FeO, (b)  $\alpha$ -Fe<sub>2</sub>O<sub>3</sub>, (c) Fe<sub>3</sub>O<sub>4</sub>. Small red balls are oxygen atoms, large blue and green balls are Fe atoms with spin up and spin down, respectively.

Finally,  $\text{Fe}_3\text{O}_4$ , or magnetite, is the basic oxide form during early oxidation stage of stainless steel (Tempest and Wild 1985). It has a cubic inverse spinel structure, with space group  $\text{Fd}\bar{3}\text{m}$ . In Figure 3.1-3c, such structure is shown. In the cubic unit cell, the tetrahedral sites are occupied by  $\text{Fe}^{3+}$  ions, while the octahedral sites are occupied by equal number of  $\text{Fe}^{3+}$  and  $\text{Fe}^{2+}$  ions. The Fe ions belonging to the tetrahedral sites and octahedral sites have opposite magnetic moments, so magnetite is a ferrimagnetic oxide.

Under dilute limit, it is reasonable to assume that the thermally generated or natural grown crystal oxides have enough vacancies for Tc accommodation. The DFT results for a simple Fe vacancy in three oxides, as well as the Tc incorporation energy at the available Fe vacancy sites in these oxides are summarized in Table 3.1-2. DFT results show that it will cost 3.1 eV for Tc to be incorporated at Fe vacancy in FeO. While in  $\alpha\text{-Fe}_2\text{O}_3$ , the Tc incorporation will release 3.1 eV in energy, making this process energetically preferred. In  $\text{Fe}_3\text{O}_4$ , while it is energetically preferred for Tc to be incorporated in octahedral Fe vacancy site, this type of vacancy site is less possible to exist due to the extremely high energetics (relative to the tetrahedral vacancy site). Further study to include the strong-electron correlation effect (see Section 3.1.2.5) is to be done to validate our findings.

**Table 3.1-2. Spin-polarized PAW-PBE DFT calculated relative energy for different Fe vacancies, and Tc incorporation energy at available Fe vacancy sites in FeO,  $\alpha\text{-Fe}_2\text{O}_3$ , and  $\text{Fe}_3\text{O}_4$ .**

|   | FeO  | $\alpha\text{-Fe}_2\text{O}_3$ | $\text{Fe}_3\text{O}_4$ |             |
|---|------|--------------------------------|-------------------------|-------------|
|   |      |                                | Octahedral              | Tetrahedral |
| Relative energy for different Fe vacancies (eV) | N/A  | N/A                            | 0.0                     | -37.15      |
| Tc incorporation energy (eV)                    | 3.10 | -3.11                          | -39.40                  | 50.95       |

Next, spin-polarized DFT calculations were carried out to obtain the migration energy barriers during diffusion, assuming that Tc is already incorporated in  $\alpha\text{-Fe}_2\text{O}_3$ . The nudged elastic band method is used in DFT calculations (Henkelman et al., 2000). Figure 3.1-4 illustrates the most likely diffusion pathway in  $\alpha\text{-Fe}_2\text{O}_3$ , i.e., the type A pairs channel. For the first time, the migration energy barrier calculated by DFT for Tc migration via vacancy mechanism is 1.9 eV. For pure Fe migration, the migration energy barrier is calculated as 1.1 eV, which is substantially lower than for Tc migration. The DFT results suggest that Tc diffusion in hematite oxide is much slower than the anion (O) or cation (Fe) diffusion.

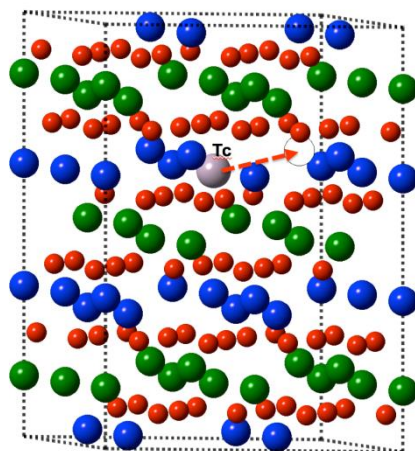


**Figure 3.1-4. Supercell structure in DFT calculation of Tc migration to a nearby Fe vacancy site in  $\alpha\text{-Fe}_2\text{O}_3$ . Small red balls are oxygen atoms, and large blue and green balls are Fe atoms with spin up and spin down, respectively.**

### 3.1.2.4 Waste form stability of different spinel phases

The long-term corrosion characteristics depend upon the phase-stability of the material, the nature of the passive oxide films that form on their surface, and the reactivity of the metal surfaces and oxide surfaces toward their local environment (Kim et al., 2014). Due to the superior physicochemical properties, oxide spinel systems have been used in electrical, optical, mechanical, and magnetic applications (Glasso, 1970). Synthesis of  $\text{TcCo}_2\text{O}_4$  was done successfully by Thorogood et al. (2011). This demonstrates the possibility of using spinels as surrogate hosts for Tc incorporation. In this study we investigate the possibility of incorporating Tc into existing iron oxide spinel (magnetite,  $\text{Fe}_3\text{O}_4$ ), calcium ferrite ( $\text{CaFe}_2\text{O}_4$ ), and rare-earth iron oxide ( $\text{YFe}_2\text{O}_4$ ) lattices. These structures are selected here for the following reasons: they are stable in both (i) the same stoichiometry  $\text{Tc:Fe:O}=1:2:4$ , and (ii) all three distinct lattice types (see Figure 3.1-5a-c). In addition, the high-pressure spinel structure is isostructural with the  $\text{CaFe}_2\text{O}_4$  phase or vice versa (Cornell and Schwertmann, 2003).  $\text{CaFe}_2\text{O}_4$  crystallizes in the orthorhombic  $Cmcm$  space group (see Figure 3.1-5b). The crystal structure of  $\text{YFe}_2\text{O}_4$  is a rhombohedral layered structure with space group  $R-3m$  (see Figure 3.1-5c). It is characterized as an alternate stacking of the hexagonal  $\text{Fe}_2\text{O}_3$  layer and the hexagonal YO layer along c-axis.

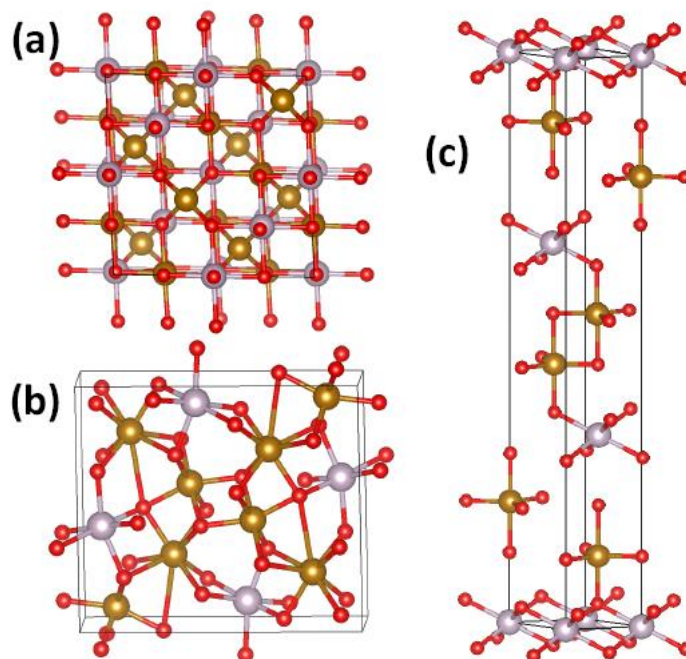


Figure 3.1-5. Crystalline structures of Tc-Fe-O in (a) cubic ( $Fd-3m$ , 227), (b) orthorhombic ( $Cmcm$ , 63), and (c) rhombohedral ( $R-3m$ , 166) lattices. The gold, grey, and red spheres represent Fe, Tc, and O atoms, respectively.

The DFT results are plotted in Figure 3.1-6, which predicts that magnetite is the most stable form to host Tc atoms up to about 33%, forming a  $\text{TcFe}_2\text{O}_4$  spinel. Above 33% of Tc inclusion a  $\text{TcFe}_2\text{O}_4$  spinel becomes energetically less stable than the ones in  $\text{CaFe}_2\text{O}_4$  and  $\text{YFe}_2\text{O}_4$  lattices. For these high Tc concentrations, the rhombohedral phase is becoming most stable form.

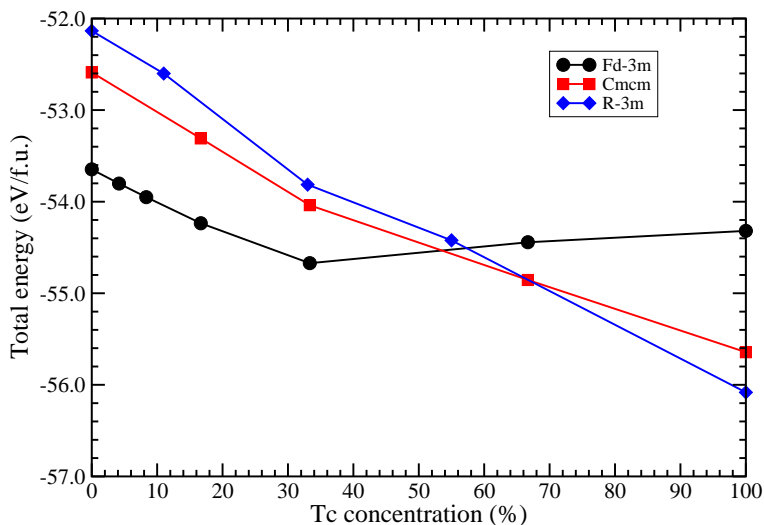


Figure 3.1-6. Total energies of TcFe<sub>2</sub>O<sub>4</sub> in cubic (Fd-3m), orthorhombic (Cmcm), and rhombohedral phases with respect to Tc concentration. The unit of the energy is eV per formula unit (eV/f.u.).

Table 3.1-3. Lattice constant and bulk modulus of magnetite. Units are in Å and GPa for the lattice constant and bulk modulus, respectively.

| U <sub>eff</sub> (eV) | 0    | 2    | 4    | Expt.<br>(Klotz et al., 2006) |
|-----------------------|------|------|------|-------------------------------|
| Lattice constant (Å)  | 8.37 | 8.43 | 8.45 | 8.39                          |
| Bulk modulus (GPa)    | 173  | 176  | 178  | 180                           |

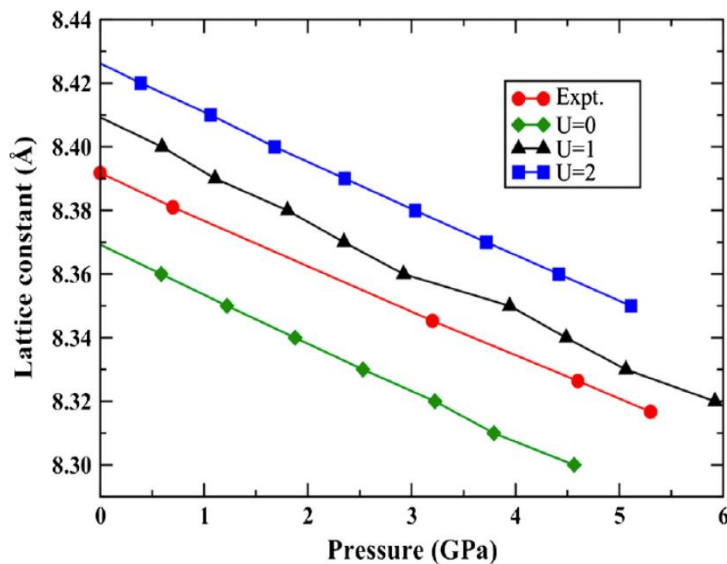


Figure 3.1-7. Compressibility of magnetite. The experimental data were taken from Klotz et al. (2006)

### 3.1.2.5 *Benchmark of strong-electron correlation effect*

The benchmark calculation was carried out for magnetite ( $\text{Fe}_3\text{O}_4$ ) by varying the effective strong-electron correction parameter,  $U_{\text{eff}}$ , to correct for the lack of electron localization within the framework of standard DFT. The results are compared to experimental data, as summarized in Table 3.1-3. The estimated lattice constant is underestimated when  $U_{\text{eff}} = 0$  eV, whereas it is slightly overestimated when  $U_{\text{eff}} = 2$  and 4 eV, compared to the experimental value of 8.39 Å. The volume compression data also show that the calculated volume is consistently overestimated when the  $U_{\text{eff}}$  value is greater than or equal to 1, as shown in Figure 3.1-7. This finding indicates that the LDA+U correction may be necessary to predict the structural properties of Tc incorporated iron oxides more accurately.

### 3.1.3 *Atomistic scale modeling of Tc corrosion*

#### 3.1.3.1 *kMC modeling of Tc alloy corrosion*

The modified embedded atom method has been applied to enable off-lattice kinetic Monte Carlo simulations of the active dissolution of binary alloys (Taylor and Liu, 2013). Application of this method to the Tc-Fe, Tc-Mo, and Tc-Ni binary systems has provided some fundamental science inputs to the development of waste forms for fission products, which would otherwise be difficult to determine from a purely experimental standpoint. The kinetic Monte Carlo method provides a means for evaluating the types and relative severity of corrosion that such waste forms may experience as a function of composition, crystallography and surface orientation. Modeling of the alloy surface corrosion rate is particularly important for localized corrosion behaviors (the rupture of oxide films by localized dissolution, mechanical damage, or presence of deleterious chemistries).

In Figure 3.1-8, the corrosion morphologies of the above candidate alloy waste forms containing 1, 5 and 10 percent Tc are shown. While the corrosion morphology for Tc-Fe and Tc-Mo alloys are similar, the crystallographic pitting for Tc-Ni is sharper than Tc-Fe or Tc-Mo. Such morphology difference may suggest that the local ordering within alloy can play a significant role in the stability of the waste form.

In Figure 3.1-9, the relative corrosion rates versus Tc composition for Tc-Fe, Tc-Mo, and Tc-Ni are shown. The corrosion rate is determined from the inverse of the time required to complete the simulation, multiplied by the number of atoms dissolved. A corrosion potential of 0 V on the hydrogen electrode scale was assumed for the simulations, at room temperature. As shown in Figure 3.1-9, regarding bcc Fe and Mo solid solutions containing Tc, the Tc addition up to 10% decreases the corrosion rate. However, such trend is reversed for fcc Ni solid solutions containing Tc up to 10%. This is presumably due to the large lattice mismatch of Tc and large dilute heat of solution (1 eV/atom) in fcc Ni.

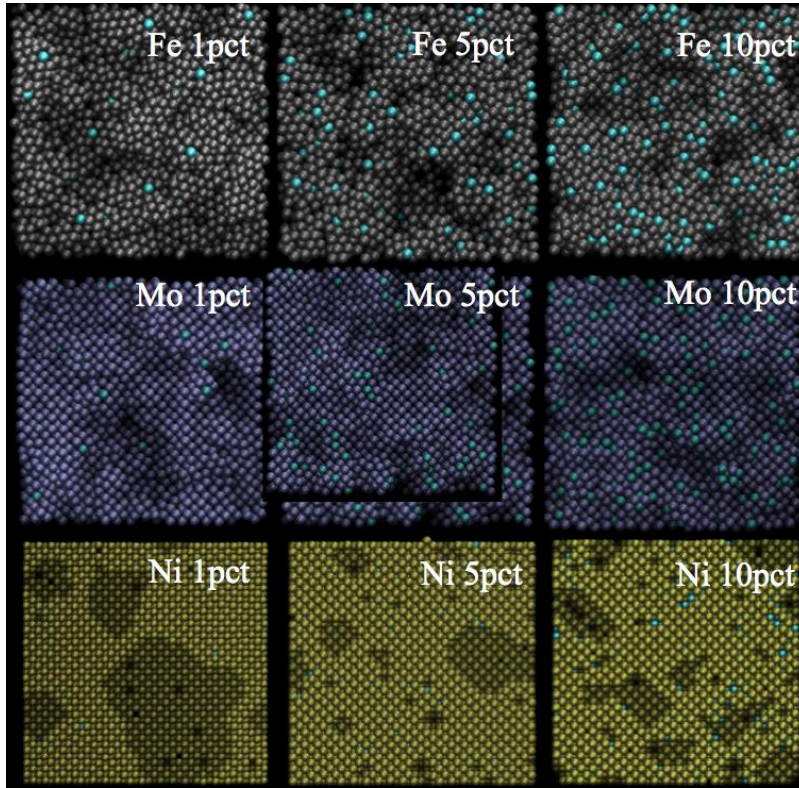


Figure 3.1-8. Corrosion morphologies obtained as outputs after the simulation of 1000 dissolution events for candidate alloy waste forms

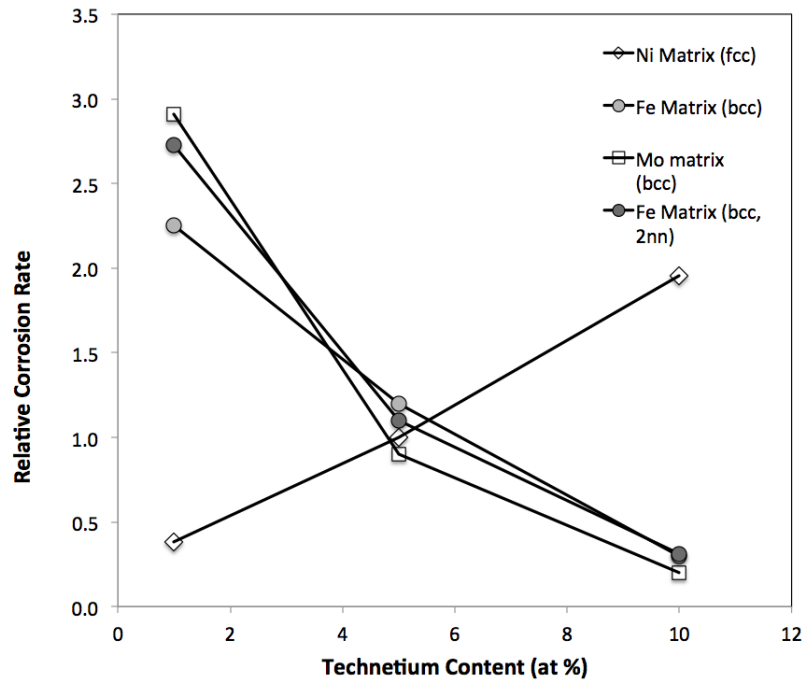


Figure 3.1-9. Average corrosion rate versus Tc composition for Tc-Fe, Tc-Mo, and Tc-Ni.

### 3.1.3.2 Development of TcO<sub>2</sub> oxide empirical potential for molecular dynamics simulation

Development of reactive force fields for molecular dynamics (MD) simulations of Tc transport between metal alloys and associated oxides are desired. The main advantage of MD simulations is the much larger length scale in simulations, compared to that in DFT, to treat microstructural effects such as interface misfit, grain-boundaries, etc.

As a first step toward optimization of the empirical potential parameterization, the Buckingham pair potential scheme is chosen. Buckingham type potential have been used widely for modeling a range of oxides including UO<sub>2</sub>. The potential consists of the sum of the attraction and repulsion energies as

$$E = Ae^{-r/\rho} - \frac{C}{r^6} \quad (3.1-1)$$

where A,  $\rho$ , and C are parameters. The optimized Buckingham potential for Tc-O interaction is fitted to the DFT calculated lattice constants and bulk modulus of TcO<sub>2</sub>. The potential has a fixed charge model, with the charge of Tc set to +4 and O to -2 in the model. The calculated lattice constants of TcO<sub>2</sub> are a=7.11, b=5.01, and c=6.11 Å, compared to DFT results, a=5.77, b=4.86, and c=5.65 Å. The calculated bulk modulus of TcO<sub>2</sub> is 218 GPa, compared to DFT result of 203 GPa. The complex bonding of TcO<sub>2</sub> is modestly captured by the Buckingham potential. More complicated forms such as variable charge interatomic potentials (like ReaxFF or COMB; Jeon et al., 2011; Martinez et al., 2013) are expected to generate better empirical potential models. Currently, we are actively testing the Fe-O potential model in ReaxFF to build more experience.

### 3.1.4 Electrochemical Corrosion Studies for Modeling Metallic Waste Form Release Rates

Metal waste forms are being studied as possible disposal forms for technetium and other fission products from advanced nuclear fuel cycle options. In recent years, a variety of studies have been performed on various technetium alloy waste forms based on alloying technetium with zircaloy and / or stainless steel components. Alloying has been successful in producing lower-melting materials, however, the alloy products are composed of multiple phases having complex microstructures. Because the technetium release from these alloys is dominated by the least corrosion-resistant phase, understanding the corrosion response of these alloys involves understand the interplay of the metallurgy and corrosion behavior of the component phases. Corrosion studies of technetium metal are quite limited. As an initial step in assessing the viability of waste forms, technetium corrosion behavior was assessed.

**Experimental.** Tc metal was produced by thermal decomposition of NH<sub>4</sub>TcO<sub>4</sub> to TcO<sub>2</sub> at 450 °C for 1 hr under a slow flow of Ar. The TcO<sub>2</sub> was converted to Tc metal in Ar - 5 % H<sub>2</sub> using a two-step furnace cycle (700 °C for 24 hours followed by 900 °C for 4 hours).

Specimens were mounted in epoxy and polished to 500 grit finish. The polished samples were ultrasonically cleaned in ethanol for five minutes. Crevice corrosion between the metal and the epoxy mount was not apparent following testing. The exposed metal surface area varied between 0.02 and 0.2 cm<sup>2</sup> depending on the individual sample.

Solutions were composed of ambiently-aerated pH 3.2 H<sub>2</sub>SO<sub>4</sub>. Solutions were room temperature - self-heating from radioactive decay was considered negligible. A commercially-available, computer-controlled potentiostat was used to perform the electrochemical measurements. The electrochemical cell was a 100-mL, five-neck flask incorporating a Ag/AgCl reference electrode and a platinized-niobium mesh counter electrode. With the exception of in-situ abrasion tests, working electrodes were immersed in solution for four hours and the open circuit potential monitored. Potentiodynamic polarization tests used a scan rate of 0.1 mV/s. Electrochemical impedance spectroscopy (EIS) was performed using a 10-mV rms AC voltage signal, applied at frequencies between 100 kHz and 10 mHz using potentiostatic control. Impedance data fitting was performed using complex nonlinear least squares circuit fitting software. Most

tests were replicated to assess the reproducibility of the results, with as many as eight replicate tests performed.

**Results and discussion.** Open circuit potential measurements are shown in Figure 3.1-10. Data are superimposed on the potential – pH diagram for Tc. The red and black lines represent two different published values for the  $\text{TcO}_2 / \text{TcO}_4^-$  transition. The open circuit potential appears to fall near or above the transition. The  $\text{TcO}_4^-$  region is a region of corrosion (as opposed to passivity), therefore pure Tc would not be predicted to spontaneously passivate upon exposure to pH 3.2  $\text{H}_2\text{SO}_4$ .

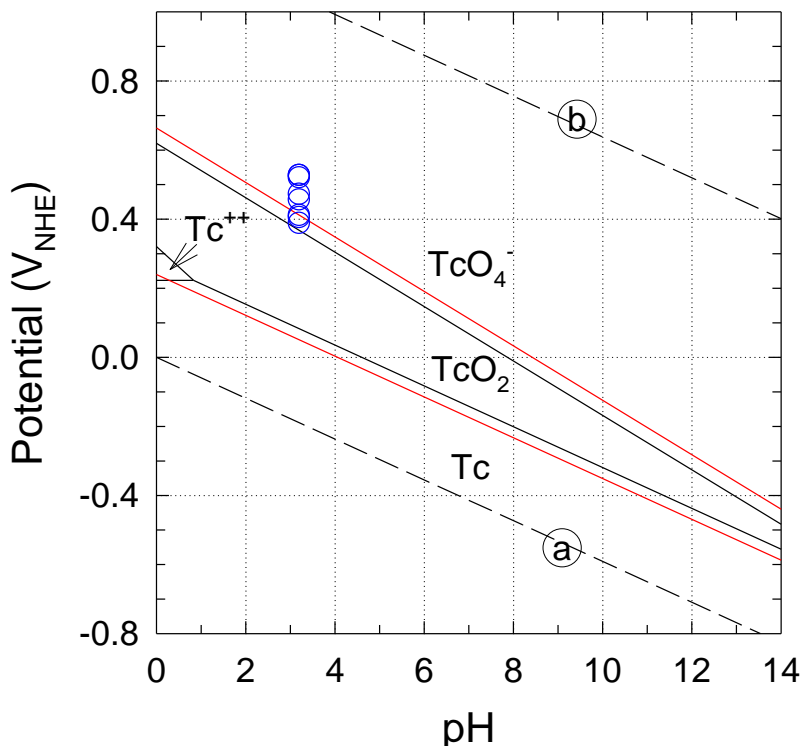


Figure 3.1-10. Open circuit potential data following 4 hour exposure to pH 3.2  $\text{H}_2\text{SO}_4$ . Black line – from Cartledge and Smith (1955). Red line – from Cobble et al. (1953). Dashed line marked (a) represents the cathodic  $\text{H}_2$  formation half reaction and dashed line marked (b) represents cathodic  $\text{H}_2\text{O}$  formation half reaction.

Anodic polarization measurements (Figure 3.1-11, top) confirm that Tc does not passivate upon exposure to pH 3.2  $\text{H}_2\text{SO}_4$ . A black film is observed following anodic polarization. The nature of the film will be investigated in the future, but is surmised to be  $\text{Tc}(\text{OH})_4$  based on the literature.

Although not observed on the forward scan, the reverse scan (Figure 3.1-11, bottom) indicates a transition (bend in the curve) that may be the  $\text{TcO}_2 / \text{TcO}_4^-$  transition. This transition appears at a potential more noble than that reported in the literature (see black and red lines in Figure 3.1-10). The discrepancy may be attributable to the reported sluggishness of the  $\text{TcO}_2 / \text{TcO}_4^-$  reaction (Cartledge and Smith, 1955). The reported data in the literature were acquired using precise methodologies and over long periods of time. The  $\text{Tc} / \text{TcO}_2$  and  $\text{TcO}_2 / \text{TcO}_4^-$  transitions will be further investigated.

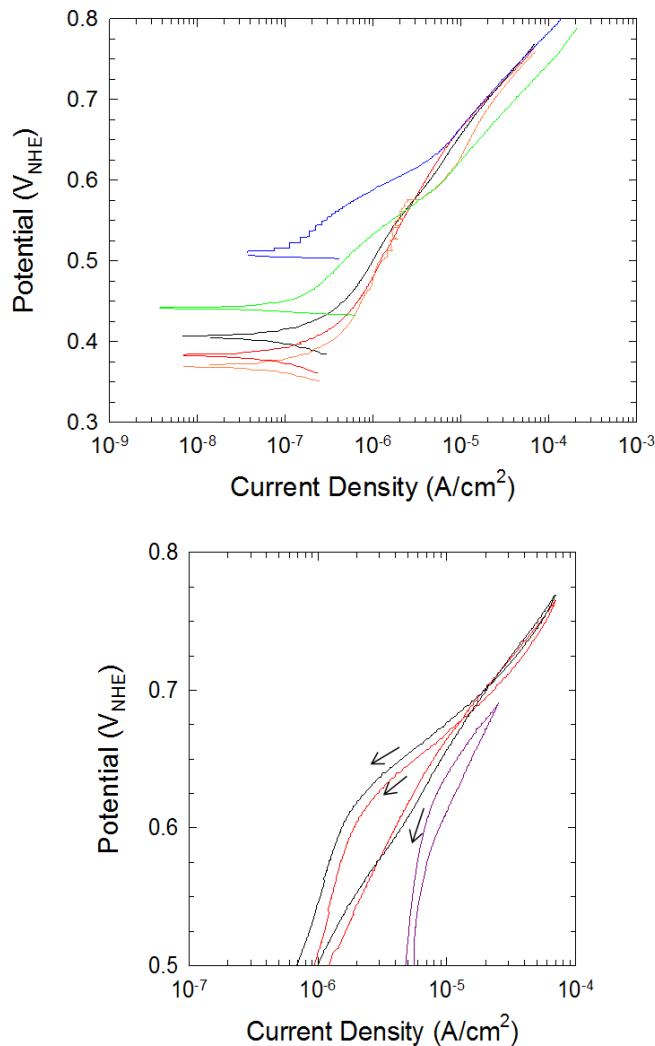


Figure 3.1-11. Top - Anodic polarization curves for Tc exposed to pH 3.2  $\text{H}_2\text{SO}_4$  solution. Bottom - selected return scans.

A test involving unconventional sample preparation was employed to determine whether the air-formed oxide on the surface of Tc was interfering with the formation of a passive film. The unconventional test involved polarizing a sample to  $-0.3V_{\text{NHE}}$  and abrading the surface *in-situ* under potential control. At a potential of  $-0.3V_{\text{NHE}}$ , Tc metal is stable and Tc oxidation is precluded. Therefore, any air-formed oxide was removed and no film would be present. Following abrasion, the sample was then polarized anodically to observe the sample behavior. Figure 3.1-12 shows the conventionally-run anodic polarization curves shown in Figure 3.1-11, along with a conventionally-run cathodic polarization curve and the unconventionally prepared sample (heavy dashed line). It is seen that the behavior of the unconventionally-run sample is quite similar to those that were conventionally run. No obvious behavior differences are seen either on the cathodic branch above  $0.1V_{\text{NHE}}$ , where Tc oxidation begins or on the anodic branch. In particular no evidence of passivity is present. One difference between the conventional and unconventional runs is a slightly higher current density in the unconventional run. This would be expected given the removal of the film which provides a mass transport barrier (as evidenced by the mass transport (i.e., non-Tafel) control upon anodic polarization).

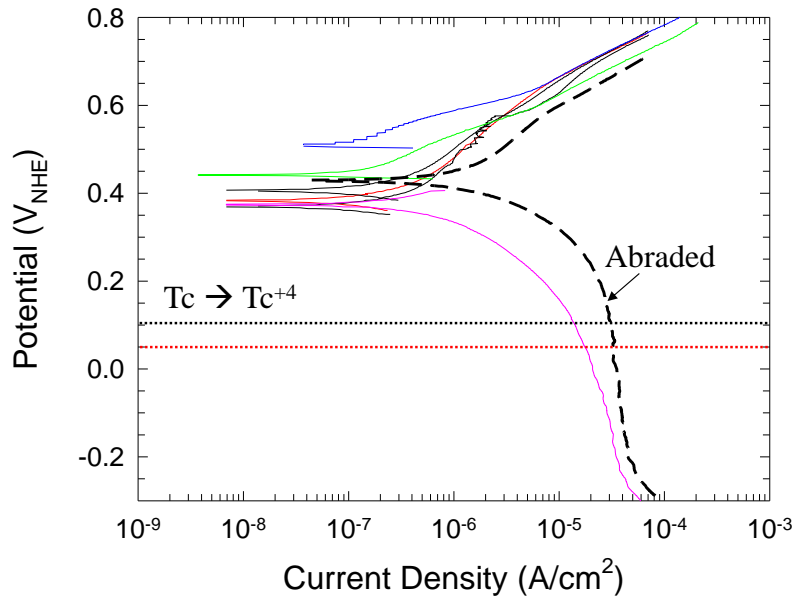


Figure 3.1-12. Anodic and cathodic potentiodynamic polarization data. Solid lines are tests using conventionally prepared samples. The heavy dashed line is a sample abraded *in-situ* at  $-0.3V_{NHE}$ .

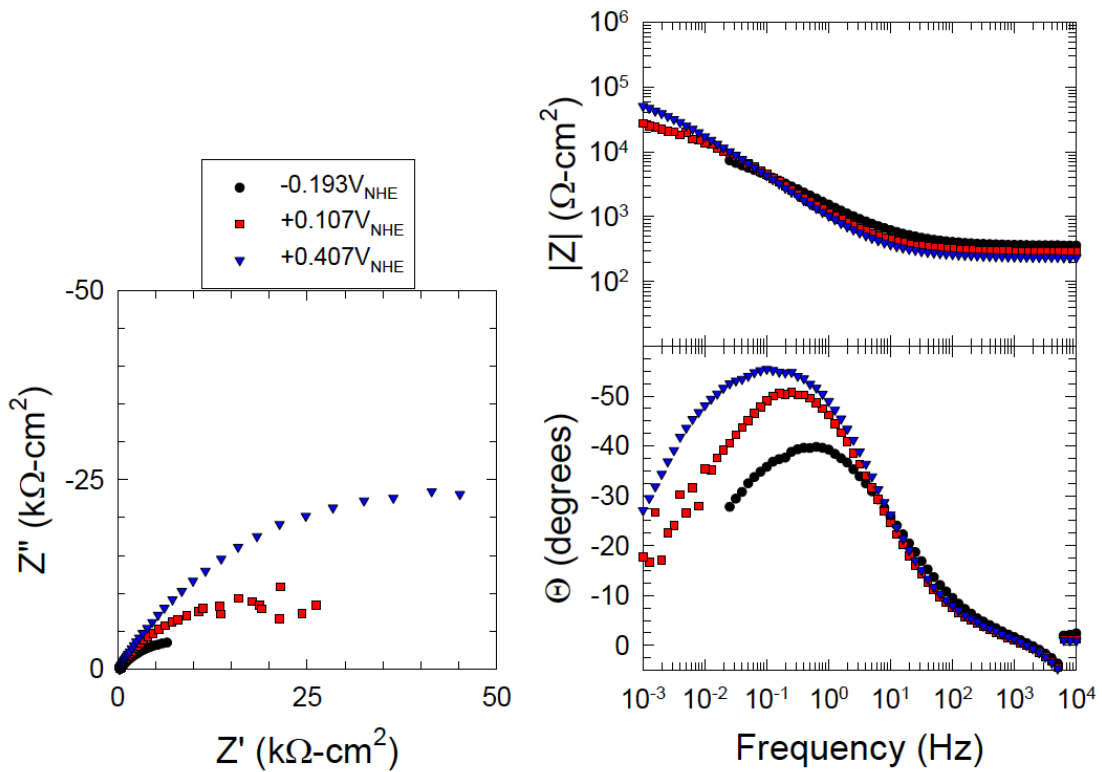


Figure 3.1-13. Electrochemical impedance data (Nyquist (left), Bode magnitude (right top) and Bode phase angle (right bottom)) at potentials that correlate to  $Tc$ ,  $Tc^{+4}$  and  $Tc^{+7}$  regions of stability. Sample was abraded at  $-0.5V_{NHE}$ .

Figure 3.1-13 includes electrochemical impedance spectra from a sample abraded in-situ at  $-0.5 V_{\text{NHE}}$ . In this set of experiments an EIS spectrum was acquired every 100 mV up to  $0.5 V_{\text{NHE}}$ . Samples were ramped 100 mV, followed by a 4-hour potentiostatic hold and then acquisition of an EIS spectrum. Three selected spectra are shown in Figure 3.1-13, one each from the Tc,  $\text{Tc}^{+4}$  and  $\text{Tc}^{+7}$  regions. In all cases only one time constant is apparent. Although not definitive, this is consistent with the absence of a passive film.

Figure 3.1-14 shows the results of fitting the EIS spectra acquired from the test shown in Figure 3.1-13. The model used to fit the data was the circuit shown in the top left of Figure 3.1-5. A constant phase element is used to account for the nonidealities of the surface.  $R_s$  is the solution resistance,  $R_p$  is the polarization resistance of the system and  $C_{\text{dl}}$  is the double-layer capacitance (or film capacitance) and  $\Phi$  is the exponent which determines the phase angle of the constant phase element. The vertical dashed lines in Figure 3.1-14 are the published Tc /  $\text{TcO}_2$  and  $\text{TcO}_2 / \text{TcO}_4^-$  transitions along with the observed open circuit potential.

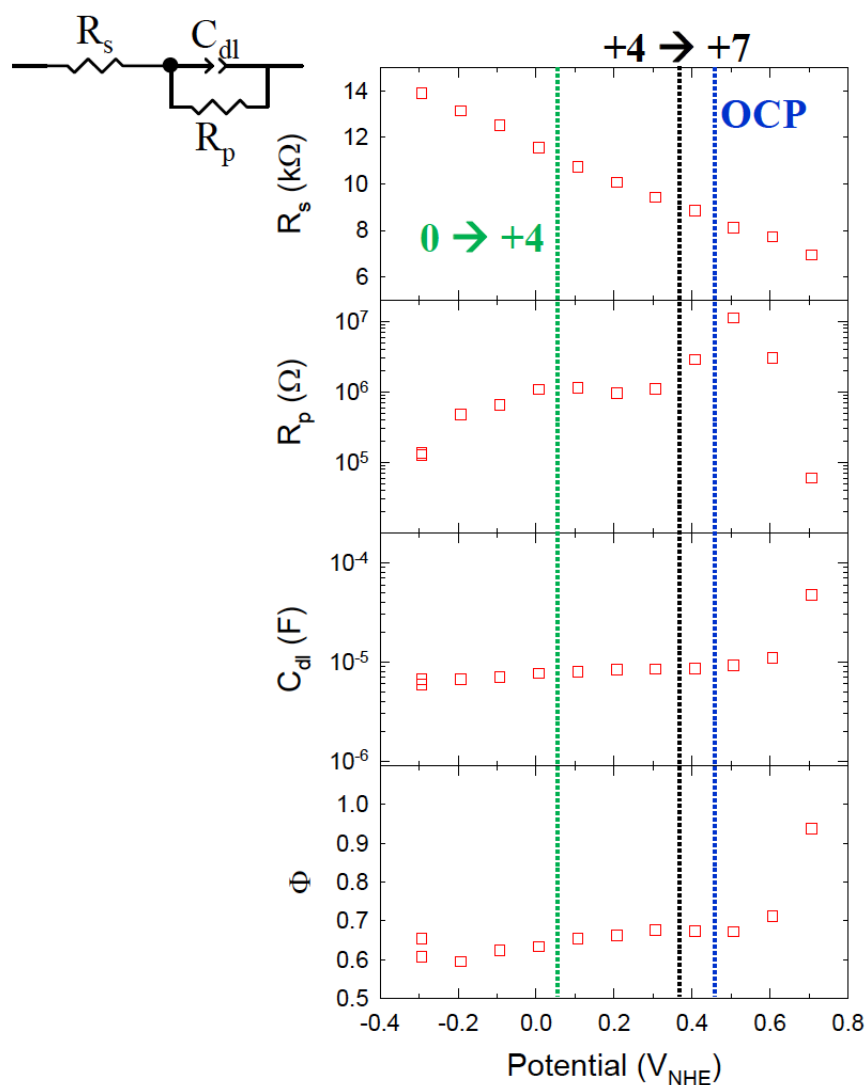


Figure 3.1-14. Results from fitting of EIS data using the circuit model shown at the top left. OCP (open circuit potential) line is also labeled.

It is seen from the fitted data that there are no obvious breaks in the fitted parameters when crossing the published transition potentials. This suggests that film formation does not appear to dominate the observed cathodic reaction in the vicinity of the Tc / TcO<sub>2</sub> transition potential because there is no change in R<sub>p</sub>. This also suggests that there is no significant change in the film properties when crossing the TcO<sub>2</sub> / TcO<sub>4</sub><sup>-</sup> transition potential. All of this information supports the observation that no dramatic changes in electrochemical behavior (including passive film formation) occur in the Tc<sup>+4</sup> or Tc<sup>+7</sup> regions.

Our tests results do not correspond to expected passivation behavior based on the information within the potential – pH diagram for the Tc-H<sub>2</sub>O system. Neither the indicated electrochemical transitions nor the passivity were observed. The dissolve sulfate in the test solutions may account for differences.

### 3.1.5 Summary and Discussion

To summarize, the metallic waste form degradation program utilizes a first-principles approach to enable predictive corrosion modeling of alloy waste forms, through validation with high-resolution characterizations.

- A multistep corrosion mechanism that is responsible for the release of Tc from any candidate alloy waste form is described. Also outlined is the first-principles approach that will be used to build a predictive model for candidate alloy waste form corrosion, useful for both alloy design and making long-term predictions.
- DFT modeling of Tc incorporation and transport in intermetallic oxides has started to elucidate Tc migration behavior and the structural stability in different Tc containing iron oxide forms. Future work will involve a rigorous DFT treatment that incorporates strong-electron correlations (DFT+U), to calculate the kinetic rates.
- Kinetic Monte Carlo models show differences in dissolution behavior of Fe, Mo, Ni as matrices for Tc solutes. To extend to oxides, a Buckingham type pair potential for TcO<sub>2</sub> oxide has been developed. Future work will involve the development of reactive force fields in Tc-O and Fe-Tc-O, to study oxidation and defects migration across metal/oxide interfaces, such as in the ReaxFF platform.
- As an initial step in assessing the viability of waste forms, technetium corrosion behavior was assessed. The films formed during electrochemical testing conditions do not show passivity. The nature of the film will be investigated in the future, but is surmised to be Tc(OH)<sub>4</sub> based on the literature, or other hydrated Tc (IV) phase. Future plans include electrochemical work across a broader pH range and along Tc binaries (likely alloying additions include Fe, Cr, Ni and Mo).

This work activity ties strongly with other experimental work on metal alloy waste form R&D within the SWF (MRWF) Campaign, such as the Waste Form Performance Testing and Modeling (WFPTM) activity at ANL (Fortner and Ebert, 2012). To support the Fractional Release Conceptual Model within WFPTM, the following components in this work package are considered to be important,

- Pure Tc oxidation, passivation, and Tc alloy corrosion rates in localized corrosion from modeling and electrochemical experiments
- Reactive force fields modeling of Tc transport between metal alloys and oxides
- Tc bulk incorporation mechanisms, including oxidation states in different iron oxides
- Mass transport of Tc and defects in a series of iron oxide phases

These processes/components contribute to the passivation and oxidation rates source terms in the Conceptual Model mentioned above, providing basis for integrating waste form degradation models with performance assessment (PA) models.

### 3.1.6 References

- Bloch P. E., 1994, Projector augmented-wave method, *Phys. Rev. B* **50**, 17953 (1994).
- Cartledge G. H., and W. T. Smith, Jr., 1955, Revision of the Electrode-Potential diagram for technetium, *J. Phys. Chem.* **59**, 1111 (1955).
- Chao C. Y., L. F. Lin, and D. D. Macdonald, 1981, A point defect model for anodic passive films: I. Film growth kinetics, *J. Electrochem. Soc.* **128**, 1187 (1981).
- Cobble J. W., W. T. Smith, Jr., G. E. Boyd, 1953, Thermodynamic properties of technetium and rhenium compounds. I. Vapor pressures of technetium heptoxide, pertechnic acid and aqueous solutions of pertechnic acid, *J. Am. Chem. Soc.* **75**, 5773 (1953).
- Cornell R., and U. Schwertmann, 2003, *The Iron Oxides: Structure, Properties, Reactions, Occurrences, and Uses* (Wiley-VCH, Weinheim, Germany), 2003.
- Crumm J. V., D. Stachan, A. Rohatgi, and M. Zumhoff, 2013, Epsilon metal waste form for immobilization of noble metals from used nuclear fuel, *J. Nucl. Mater.* **441**, 103 (2013).
- Forti M., P. Alonso, P. Gargano, G. Rubiolo, 2012, Transition metals monoxides. An LDA+*U* study, *Proc. Mater. Sci.* **1**, 230 (2012).
- Fortner J. A. and W. L. Ebert, 2012, *Status of static corrosion tests with RAW-1(Tc)*, FCRD-UFD-2012-000202.
- Glasso, F., 1970, *Structure and properties of inorganic solids*. Pergamon, New York, 1970.
- Hafner J., C. Wolverton, and G. Ceder, 2006, Towards computational materials design: The impact of density functional theory on materials research, *MRS Bulletin* **31**, 659 (2006).
- Henkelman G., B.P. Uberuaga, and H. Jonsson, 2000, A climbing image nudged elastic band method for finding saddle points and minimum energy paths, *J. Chem. Phys.* **113**, 9901 (2000).
- Jeon B., S. K. R. S. Sankaranarayanan, A. C. T. van Duin, and S. Ramanathan, 2011, Atomistic insights into aqueous corrosion of copper, *J. Chem. Phys.* **134**, 234706 (2011).
- Kaxiras, E., 2003, *Atomic and Electronic Structure of Solids* (Cambridge University Press, Cambridge, UK, 2003).
- Keiser D. D., D. P. Abraham, and J. W. Richardson, 2000, Influence of technetium on the microstructure of a stainless-steel zirconium alloy, *J. Nucl. Mater.* **277**, 333 (2000).
- Kim E., P. F. Weck, C. D. Taylor, O. Olatunji-Ojo, X.-Y. Liu, E. Mausolf, G. D. Jarvinen and K. R. Czerwinski, 2014, First-principles and kinetic Monte Carlo simulation studies of the reactivity of Tc(0001), MoTc(111) and MoTc(110) surfaces, *J. Electrochem. Soc.* **161**(3), C83 (2014).
- Kittel, C., 1996, *Introduction to Solid State Physics*, 7<sup>th</sup> ed., Wiley, New York, 1996.
- Klotz S., G. Rousse, Th. Strässle, C. L. Bull, M. Guthrie, 2006, Nuclear and magnetic structure of magnetite under pressure to 5.3GPa and at low temperatures to 130K by neutron scattering, *Phys. Rev. B* **74**, 012410 (2006).
- Kolman D., G. D. Jarvinen, C. D. Taylor, D. P. Moore, G. Goff, R. Gibson, M. Cisneos, E. Mausolf, P. F. Weck, E. Kim, 2011, Corrosion and passivity behavior of technetium waste forms, In *Corrosion - National Association of Corrosion Engineers: Houston, TX, 2011*.
- Krebs, B., 1969, Technetium(vII) oxide : A transition metal oxide with a molecular structure in the solid state, *Angewandte Chemie* **8**, 381 (1969)

- Kresse G. and J. Furthmüller, 1996, Efficiency of *ab-initio* total energy calculations for metals and semiconductors using a plane-wave basis set, *Comput. Mater. Sci.* **6**, 15 (1996).
- Lee J. and S. Han, 2013, Thermodynamics of native point defects in  $\alpha$ -Fe<sub>2</sub>O<sub>3</sub>: an *ab initio* study, *Phys.Chem. Chem. Phys.* **15**, 18906 (2013).
- Lemire R. J. and D. J. Jobe , 1996, Predicted behavior of technetium in a geological disposal vault for used nuclear fuel - Ramifications of a recent determination of the enthalpy of formation of TcO<sub>2</sub>(cr), *Mater. Res. Soc.* **412**, 873 (1996).
- Levine, I. N., 2000, *Quantum Chemistry* (Prentice HALL, Upper Saddle River, NY, 2000).
- Lin L. F., C. Y. Chao, and D. D. Macdonald, 1981, A point defect model for anodic passive films: II. Chemical breakdown and pit initiation, *J. Electrochem. Soc.* **128**, 1194 (1981).
- Liu X.-Y., D. A. Andersson, and B. P. Uberuaga, 2012, First principles DFT modeling of nuclear fuel materials, *J. Mater. Sci.* **47**, 7367 (2012).
- Macdonald, D., 2011, The history of the point defect model for the passive state: a brief review of film growth aspects, *Electrochim. Acta* **56**, 1761 (2011).
- MacDougall, B. and M. J. Graham, 2002, Growth and stability of passive films, in *Corrosion Mechanisms in Theory and Practice*, edited by P. Marcus (Marcel Dekker, Inc., New York, 2002), p. 189.
- Martinez, J. A., D. E. Yilmaz, T. Liang, S. B. Sinnott, and S. R. Phillpot, 2013, Fitting empirical potentials: Challenges and methodologies, *Current Opinion Solid State Mater. Sci.* **17**, 263 (2013).
- Methfessel, M., and A. T. Paxton, 1989, High-precision sampling for Brillouin-zone integration in metals, *Phys. Rev. B* **40**, 3616 (1989).
- Monkhorst, H. J. and J. D. Pack, 1976, Special points for Brillouin-zone integrations, *Phys. Rev. B* **13**, 5188 (1976).
- Muller, O., W. B. White, and R. Roy, 1964, Crystal chemistry of some technetium-containing oxides, *J. Inorg. Nucl. Chem.* **26**, 2075 (1964).
- Nørskov, J. K., F. Abild-Peterson, F. Studt, and T. Bligaard, 2011, Density functional theory in surface chemistry and catalysis, *Proc. Natl. Acad. Sci.* **108**, 937 (2011).
- Runevall, O., and N. Sandberg, 2011, Self-diffusion in MgO-a density functional study, *J Phys Condens Matter* **23**, 345402 (2011).
- Perdew, P., K. Burke, and M. Ernzerhof, 1996, Generalized gradient approximation made simple, *Phys. Rev. Lett.* **77**, 3865 (1996).
- Rollmann G., A. Rohrbach, P. Entel, and J. Hafner, 2004, First-principles calculation of the structure and magnetic phases of hematite, *Phys. Rev. B* **69**, 165107 (2004).
- Roth, W. L., 1958, Magnetic Structures of MnO, FeO, CoO, and NiO, *Phys. Rev.* **110**, 1333 (1958).
- Schrön, A., C. Rödl, and F. Bechstedt, 2012, Crystalline and magnetic anisotropy of the 3d-transition metal monoxides MnO, FeO, CoO, and NiO, *Phys. Rev. B* **86**, 115134 (2012)
- Schweika, W., A. Hoser, M. Martin, and A. E. Carlson, 1995, Defect structure of ferrous oxide Fe<sub>1-x</sub>O, *Phys. Rev. B* **51**, 15771 (1995).
- Schwochau, K., 2000, *Technetium: chemistry and radiopharmaceutical applications*. Wiley-VCH, 2000.
- Sherwin, M. E. and T. J. Drummond. 1991, Predicted elastic constants and critical layer thicknesses for cubic phase AlN, GaN, and InN on  $\beta$ -SiC, *J. Appl. Phys.* **69**, 8423 (1991).

- Skomurski, F. N., K. M. Rosso, K. M. Krupka, and B. P. McGrail, 2010, Technetium incorporation into hematite ( $\alpha$ -Fe<sub>2</sub>O<sub>3</sub>), *Environ. Sci. Technol.* **44**, 5855 (2010).
- Taylor, C. D., 2014, Oxidation of technetium metal as simulated by first principles, *J. Phys. Chem. C*, **118**, 10017 (2014).
- Taylor, C. D. and X.-Y. Liu, 2013, Investigation of structure and composition control over active dissolution of Fe–Tc binary metallic waste forms by off-lattice kinetic Monte Carlo simulation, *J. Nucl. Mater.* **434**, 382 (2013).
- Tempest, P. A. and R. K. Wild, 1985, Formation and growth of spinel and Cr<sub>2</sub>O<sub>3</sub> oxides on 20% Cr-25% Ni-Nb stainless steel in CO<sub>2</sub> environments, *Oxidation of Metals*, **23**, 207 (1985).
- Thorogood, G., 2011, Structure and cation ordering in spinel-type TcCo<sub>2</sub>O<sub>4</sub>. An example of a trivalent technetium oxide, *Dalton Trans.* **40**, 10924 (2011).

## 3.2 Modeling of Tc Incorporation into Fe-oxyhydroxides

During the reprocessing of commercial nuclear fuels or the vitrification of high-level defense waste, technetium (Tc) is an element of interest due to its volatility and tendency to partition among different waste streams (Darab and Smith, 1996; Um et al., 2011; McCloy et al., 2012). As such, separate waste forms are commonly considered for stabilizing Tc, such as borosilicate glasses (Darab and Smith, 1996; McCloy et al., 2012), metallic iron-technetium alloys (Taylor, 2011a,b; see Section 3.1 above), technetium sulfides, and iron oxides and iron oxy-hydroxides (Um et al., 2011 and references therein). Capturing Tc in metallic waste forms (MWFs; e.g., Fe-Tc alloys) as part of the separations and/or vitrification process is of interest because Tc-stainless steel alloys offer high waste loading and promising corrosion resistance (Taylor, 2011); however, the long-term corrosion behavior of these materials may also affect the Tc source term in a repository environment. Technetium is an element of interest during the long-term storage of nuclear materials because of its long half-life ( $2.1 \times 10^5$  years), high-mobility in the environment as the oxidized pertechnetate anion ( $\text{Tc(VII)O}_4^-$ ), and radiotoxicity as a beta emitter (Lieser and Bauscher, 1987; Meyer et al., 1991). While experiments can answer the question of “*Does Tc get incorporated into steel corrosion products?*” atomic-scale modeling provides a method for answering, “*How is Tc incorporated into steel corrosion products?*” This latter question has implications for the capacity of corrosion product iron oxides and iron oxy-hydroxides to retain Tc, and potentially other radionuclides, and how they may release Tc in a long-term disposal environment.

Here, atomic-scale modeling methods are used to investigate the incorporation of Tc into the iron oxy-hydroxide phase, goethite ( $\alpha\text{-FeOOH}$ ). Goethite was chosen for many reasons: 1) it is the most common iron oxy-hydroxide in nature (Alvarez et al., 2008); 2) it is a common steel corrosion product (Oh et al., 1999; Dodge et al., 2002); and 3) experimental results demonstrate that goethite can incorporate Tc(IV) into its structure, leading to the proposal of goethite as a waste form for Tc, as well (Um et al., 2011, 2012). With respect to the last point, uncertainty still remains as to the method of Tc(IV) incorporation into the goethite which has implications for Tc-fate during the corrosion of MWFs, as well as corrosion products as hosts for radionuclides in a repository environment. As such, three main research objectives are being addressed in this study using atomic-scale (quantum-mechanical) modeling techniques to determine: 1) the most favorable Tc incorporation mechanisms into the bulk goethite structure, 2) Tc affinity for bulk versus mineral surface sites of goethite, and 3) determining Tc stability in (near-) goethite surface sites in the presence of adsorbates, such as water ( $\text{H}_2\text{O}$ ), oxygen ( $\text{O}_2$ ), hydrogen ( $\text{H}_2$ ), and hydrogen peroxide ( $\text{H}_2\text{O}_2$ ). These species are under consideration because they contribute to our understanding of the long-term behavior of waste-form materials in storage environments, including scenarios involving radiolytic oxidants. The work presented in this Section provides an update on the first objective, bulk incorporation mechanisms and is from the milestone M4FT-14PN0804041, from the work package FT-14PN0804042.

### 3.2.1 Methods

#### 3.2.1.1 Quantum-Mechanical Calculations

Charge-localized, quantum-mechanical methods are being used to explore possible Tc incorporation scenarios in bulk goethite. Specifically, the modeling software CRYSTAL09 (Dovesi et al., 2005) is being used to calculate single-point energies and optimized geometries for bulk goethite models. From these models, charge-balanced, coupled substitution mechanisms will be evaluated to calculate Tc incorporation energies. The unrestricted Hartree Fock (UHF) level of theory, that allows for unpaired electronic spin, is being used based on previously successful modeling efforts involving the Tc-hematite system where discrete Fe(II)/Fe(III) and Tc(IV)/Tc(VII) charge distinctions were maintained during structure and energy optimizations (Skomurski et al., 2010a, and references therein). While combined HF-Density Functional Theory (DFT) methods may ultimately be used to more thoroughly account for the exchange and correlation contributions to the ground-state energy of the system (i.e., UHF methods account for exchange but not correlation energy contributions), UHF methods have been demonstrated to

successfully capture localized electron behavior in iron oxides (Rosso et al., 2003; Jordanova et al., 2005). These hybrid HF-DFT calculations can take place once initial UHF calculations are completed, using pre-optimized structures as a starting point to conserve computational time.

The first step in any modeling study is to determine the calculation parameters that are most appropriate for the system of interest, specifically basis-set testing, run parameter optimization, and capturing magnetic or electronic structure of the specific material. Basis sets being used for iron and technetium in this study were demonstrated to effectively capture discrete Fe(II) and Fe(III) behavior in previous studies on iron charge distribution in magnetite (Fe(II)Fe(III)<sub>2</sub>O<sub>4</sub>; Skomurski et al., 2010b.), and Tc (IV) versus Tc(VII) behavior in a study on Tc incorporation into hematite (Fe(III)<sub>2</sub>O<sub>3</sub>; Skomurski et al., 2010a and references therein). Run parameter testing led to a k-point density selection of 63 electronic sampling points in crystallographic space; higher k-point densities lead to a one-order of magnitude improvement in energy convergence relative to the previous k-point density selection (e.g.,  $2 \times 10^{-3}$  eV versus  $2 \times 10^{-4}$  eV energy change for 63 versus 36 k-points and 112 versus 63 k-points, respectively; see Table 3.2-1). While a higher k-point density could be considered for final calculations, 63 k-points are sufficient for testing a wide variety of goethite models.

**Table 3.2-1. Total energy versus k-point density in a single, ferromagnetic (FM) goethite unit cell.**

| Shrinking Factor | # k-points | Single-Point Energy (Ha) | Energy Diff. (n-(n-1))* (Ha) | Energy Diff. (n-(n-1))* (eV) |
|------------------|------------|--------------------------|------------------------------|------------------------------|
| 1 1              | 1          | -772.70401               | NA                           | NA                           |
| 2 2              | 8          | -214.09426               | 558.60975                    | 15200.32989                  |
| 3 3              | 14         | -214.11287               | -0.01861                     | -0.50652                     |
| 4 4              | 36         | -214.11397               | -0.00110                     | -0.02987                     |
| 5 5              | 63         | -214.11405               | -0.00008                     | -0.00227                     |
| 6 6              | 112        | -214.11406               | -0.00001                     | -0.00017                     |

\*Here, “n” refers to the current case, and “n-1” to the previous case.

In Table 3.2-1, energies in column four are reported in Hartrees and converted to electron volts (eV) in column five (1 Ha = 27.211 eV). In these calculations, the atomic positions, lattice parameters, and magnetic ordering of the iron atoms stayed the same while only the k-point density changed. Here, a ferromagnetic (FM) case was used where all iron atoms had the same direction of unpaired spins (e.g., all up or all down). A significant change in energy occurs when k-point density increases from 1 k-point in crystallographic space to 8 k-points; this result suggests that the single k-point was not robustly capturing the electronic structure of the goethite unit cell. Based on the minimal change in energy between 112 versus 63 k-points, the latter was chosen for all models to maximize computational resources while appropriately capturing the behavior of atoms in the goethite unit cell.

Regarding the magnetic structure of goethite, experimental studies suggest that it is antiferromagnetic at room temperature meaning it has no net-magnetic moment (Forsyth et al., 1968; Yang et al., 2006; Llavona et al., 2012). To achieve this, the four iron atoms in the unit cell must have equal and opposite, unpaired spin directions (e.g., 5 unpaired d-orbital electrons per each Fe<sup>3+</sup>). Different spin structures can be assigned and maintained during energy or geometry optimization of the unit cell. Four different magnetic ordering schemes were tested and will be discussed in the Results section.

### 3.2.1.2 Incorporation Energy Calculations

The schematic in Figure 3.2-1 describes the method for calculating incorporation energy ( $E_{inc}$ ) using atomic-scale models (i.e., solid-phase energies for the pure and doped-bulk models and gas-phase energies for the elements being substituted, e.g., Tc(IV), Fe(II), and Fe(III)):

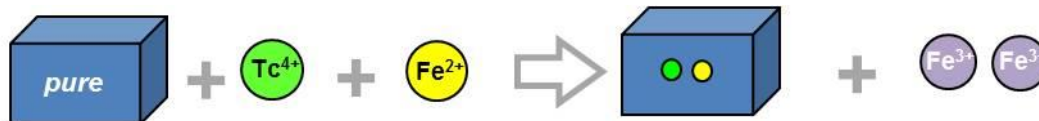


Figure 3.2-1. Schematic illustrating one possible charge-compensated substitution scheme where Tc(IV) and Fe(II) replace two lattice Fe(III) in bulk goethite. Blue rectangular prisms represent pure bulk goethite (left) and bulk goethite with substituted impurities (right). The right-hand side is the “Products” and the left-hand side is the “Reactants”.

Here, the blue box on the left represents the pure (un-doped) iron oxide phase, and the Tc(IV)/Fe(II)-doped or “defect” iron oxide phase on the right. In this case, two Fe(III) cations are removed to accommodate a charge-balanced substitution of Tc(IV) and Fe(II) into the bulk. The  $E_{inc}$  is the sum of the optimized energy for the doped iron oxide case and excised Fe(III) cations on the right, minus the sum of the energy of the optimized pure iron oxide plus the Tc(IV) and Fe(II) cations on the left. A negative incorporation energy would indicate favorable incorporation of the Tc(IV)/Fe(II) pair, while a positive energy would indicate unfavorable incorporation of the impurities. The cations being added or removed are being treated as gas phase species by calculating the energy of an atom in a box (e.g.,  $10 \times 10 \times 10 \text{ \AA}^3$ ) and accounting for its ionization energy. The pure and defect-phase bulk calculations are performed on infinite crystals (e.g., solids repeating infinitely in three-dimensions). Alternatively, solid-phase references can be used for the impurity phases, such as  $\text{TcO}_2 \cdot x\text{H}_2\text{O}$  for Tc(IV), following the method described by Shuller et al. (2013). Solvation energies can be applied impurity cations, as well, to simulate a more realistic, aqueous-based incorporation scenario. Previous studies suggest that this additional calculation may affect the magnitude of the incorporation energies, but not necessarily the trends, based on energy calculations of uranyl carbonate molecules treated as gas-phase, coordinated by water molecules, and subjected to a polarizable continuum model to simulate water (Schlosser et al., 2010). Such calculations could be considered when finalizing energies for Tc-incorporation models being develop here. Different Tc substitution schemes are discussed below.

### 3.2.1.3 Single Unit Cell and Supercell Models

A single goethite unit cell is orthorhombic with  $Pbnm$  space-group symmetry, and contains 16 atoms (see Figure 3.2-2). All structures in this paper have been built according to the lattice and atomic positions described in Yang et al. (2006) for a single crystal of goethite, where  $a = 4.5979 \text{ \AA}$ ,  $b = 9.9510 \text{ \AA}$ , and  $c = 3.0178 \text{ \AA}$ ;  $\alpha$ ,  $\beta$  and  $\gamma$  are all  $90^\circ$ . In goethite, each iron atom is octahedrally coordinated by 3 oxygen atoms and 3 hydroxyl groups. Two Fe atoms in the center of the unit cell are edge-sharing, and each of those Fe atoms shares a corner with an additional Fe atom at the top right and bottom left corners of the unit cell (see Figure 3.2-2). When extended in three dimensions, all Fe atoms share edges with Fe atoms in neighboring unit cells, forming chains parallel to the  $c$ -axis (i.e., into the paper). Another way to describe the unit cell is that half of the octahedral sites created by the oxygen sub-lattice are occupied by Fe atoms.

The motivation for using supercells to study Tc incorporation into goethite is to achieve experimentally-relevant Tc incorporation levels. For instance, by substituting a single Fe atom in a single unit cell with Tc, an impurity loading of 25 atomic % would result. For prior studies of Tc incorporation into hematite, 1-3 atomic % impurity loading was of interest based on experimental data (Skomurski et al., 2010 and references therein). While exact limits of Tc incorporation into goethite are not currently well established, there is interest in using models with more iron atoms such that a broad range of incorporation percentages can be explored. However, a trade-off exists between the number of atoms in a

system and computational time. In Table 3.2-2, the number of atoms per  $n \times n \times n$  supercell is presented, where  $n$  is the number of single unit cells per side of the supercell. A  $3 \times 3 \times 3$  unit cell containing 432 atoms was settled upon such that a substitution of one Tc atom for one Fe atom is approximately 1 atomic % impurity in the system (highlighted in bold in Table 3.2-2).

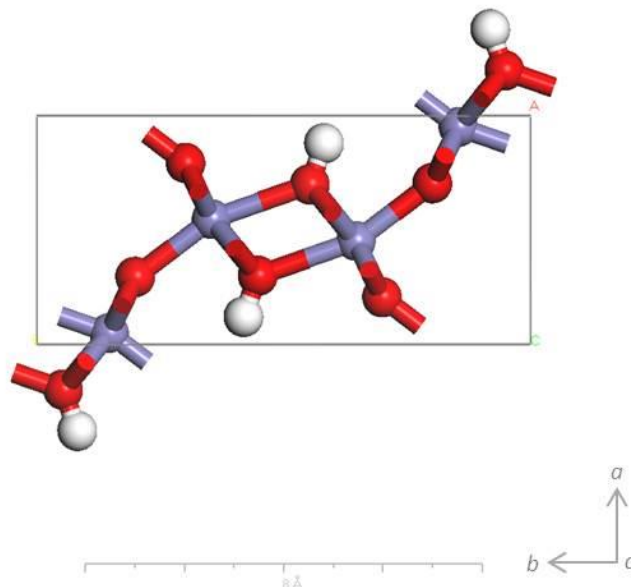


Figure 3.2-2. A single unit cell of goethite looking down the  $c$  axis. Purple spheres are iron, red spheres are oxygen, and white spheres are hydrogen. A scale bar is included for reference.

Table 3.2-2. Number and type of each atom in a goethite supercell when increasing dimensions by  $n \times n \times n$  unit cells.

| # Unit Cells / Side | # Iron Atoms | # Hydrogen Atoms | # Oxygen Atoms | # Total Atoms |
|---------------------|--------------|------------------|----------------|---------------|
| 1×1×1               | 4            | 4                | 8              | 16            |
| 2×2×2               | 32           | 32               | 64             | 128           |
| <b>3×3×3</b>        | <b>108</b>   | <b>108</b>       | <b>216</b>     | <b>432</b>    |
| 4×4×4               | 256          | 256              | 512            | 1024          |
| 5×5×5               | 500          | 500              | 1000           | 2000          |
| 6×6×6               | 864          | 864              | 1728           | 3456          |
| 7×7×7               | 1372         | 1372             | 2744           | 5488          |
| 8×8×8               | 2048         | 2048             | 4096           | 8192          |
| 9×9×9               | 2916         | 2916             | 5832           | 11664         |
| 10×10×10            | 4000         | 4000             | 8000           | 16000         |

## 3.2.2 Results

### 3.2.2.1 Magnetic Structure Calculations

As mentioned earlier, goethite exhibits antiferromagnetic behavior at room temperature (Yang et al., 2006; Forsyth et al., 1968; Llavona et al., 2012). Because each Fe(III) in the single goethite unit cell has five unpaired electrons in the same spin up or spin down orientation, each Fe(III) carries a net spin of 5. In order to cancel out the net spin of the unit cell, half the iron atoms must have opposite spins compared to the other half. In Figure 3.2-3, four different magnetic structures are illustrated: (a) ferromagnetic (FM) where all atoms have the same spin direction; (b) anti-ferromagnetic (AFM) where edge-sharing Fe(III) have opposite spin directions to each other and the corner sharing Fe(III) atoms; (c) anti-ferromagnetic-prime (AFM-P) where edge-sharing Fe(III) have the same spin and opposite spin from the corner sharing Fe<sup>3+</sup>; and (d) anti-ferromagnetic double-prime (AFM-DP) where edge sharing Fe(III) have opposite spin, but the same spin as neighboring, corner sharing Fe(III). The FM case has a net spin of 20 per unit cell; all other AFM cases have a net spin of 0.

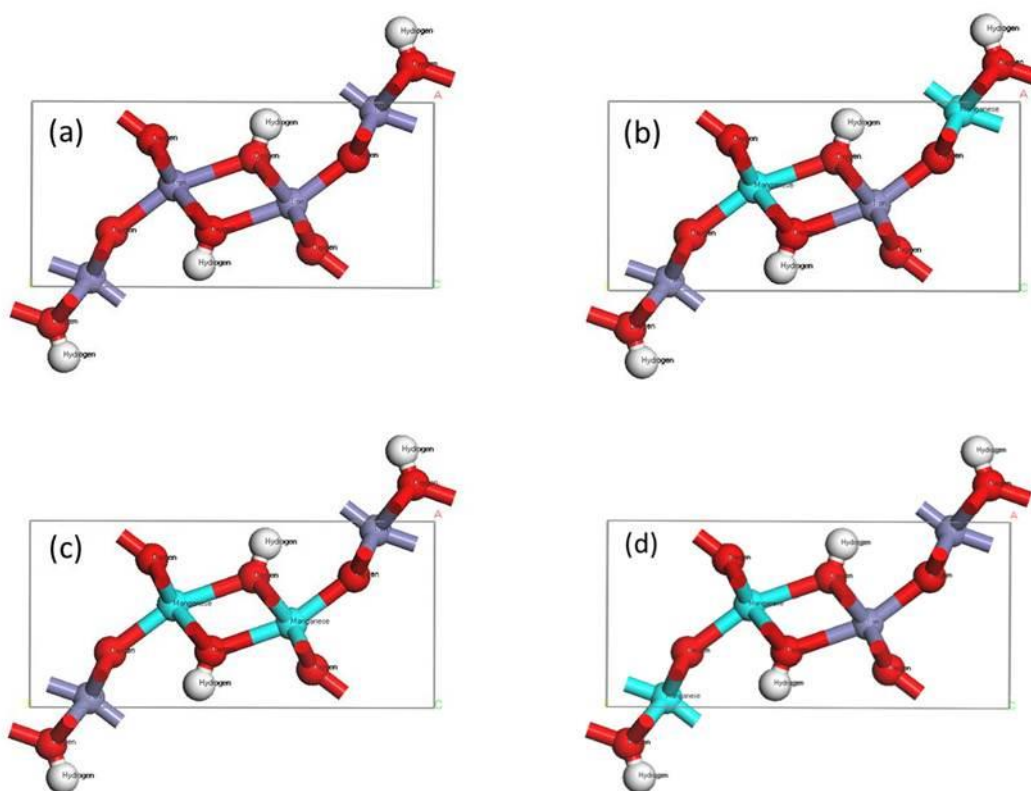


Figure 3.2-3. Four different magnetic structures for goethite represented by a single unit cell: a) ferromagnetic (all Fe(III) are spin up); b) anti-ferromagnetic (edge sharing Fe(III) octahedra have opposite spins); c) anti-ferromagnetic prime (edge-sharing Fe(III) octahedra have the same spin); and d) anti-ferromagnetic double-prime (edge-sharing Fe(III) octahedra have opposite spins; corner sharing Fe(III) octahedra have the same spin). Purple spheres are Fe(III) (spin up), cyan spheres are Fe(III) (spin down), red spheres are O, and white spheres are H.

In order to test for the lowest-energy magnetic structure, single point energy (SPE) calculations were performed on each of the unit cells shown above. Subsequently, geometry optimizations (GOPT), where only the atoms (not the lattice parameters) were allowed to move, were performed on the same models for comparison. Results are shown in Table 3.2-3.

Table 3.2-3. Single-point energy versus geometry optimized calculations for single goethite unit cells with different magnetic ordering on the iron sub-lattice.

| Filename           | # k points | Total Energy (Ha) | Fe spins ( $\times 2$ ) | Energy Difference* (Ha) | Energy Difference* (eV) |
|--------------------|------------|-------------------|-------------------------|-------------------------|-------------------------|
| FM Case (SPE)      | 63         | -214.11405        | $\pm 4.798$             | ---                     | ---                     |
| FM Case (GOPT)     | 63         | -214.16487        | $\pm 4.808$             | -0.05082                | -1.38284                |
| AFM Case (SPE)     | 63         | -214.11701        | $\pm 4.782$             | ---                     | ---                     |
| AFM Case (GOPT)    | 63         | -214.16698        | $\pm 4.795$             | -0.04997                | -1.35980                |
| AFM-P Case (SPE)   | 63         | -214.11724        | $\pm 4.784$             | ---                     | ----                    |
| AFM-P Case (GOPT)  | 63         | -214.16724        | $\pm 4.797$             | -0.05001                | -1.36074                |
| AFM-DP Case (SPE)  | 63         | -214.11375        | $\pm 4.796$             | ---                     | ---                     |
| AFM-DP Case (GOPT) | 63         | -214.16451        | $\pm 4.806$             | -0.05076                | -1.38134                |

\* Energy difference refers to cases with atomic positions optimized (EOPT) minus single-point energy cases (SPE), those without atomic-positions optimization.

Looking at “Total Energy” values for all cases tested, the GOPT values are approximately 0.05 Ha, or 1.36 eV lower in energy than the single-point energy calculations. This result is expected since atoms will move to find their lowest-energy position along calculated energy gradients with respect to the assigned atomic basis sets. When comparing SPE-optimized models in column 3, the AFM-P and AFM cases are nearly equivalent for the lowest energy, followed by the FM case, and the AFM-DP case with the least favorable optimized energy of all. For the two lowest-energy cases, the energy difference is approximately 0.0002 Ha, or 0.0054 eV. For the two highest-energy cases, the energy difference is of similar magnitude; however, the low cases versus the high cases are about 0.05 eV different in energy. The same trend is apparent when analyzing the GOPT results, where AFM-P and AFM cases are nearly equivalent with the lowest energy values, followed by the FM case, and the AFM-DP case with the highest optimized energy values. Values are similar, too with the two lowest cases differing by only 0.0003 Ha, or 0.0073 eV. Differences between the lowest-energy magnetic structures (AFM-P) and the highest-energy cases (AFM-DP) are an order of magnitude greater in energy (e.g., 0.095 and 0.074 eV) for both SPE and GOPT calculations, respectively.

When comparing these results to computational studies on fully-geometry optimized goethite models found in the literature, the AFM and AFM-P magnetic ordering cases have the lowest reported energies, with the AFM structure being slightly more favorable than the AFM-P structure, according to Guo and Barnard (2012). Least favorable is the AFM-DP case, followed by a ferromagnetic case. In a modeling study by Fuente et al. (2013), similar results were obtained with the AFM case being the lowest in energy of the three different AFM cases tested. This difference in lowest-energy trends may exist because lattice parameters were not yet allowed to relax fully in this study, for which further testing will be performed. Experimental Mössbauer spectroscopy studies also suggest that the AFM structure is also observed at room temperature (Forsythe et al., 1968); however, recent papers outline the complexity in determining the magnetic structure in goethite due to some magnetic orderings exhibiting similar energies to one another (Pankhurst et al., 2012). Moving forward, the two lowest energy magnetic structures determined here, AFM and AFM-P, will be used to generate super cells and Tc-incorporation models, although only AFM models will be illustrated in the following section.

### 3.2.2.2 Bulk Incorporation Models

Goethite is known to host many metal and metalloid impurities in nature such as aluminum manganese, chromium and nickel (Alvarez et al., 2008). In recent studies by Um et al. (2011, 2012), where Tc-bearing goethite was precipitated in the presence of Fe(II) and the pertechnetate anion,  $\text{TcO}_4^-$ , strong spectroscopic evidence points towards the incorporation of Tc into goethite as Tc(IV) rather than Tc(VII), or the pertechnetate anion. Based on the similarity in atomic radii between Tc(IV) and Fe(III), substitution into the octahedral Fe site is likely feasible. This type of mechanism is supported by previous modeling efforts where Tc(IV) was found to favorably substitute for Fe(III) in the hematite structure, along with the transformation of two Fe(III) to Fe(II) for charge balance (Skomurski et al., 2010a). Although goethite and hematite have different chemistries and structural arrangements of atoms, the Fe(III) coordination environment between them is similar and they are part of a temperature-based transformational series favoring hematite over goethite as temperature increases (Gualtieri and Venturelli, 1999). As such, it is possible that similar Tc(IV) substitution mechanisms could be favored in both (see Figure 3.2-4a).

In contrast to hematite, where excess Fe(II) is observed in the  $\text{Fe}_2\text{O}_3$  structure upon incorporation of  $M^{4+}$  impurities, such as titanium, where  $M$  stands for metals (Droubay et al., 2007), a study by Berry et al. (2000) suggests that no excess Fe(II) is observed in the goethite upon substitution of Sn(IV) for Fe(III) when X-ray photoelectron spectroscopy (XPS) was used to probe samples. Instead, a number of direct or interstitial Sn(IV) substitutions for Fe(III) were tested using empirical potential modeling methods to account for experimental observations. In that case, a coupled Fe(III) + vacancy substitution had the lowest energy, followed by coupled Fe(III) + OH- vacancies, Fe(III) + O<sup>2-</sup> vacancies, with an interstitial Sn(IV) having the highest, or least favorable, incorporation energy (Berry et al., 2000). Out of those models described in that paper, two mechanisms are being tested here, one where Tc(IV) replaces a lattice Fe(III) directly, and the nearest  $\text{H}^+$  is removed for remaining charge balance (Figure 3.2-4b), and another case where interstitial  $\text{Tc}^{4+}$  occupies an empty Fe-octahedral site, charge compensated by removing four nearest-neighbor  $\text{H}^+$  to maintain charge neutrality (Figure 3.2-4c). These three models are being used as a starting point for SPE and GOPT energy calculations that will ultimately be coupled with incorporation energy calculations, as outlined in Figure 3.2-1, to determine which Tc(IV) incorporation mechanisms are most favorable in goethite. Additional models, as described for  $\text{UO}_2^{2+}$  substitution into iron oxides by Kerisit et al. (2011) will also be used as a guide for exploring the parameter space for Tc(IV) incorporation into goethite.

Once the most energetically favorable Tc incorporation scheme is identified, additional goethite super cells will be generated into which increasing amounts of Tc can be added in the same fashion. In this way, the effect of Tc loading on  $E_{inc}$  can be evaluated to determine if there is an incorporation limit for Tc in the goethite structure, or at least if a limit is approaching. Ultimately, surface slabs will be generated using the most stable incorporation mechanism to investigate the effect of free surfaces and adsorbates on Tc stability in iron oxide corrosion products of metallic Fe-Tc waste forms.

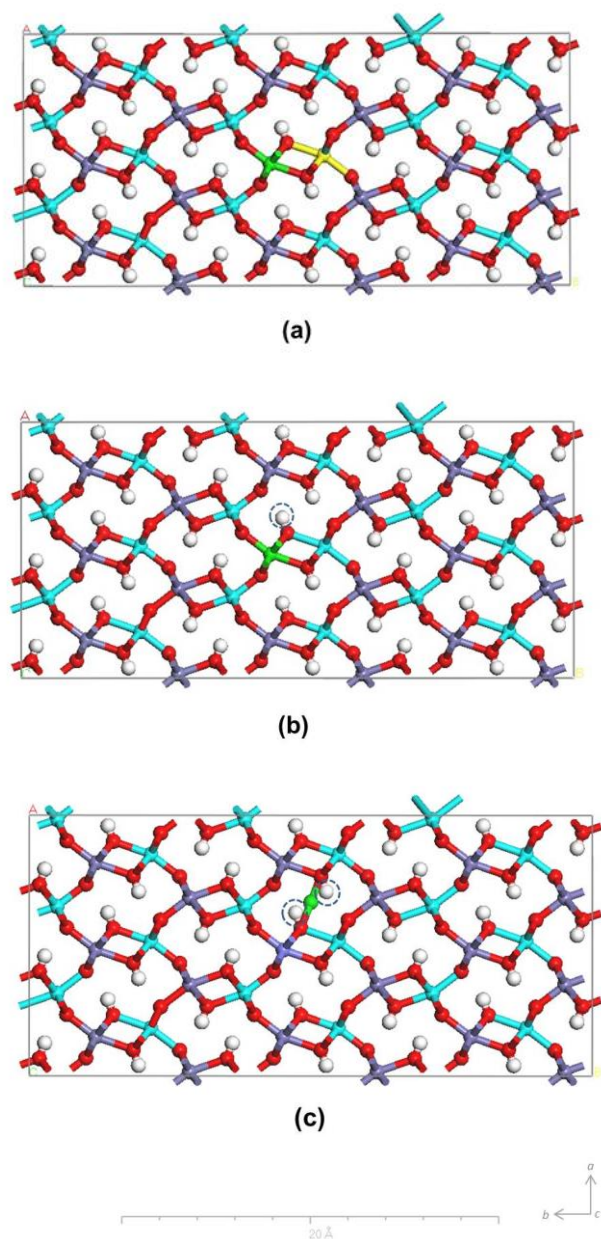


Figure 3.2-4. Goethite supercells (3×3×3) representing the anti-ferromagnetic (AFM) spin structure illustrating three different Tc(IV) substitution schemes: a) coupled Tc(IV) (green) / Fe(II) (yellow) substitution for two lattice Fe(III); b) Tc(IV) substitution of one lattice Fe(III) and removal of one H<sup>+</sup> for charge balance; and c) interstitial Tc(IV) addition to the supercell and removal of four nearest-neighbor H<sup>+</sup> for charge balance. A 20 Å scale-bar is included for reference. Purple spheres are Fe(III) (spin up), aqua spheres are Fe(III) (spin down), red spheres are O<sub>2</sub><sup>-</sup>, and white spheres are H<sup>+</sup>; additionally, green spheres are Tc(IV) spin up and yellow spheres are Fe(II) spin down.

### 3.2.3 Discussion

#### 3.2.3.1 Connections to Metallic Waste Form Research Objectives

The Tc incorporation into goethite modelling effort described here is part of a larger body of modeling and experimental studies being performed on Tc-bearing MWFs within the UFD Campaign (at LANL and UNLV; see Section 3.1). Specifically, MWF-oxide interfaces are being studied using electrochemical and surface-characterization methods, in addition to fundamental corrosion studies being performed on MWF

using atomic-scale modeling methods, building on previous work in this area. In this work, atomic-scale modeling efforts are focused on understanding Tc-incorporation and metal diffusion in a series of increasingly oxidized iron oxides (e.g., FeO to Fe<sub>3</sub>O<sub>4</sub> to Fe<sub>2</sub>O<sub>3</sub>, etc.) to understand incorporation mechanisms and Tc stability as a function of oxidation and the presence of other transition metals. The differences between modeling efforts at PNNL and UNLV is the use of iron oxy-hydroxide phases versus iron oxides, respectively, and the ultimate trajectory of focusing on Tc stability at goethite-environmental interfaces at PNNL versus the bulk behavior or Tc in different iron oxides at UNLV.

During the current fiscal year (FY14), discussion increased among individuals at different institutions working on research under the umbrella the “*Metal Corrosion Mechanisms*” project (FT-14PN0804042) to ensure that common and complementary research goals were being met across participating organizations. These efforts are highlighted in Figure 3.2-5. Along those lines, it was important to ensure that experimental and theoretical research results could also be used to constrain a larger-scale, fractional release (FR) model (see Figure 3.2-5) that could be of direct use within a PA model to analyze radionuclide behavior in a generic repository environment.

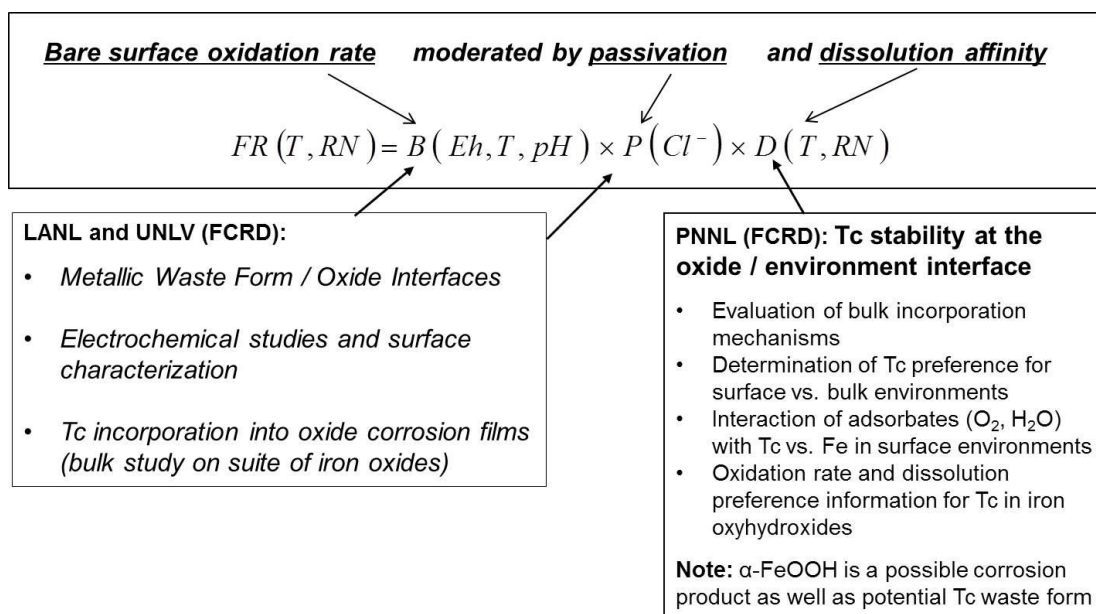


**Figure 3.2-5. Schematic illustrating how “Metal Corrosion Mechanisms” research at PNNL, LANL, and UNLV contributes to a conceptual model describing fractional release (FR) of radionuclides from MWF.**

In brief, the FR equation above was used to show where research results from “*Metal Corrosion Mechanisms*” projects fits into the components of the equation, where  $B$  is a bare surface oxidation rate as a function of Eh, T, and pH;  $P$  is a passivation term that can be affected different ion concentrations or species present in solution; and  $D$  is a dissolution affinity term that depends on temperature and radionuclide species. As seen in the bottom right corner of Figure 3.2-5, the study of Tc incorporation into iron oxy-hydroxides feeds the dissolution affinity term most directly by, 1) understanding how, and how much, Tc is incorporated into the goethite structure; 2) by evaluating whether Tc prefers a surface versus bulk environment in goethite (which affects its availability for release), and 3) understanding how strongly Tc interacts with adsorbates when in the goethite structure. Ultimately, reaction rates for Tc oxidation will be calculated when the third phase of this research project is reached. Experimental and theoretical research at LANL and UNLV (bottom left corner of Figure 3.2-5) contribute more directly to the bare surface oxidation rate term, as well as the passivation rate term. Technetium incorporation into iron oxides and oxyhydroxides can help constrain the dissolution affinity term by elucidating bulk incorporation mechanisms.

### Connections to Used Fuel Disposition Research Objectives

While the Tc incorporation into iron oxy-hydroxides research described here stems from MWF origins, it has broad application to UFD research objects, largely due to the potential for significant amounts of iron in a repository environment to interact with stored radionuclides. Various source locations (Figure 3.2-6) in an Engineered Barrier System (EBS) will have Tc interaction with iron oxides that may affect waste form performance in a generic disposal scenario, and each is being evaluated from a process model standpoint. There is the waste form itself in which Tc would be a large component of a metal-alloy waste. For the MWF, radionuclide mobilization may bring Tc into contact with corroding steel and corrosion products. Corrosion products (i.e., iron oxides and iron oxy-hydroxides) may incorporate Tc, within certain limits, to serve as sinks for mobilized radionuclides. All of these processes ultimately affect the “Source Term” to be included in the PA model (shown at the top of Figure 3.2-6)

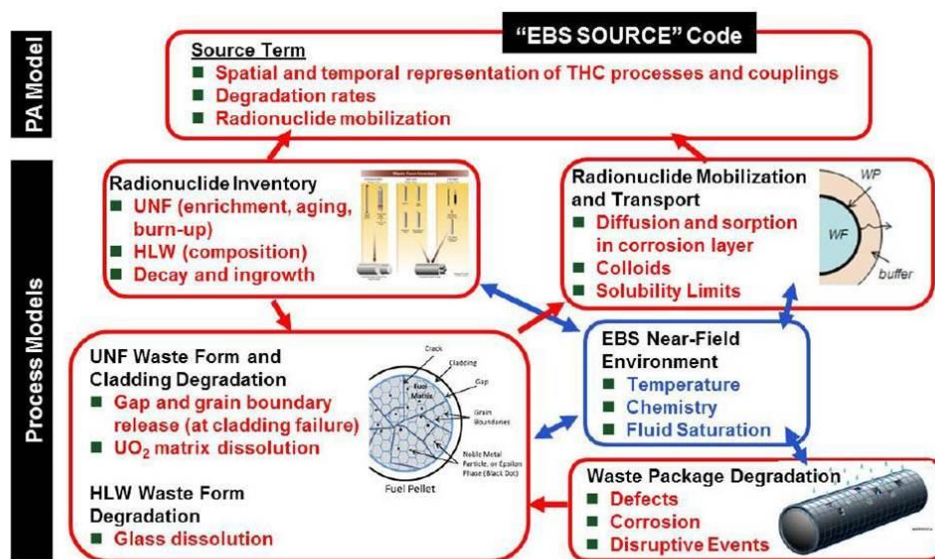


Figure 3.2-6. Schematic illustrating different processes that contribute to an overall understanding of radionuclide source terms for a generic disposal system. The individual “Process Models,” including inventory, waste form, and waste package degradation processes, ultimately feed into the radionuclide source term as part of a “Probabilistic Assessment” (PA) Model (from Freeze et al., 2013, Figure 2-11).

Tc is a radioelement of interest due to its long half-life, high mobility in the environment as the oxidized pertechnetate anion ( $TcO_4^-$ ), and its radiotoxicity (Lieser and Bauscher, 1987; Meyer et al., 1991). In irradiated fuel, Tc makes up approximately 6% of total fission product content and is found primarily in the epsilon metal phase that precipitates out at grain boundaries and within the  $UO_2$  matrix grains (Kleykamp, 1985; Cui et al., 2004; Bruno and Ewing, 2006; Um et al., 2011). As such, if waste packages are compromised (Figure 3.2-6, bottom right), and the fuel matrix degrades, Tc will interact with WP corrosion products. Assuming that the WP is iron-bearing, Tc could be incorporated into the iron corrosion products (including goethite). Finally, waste package degradation may affect local Eh and pH conditions if hydrogen gas is generated (Carbol et al., 2009). Also, corrosion products may have a “self-sealing” effect on waste packages and help maintain the integrity of the fuel as a waste form by protecting it from further interaction with environmental variables (Ferriss et al., 2009). As such, radionuclide interaction with iron corrosion products will play a significant role in predicting the long-term behavior of used fuel or metallic waste forms in a repository environment.

### 3.2.4 References

- Alvarez, M., Sileo, E.E., and Rueda, E.H. (2008) Structure and reactivity of synthetic Co-substituted goethites. *American Mineralogist*, 93, 584-590.
- Berry, F.J., Helgason, Ö., Bohórquez, A., Marco, J.F., McManus, J., Moore, E.A., Mørup, S., and Wynn, P.G. (2000) Preparation and characterization of tin-doped  $\alpha$ -FeOOH (goethite). *Journal of Materials Chemistry*, 10, 1643-1648.
- Bruno, J. and Ewing, R.C. (2006) Spent Nuclear Fuel. *Elements*, 2(6), 343-349.
- Carbol, P., Fors, P., Gouder, T., and Spahiu, K. (2009) Hydrogen suppresses UO<sub>2</sub> corrosion. *Geochimica et Cosmochimica Acta*, 73, 4366-4375.
- Cui, D., Low, J., Sjostedt, C.J., and Spahiu, K. (2004) On Mo-Ru-Tc-Pd-Rh-Te alloy particles extracted from spent fuel and their leaching behavior under Ar and H<sub>2</sub> atmospheres. *Radiochimica Acta*, 92, 551-555.
- Darab, J.G. and Smith, P.A. (1996) Chemistry of technetium and rhenium species during low-level radioactive waste vitrification. *Chemistry of Materials*, 8, 1004-1021.
- Dodge, C.J., Francis, A.J., Gillow, J.B., Halada, G.P., Eng, C., and Clayton, C.R. (2002) Association of uranium with iron oxides typically formed on corroding steel surfaces. *Environmental Science & Technology*, 36, 3504-3511.
- Dovesi, R., Orlando, R., Civalleri, B., Roetti, C., Saunders, V. R. and Zicovich-Wilson, C. M. (2005) CRYSTAL: a computational tool for the ab initio study of the electronic properties of crystals. *Zeitschrift für Kristallographie*, 220, 571-573.
- Droubay, T., Rosso, K.M., Heald, S.M., McCready, D.E., Wang, C.M., and Chambers, S.A. (2007) Structure, magnetism, and conductivity in epitaxial Ti-doped  $\alpha$ -Fe<sub>2</sub>O<sub>3</sub> hematite: Experiment and density functional theory calculations. *Physical Review B*, 75, 104412.
- Ferriss, E.D.A., Helean, K.B., Bryan, C.R., Brady, P.V., and Ewing, R.C. (2009) UO<sub>2</sub> corrosion in an iron waste package. *Journal of Nuclear Materials*, 384, 130-139.
- Forsyth, J.B., Hedley, I.G., and Johnson, C.E. (1968) The magnetic structure and hyperfine field of goethite ( $\alpha$ -FeOOH). *Journal of Physics C (Proc. Phys. Soc.)*, 2(1), 179-188.
- Freeze, G., Gardner, W.P., Vaughn, P., Sevougian, S.D., Mariner, P., Mousseau, V., and Hammond, G (2013) Enhancements to Generic Disposal System Modeling Capabilities. FCRD-UFD-2014-000062, SAND2013-10532P, Sandia National Laboratories, Albuquerque, NM.
- Fuente, S.A., Belelli, P.G., Castellani, N.J., and Avena, M. (2013) LDA+*U* and GGA+*U* studies of Al-rich and bulk goethite ( $\alpha$ -FeOOH). *Materials Chemistry and Physics*, 137, 1012-1020.
- Gualtieri, A.F. and Venturelli, P. (1999) In situ study of the goethite-hematite phase transformation by real time synchrotron powder diffraction. *American Mineralogist*, 84, 895-904.
- Guo, H. and Barnard, A.S. (2011) Modeling the iron oxides and oxyhydroxides for the prediction of environmentally sensitive phase transformations. *Physical Review B*, 83, 094112.
- Iordanova, N., Dupuis, M., and Rosso, K.M. (2005) Charge transport in metal oxides: a theoretical study of hematite  $\alpha$ -Fe<sub>2</sub>O<sub>3</sub>. *Journal of Chemical Physics*, 122, 144305.
- Kerisit, S., Felmy, A.R., and Ilton, E.S. (2011) Atomistic simulations of uranium incorporation into iron (hydr)oxides. *Environmental Science & Technology*, 45, 2770-2776.
- Kleykamp, H. (1985) The chemical state of the fission products in oxide fuels. *Journal of Nuclear Materials*, 131, 221-246.

- Lieser, K.H. and Bauscher, C. (1987) Technetium in the hydrosphere and in the geosphere I. Chemistry of technetium and iron in natural waters and influence of the redox potential on the sorption of technetium. *Radiochimica Acta*, 42, 205-213.
- Llavona, Á., Prados, A., Velasco, V., Crespo, P., Sánchez, M.C., and Pérez, L. (2013) Electrochemical synthesis and magnetic properties of goethite single crystal nanowires. *CrystEngComm*, 15, 4905-4909.
- McCloy, J.S., Riley, B.J., Goel, A., Liezers, M., Schweiger, M.J., Rodriguez, C.P., Hrma, P., and Kim, D.-S. (2012) Rhenium solubility in borosilicate nuclear waste glass: Implications for the processing and immobilization of technetium-99. *Environmental Science & Technology*, 46, 12616-12622.
- Meyer, R.E., Arnold, W.D., Case, F.I., and O'Kelley, G.D. (1991) Solubilities of Tc(IV) oxides. *Radiochimica Acta*, 55(1), 11-18.
- Oh, S.J., Cook, D.C., and Townsend, H.E. (1999) Atmospheric corrosion of different steels in marine, rural and industrial environments. *Corrosion Science*, 41, 1687-1702.
- Pankhurst, Q.A., Barquín, L.F., Lord, J.S., Amato, A., and Zimmermann, U. (2012) Intrinsic magnetic relaxation in goethite. *Physical Review B*, 85, 174437.
- Rosso, K.M., Smith, D.M., and Dupuis, M. (2003) An ab initio model of electron transport in hematite ( $\alpha$ -Fe<sub>2</sub>O<sub>3</sub>) basal planes. *Journal of Chemical Physics*, 118(14), 6455-6466.
- Schlosser, F., Moskaleva, L.V., Kremleva, A., Kruger, S., and Rosch, N. (2010) Comparative density functional study of the complexes [UO<sub>2</sub>(CO<sub>3</sub>)<sub>3</sub>]<sup>4-</sup> and [(UO<sub>2</sub>)<sub>3</sub>(CO<sub>3</sub>)<sub>6</sub>]<sup>6-</sup> in aqueous solution. *Dalton Transactions*, 39, 5705-5712.
- Shuller, L.C., Ewing, R.C., and Becker, U. (2013) Np-incorporation into uranyl phases: A quantum-mechanical evaluation. *Journal of Nuclear Materials*, 434, 440-450.
- Skomurski, F.N., Rosso, K.M., Krupka, K.M., and McGrail, B.P. (2010a) Technetium incorporation into hematite ( $\alpha$ -Fe<sub>2</sub>O<sub>3</sub>). *Environmental Science & Technology*, 44, 5855-5861.
- Skomurski, F.N., Kerisit, S., and Rosso, K.M. (2010b) Structure, charge distribution, and electron hopping dynamics in magnetite (Fe<sub>3</sub>O<sub>4</sub>) (100) surfaces from first principles. *Geochimica et Cosmochimica Acta*, 74, 4234-4248.
- Taylor, C.D. (2011a) Cohesive relations for surface atoms in the iron-technetium binary system. *Journal of Metallurgy*, 2011, Article ID 954170, 1-8.
- Taylor, C.D. (2011b) Surface segregation and adsorption effects of iron-technetium alloys from first-principles. *Journal of Nuclear Materials*, 408, 183-187.
- Um, W., Chang, H.-S., Icenhower, J.P., Lukens, W.W., Serne, R.J., Qafoku, N.P., Westick, Jr., J.H., Buck, E.C., and Smith, S.C. (2011) Immobilization of 99-Technetium(VII) by Fe(II)-goethite and limited reoxidation. *Environmental Science & Technology*, 4904-4913.
- Um, W., Chang, H., Icenhower, J.P., Lukens, W.W., Serne, R.J., Qafoku, N., Kukkadapu, R.K., and Westsik, J.H. Jr. (2012) Iron oxide waste form for stabilizing <sup>99</sup>Tc. *Journal of Nuclear Materials*, 429, 201-209.
- Yang, H., Lu, R., Downs, R.T., and Costin, G. (2006) Goethite,  $\alpha$ -FeO(OH), from single-crystal data. *Acta Crystallographica*, E62, i250-i252.

## 4. Integrating Waste Form Models into Performance Assessment Models

Performance assessment models provide a common conceptual and computational framework for the simulation of coupled thermal-hydrologic-chemical-mechanical-biological-radiological processes that govern the behavior of nuclear waste disposal systems (Freeze and Vaughn, 2012). Within the common performance assessment models framework, a range of disposal system alternatives (combinations of inventory, EBS design, and geologic setting) can be evaluated using appropriate model fidelity that can range from simplified reduced-dimension representations running on a desktop computer to complex coupled relationships running in a high-performance computing environment (see e.g., Figure 2.1-1 in Sassani et al., 2012).

A general strategy for incorporating models of spent fuel degradation into PA models was initially described in Sassani et al. (2012) and subsequently refined the following year (Sassani et al., 2013a, b). As discussed below, PA models within UFD have generally focused on the spent/used nuclear fuel (SNF/UNF) as the source term, but this fiscal year additional modeling activities for the glass waste form and metallic waste forms came under the UFD Campaign purview. The existing approach for incorporation of process-based waste form degradation models into the PA models is now expanded to include these.

### 4.1 General Approach

Within the PA model the EBS is conceptualized with a number of major barriers of various types, depending on disposal environment, as well as with various waste forms including SNF/UNF that is the primary waste form by activity and by volume projected out to the year 2048 (SNL 2014) and high-level waste (HLW) glass (Figure 4.1-1). A number of the models implemented currently in the PA model for the EBS are more idealized than fully coupled, but the plan is to augment or replace those simpler models with more comprehensively coupled process models as the work progresses. It should be noted that waste form degradation and behavior of the major barriers in the EBS are the key features of the PA model integration structure envisioned (Freeze et al., 2013). For example, Figure 4.1-2 shows the “Source Term and EBS Evolution” (top-left) box delineating waste form (WF) degradation as part of the breakdown of key source-term and EBS coupled processes within the PA integration scheme and code capabilities. Models for used fuel degradation processes are expected to be some of the earliest augmentations implemented within the PA Model. The glass waste form degradation models would be the next highest priority based on volume of materials (see SNL 2014), with other models for more specialized waste forms being lower priority.

Consideration of the physico-chemical evolution of the post-closure environment is needed when evaluating models for waste form degradation either on their own, or within the PA models. Temporal evolution of both the natural and engineered barriers in the system will include thermal, hydrologic, chemical, and mechanical changes driven by the system initial and boundary conditions, as well as by the placement of the waste forms into that system. Thermal perturbations from heat-generating waste forms are one of the most prominent aspects of such evolution.

A stylized example of the chronological evolutions of such system conditions is shown in Figure 4.1-3 for an argillite (clay/shale) disposal environment. This figure is based on a similar chronological description for THMC coupled processes in an argillite repository for the TIMODAZ project described in Yu et al. (2010). The thermal evolution is driven primarily by the radioactive decay of the used fuel and provides coupled effects within the three other process areas (e.g., drying of the immediate vicinity). Note that the chemical conditions are those imposed from the evolution of the natural system and the engineered barriers excluding the waste form itself. The waste form degradation models discussed within this report are those that would evaluate additional chemical aspects of the glass or metallic waste forms that may drive bulk chemical changes. In general, the point in time of waste package failures will be out in time

after the system thermal perturbation has decreased. This is just one example of such temporal changes for one possible generic disposal system and the process models in this report are developed to be able to address the ranges of possible conditions, focusing primarily on the dominant conditions expected for waste form degradation during post closure.

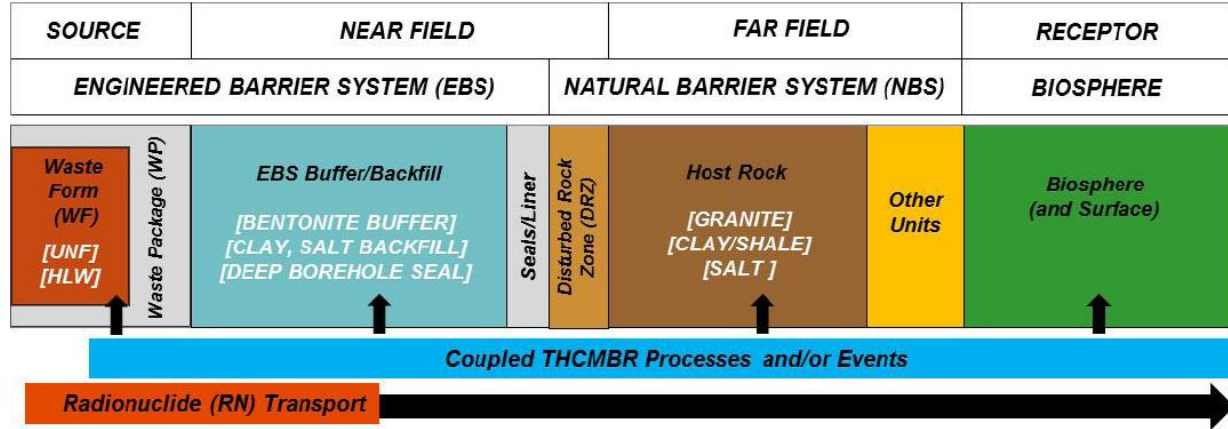


Figure 4.1-1. Features and phenomena to be represented in the PA model of a generic disposal system.

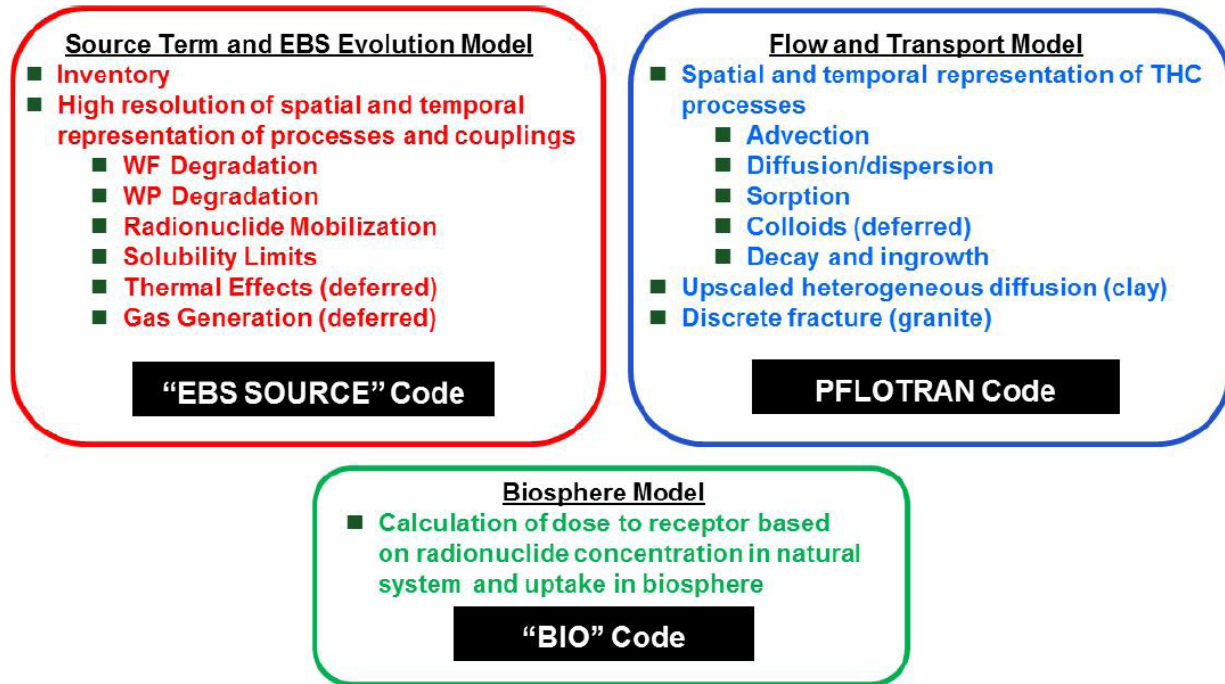


Figure 4.1-2. Disposal system integrated process model capabilities in codes for the PA model (Freeze et al. 2013).

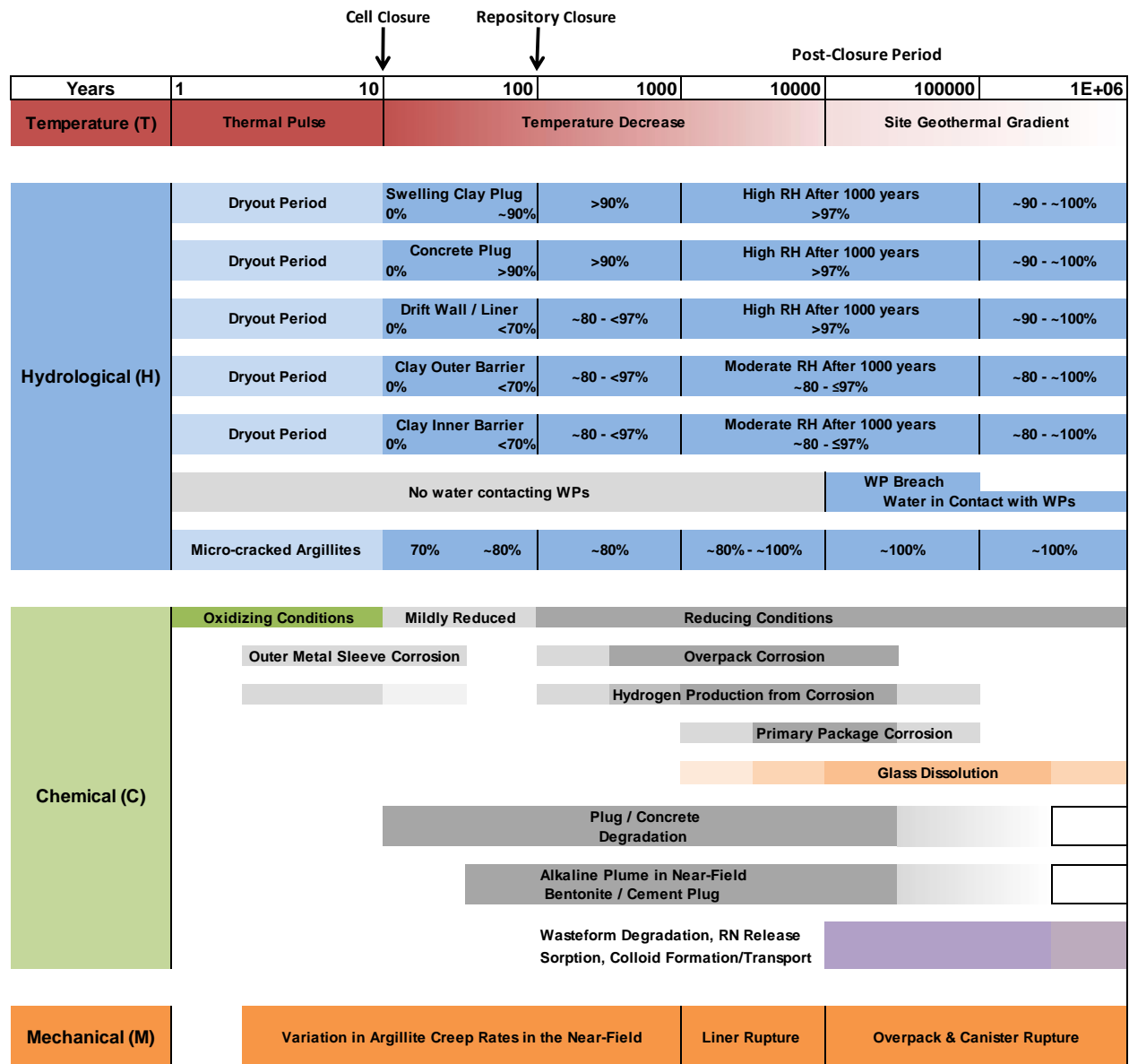


Figure 4.1-3. Schematic example of an idealized chronological evolution of the thermal, hydrologic, mechanical, and chemical (THMC) conditions for a generic shale/argillite disposal environment. Percentages in the hydrological part of the diagram represent percent of water saturation in the media.

For the source-term models of the four generic disposal environments, the implementations are generally simplified. For example, in Clayton et al. (2011) the generic salt source-term model is described as follows:

*Waste form degradation is assumed to release radionuclides into a large uniformly mixed container representative of the source-term water volume. The source-term water volume is obtained by multiplying the source-term bulk volume by its porosity. The dissolved concentrations of radionuclides in the source term mixing cell are then calculated based on the mass of radionuclides released from the waste form, the source-term water volume, and the radionuclide solubility. ... As the model matures and information becomes available, more realistic representations of the processes will replace this initial simplified approach.*

Within that generic salt source-term model, the glass degradation rate is represented as follows:

*For the DHLW and CHLW, the waste form is borosilicate glass. For both waste form types, the waste form degradation in the source-term model is represented with an annual fractional degradation rate (i.e., fraction of remaining waste mass degraded per year), with a distribution that captures potential range of degradation rates that could be expected in a generic salt repository environment.*

The above waste form degradation activities are part of a larger set of activities in the MRWF Campaign that will provide augmented models for glass and metallic waste form degradation for use in PA models. Implementation of those models into PA models will initially follow a similar path as that being implemented for the spent/used fuel degradation model whereby the primary connection will be the supply of a calculated fractional degradation rate to the PA model, versus simple sampling of a distribution. As the implementation matures, connections/couplings will become more abundant to address the various input/output needed by the specific waste form model interaction with the other models for components of the EBS. This progression is also similar to that expected for the spent fuel degradation models; however the specifics of the connections/couplings are likely to be different for each particular waste form degradation model.

## 4.2 Connections to other Processes in the PA Model

The primary initial connection into the current performance assessment models for the glass and metallic waste form degradation models is the fractional degradation rate (FDR) parameter, which is currently sampled from a distribution as indicated above. This primary coupling allows for development of more process-based models that are able to supplant the FDR distribution by supplying that parameter directly as a result of the process model. This is the initial connection that is needed for implementation of the UF MPM described above. Additionally, if secondary phases are formed that will incorporate some fraction of the radionuclides being released from the glass or metal waste form, quantification of the amounts so sequestered and the rate of dissolution of the secondary phase would be another set of connections that could be defined.

A coarse connection to chemical environment (defined in the performance assessment models and needed as input to the waste form degradation models) exists currently in the form of the four generic disposal environments. At present this is sufficient as the models discussed herein are developed in general for dilute groundwater in reducing environments. Explicit coupling to major chemistry variation is expected to be an ongoing enhancement, with the model applicability in granite or clay/shale systems being relatively straightforward, whereas extending to deep borehole environments, or salt brine environments appropriate a larger effort to be done in the future, if needed. This is also the case for thermal and pressure dependencies (the latter primarily related to reactions that are directly affected by gas fugacities, such as redox controls) that will be further incorporated into the waste form degradation models and will capture

essential environment and temporally-changing conditional parameters. It is expected that as these enhanced models are incorporated into the performance assessment models, expanding explicit environment/chemical variability coverage within the models will become more efficient.

Our general strategy for integrating process models with each other, and within the performance assessment models, is to identify initially the major feeds among the process models and from the process models to performance assessment models (see below for discussion of connections). For coupling into performance assessment models, our approach begins with the direct, though idealized, interface connections that exist, with further couplings added as the process models themselves become more highly coupled.

One more simplistic approach to coupling to the PA models would be to use waste form degradation process models to generate a set of histories based on temperature and waste form. This could be done initially for each generic disposal chemical environment (e.g., granitic groundwater or clay/shale), and simply directing the PA model to select the appropriate set of histories to sample depending on which environment was being analyzed. This is an efficient approach with little potential conservatism.

Such an idealized coupling using histories may only be an initial stage of coupling the waste form degradation models with PA models and the preferred approach is the direct incorporation of the coupled process model into the PA models, as will be done with the spent fuel degradation model as the initial case. Such an approach can start simply (the PA model supplying basic physical parameters such as T) and progress to a more thorough coupling that would entail passing water compositional parameters (potentially from other internal chemistry models) as input to waste form degradation models, which would analyze the waste form degradation in that particular environment and provide the fractional degradation rate for those specific water compositions. This would be a bidirectional connection example (i.e., inputs and outputs both ways). Further coupling of the waste form degradation models into the PA model with a full suite of coupled THC processes would allow a fully coupled feedback where, for example, in addition to the fractional degradation rate being provided to the performance assessment models, the change to water composition based on the glass waste form degradation could be supplied back to the PA model as well. The potential connections between the glass or metallic waste form degradation models and the other PA model subsystems are shown in Figure 4.2-1. Such a staged developmental strategy facilitates incorporation of process-level detail as it is available and permits an evolving level of model complexity to be incorporated in a deliberate manner.

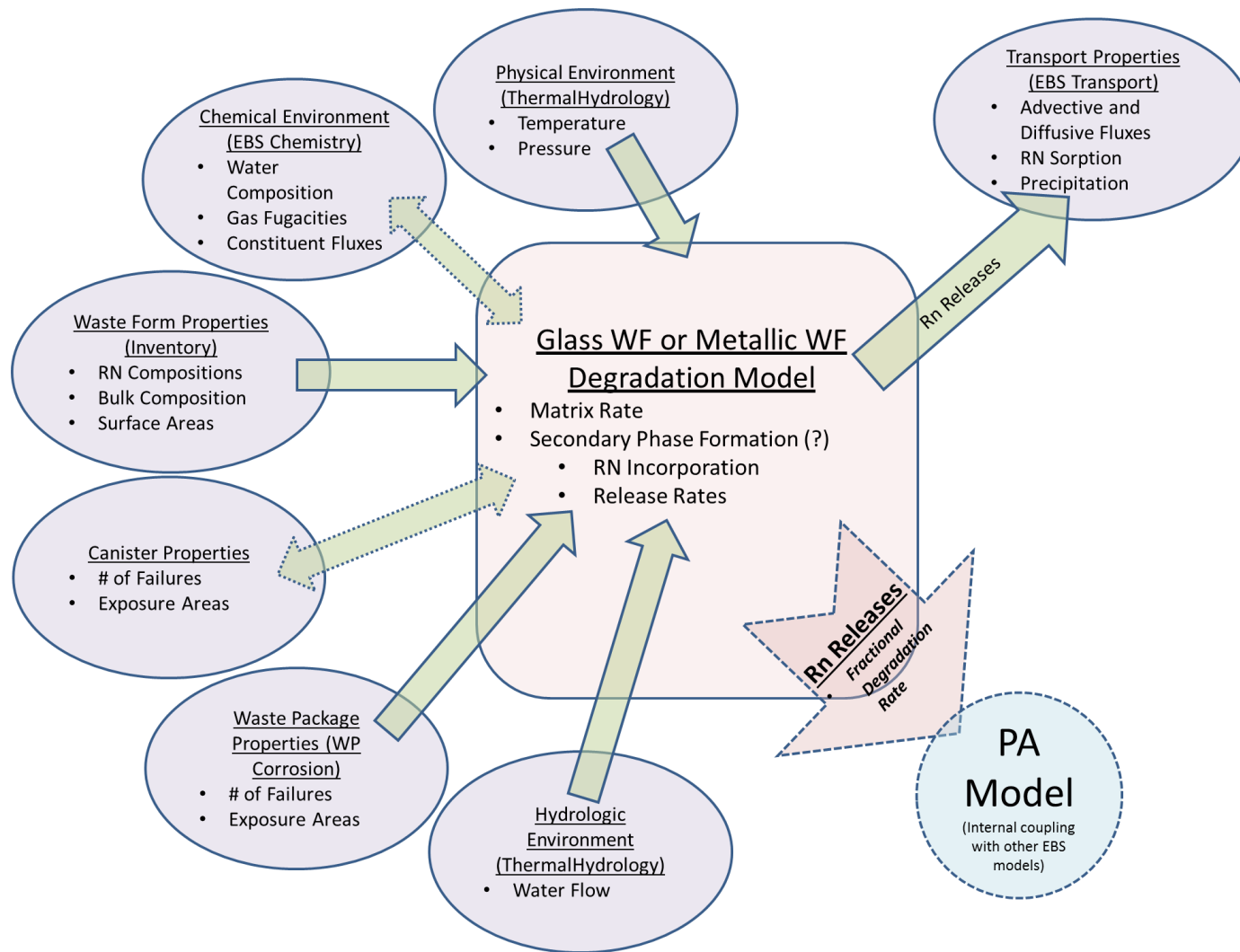


Figure 4.2-1. Schematic diagram showing the range of possible couplings between the glass waste form, or metallic waste form, degradation model and the other models within the engineered barrier system (EBS) portion of the PA Model. Primary hand-offs/connections are shown with single-headed arrows. Note that initial connection into the PA Model would be expected to be simply via the fractional degradation rate of the waste form. Potential two-way hand offs (i.e., couplings) are shown with double-headed arrows

### 4.3 References

- Clayton D., Freeze, G., Hadgu, T., Hardin, E., Lee, J., Prouty, J., Rogers, R., Nutt, W. M., Birkholzer, J., Liu, H.H., Zheng, L., and Chu, S., 2011, Generic Disposal System Modeling—Fiscal Year 2011 Progress Report, FCRD-USED-2011-000184, pp. 443.
- Freeze, G. and Vaughn, P., 2012, Performance Assessment Framework Requirements for Advanced Disposal System Modeling, FCRD-UFD-2012-000227 (M3FT-12SN0808062), U.S. Department of Energy, Office of Nuclear Energy, Used Fuel Disposition Campaign, Washington, D.C.
- Freeze, G., W.P. Gardner, P. Vaughn, S.D. Sevougian, P. Mariner, V. Mousseau, and G. Hammond, 2013, Enhancements to Generic Disposal System Modeling Capabilities, FCRD-UFD-2014-000062, SAND2013-10532P, November 2013.
- Sassani, D.C., Jové Colón, J. C., Weck, P., Jerden, J. L., Jr., Frey, K. E., Cruse, T., Ebert, W. L., Buck, E. C., Wittman, R. S., Skomurski, F. N., Cantrell, K. J., McNamara, B. K., and Soderquist, C. Z., 2012, Integration of EBS Models with Generic Disposal System Models, U.S. Department of Energy, Used Fuel Disposition Campaign milestone report: M2FT-12SN0806062, September, 7 2012
- Sassani, D. C., Jové-Colón, C. F., and Weck, P. F., 2013a, “Integrating Used Fuel Degradation Models into Generic Performance Assessment” for the ANS 2013 International High-level Radioactive Waste Management Conference, April 28 – May 3, 2013, Albuquerque, NM.
- Sassani, D.C., Jove-colon, C.F., Weck, P.F., Jerden, J. L., Jr., Frey, K. E., Cruse, T., Ebert, W. L., Buck, E. C., and Wittman, R. S., 2013b, Used Fuel Degradation: Experimental and Modeling Report, FCRD-UFD-2013-000404, SAND2013- 9077P, October 17, 2013.
- SNL (Sandia National Laboratories) 2014. Evaluation of Options for Permanent Geologic Disposal of Used Nuclear Fuel and High-Level Radioactive Waste Inventory in Support of a Comprehensive National Nuclear Fuel Cycle Strategy. FCRD-UFD-2013-000371. SAND2014-0187P; SAND2014-0189P. Revision 1. Albuquerque, New Mexico: Sandia National Laboratories, April 15, 2014.
- Yu, L., Weetjens, E., Vietor, T., and Hart, J., 2010, Integration of TIMODAZ within the safety case and recommendations for repository design (D14), Final Report of WP6, European Commission Euratom Research and Training Programme on Nuclear Energy, 48 pp.

## 5. Summary and Conclusions

These modeling activities focused on the degradation rates of the high-level waste glass waste form and of the metallic (Fe-Tc alloy) waste form were executed within the UFD Campaign as part of a larger effort across the Materials Recovery and Waste Forms (MRWF) Campaign (formerly the Separations and Waste Forms Campaign, in which these activities previously were executed). The management and integration of these glass and metallic waste form modeling activities within the UFD Campaign was performed within the Disposal Research Engineered Materials Performance (DREMP) technical work area (control account). This waste form degradation work was managed and directed within work package FT-14SN080405 and this report fulfills milestone M2FT-14SN0804051 and covers waste form degradation activities in this control account. Achieving a high degree of integration both within the set of activities in the UFD Campaign, as well as across the UFD and MRWF Campaigns, for these technical topics was a larger challenge than solely within-campaign integration. However, the efforts by program management and all the investigators involved across these two campaigns have led to an increased awareness of technical interfaces and development across both these campaigns. This enhanced level of integration should facilitate incorporation of waste form degradation models for glass and metallic waste forms being developed in the MRWF Campaign for use in PA Models developed within the UFD Campaign.

### 5.1 Glass Waste Form Modeling Activities

The activities for glass degradation modeling encompass scales from the molecular- to the macro-scale for evaluating the breakdown of the glass phase, the development of silica gel at the glass-water interface, and the formation of alteration phases at this interface. These activities are evaluating several different rate laws that have been proposed for these processes based on fitting experimental data and that are currently used to predict corrosion rates into the distant future in repository settings. In general, these rate laws base their limiting rates on either a transition state theory (TST) dissolution affinity rate law or on the rate of mass transport through the amorphous layers formed at the glass-water interface. The lack of a consensus on an integrated quantitative representation of the rate-limiting processes for nuclear waste glass degradation initiated an effort to evaluate several processes of glass degradation in greater detail to enhance the technical bases for glass degradation rate models used in performance assessment of geologic disposal systems.

Molecular-scale first-principles modeling work on glass degradation mechanisms (Section 2.1) focuses on calculating the energies and barriers for bond-breaking reactions involving Si-O and B-O bonds at the glass surface. This research effort is designed to develop a more complete constitutive expression for the TST affinity rates based on multicomponent glass surface structure. Reaction barriers and energies for dissolution reactions on protonated, neutral, and deprotonated sites on sodium borosilicate glass surfaces were calculated and reported. For these simple three component glasses ( $\text{Na}_2\text{O} - \text{B}_2\text{O}_3 - \text{SiO}_2$ ), there are only two framework metals (B and Si). However, there are numerous reactions occurring on the surface with different activation barriers and reaction energies depending on the bond saturation state of the B (or Si) atom being removed from the surface, the type and saturation state of the neighboring metal (B or Si) bonded to the same bridging oxygen atom, and the protonation state of the bridging oxygen. The tables in Section 2.1 report energies for 22 different surface reactions that play a role in  $\text{Na}_2\text{O}-\text{B}_2\text{O}_3-\text{SiO}_2$  glass dissolution.

Discrepancies in bulk reaction energetics exist in the literature because simple affinity rate laws have been derived from bulk experimental dissolution data, even though different reactions may become rate-limiting for different glass or solution compositions. Using the work done here, subsequent research would include incorporating the calculated energy barriers and reaction energies into Kinetic Monte Carlo simulations of glass dissolution (or into the kinetic-microscopic-continuum model—see Section 2.2, and below) and sensitivity analyses to determine the rate-limiting bond-breaking steps under different system

conditions. In addition, building on the methodology developed here for a simple glass composition, expanding to include more of the major components in nuclear waste glass would be a valuable next step.

Nano-continuum ( $K\mu C$ ) modeling (Section 2.2) focuses on reproducing the nanoscale concentration profiles at the glass-water interface observed for a 25-year degradation experiment for the French SON68 glass. A high resolution model of that interface is developed with a constant grid spacing of 1 nanometer and a continuum model assumption. Although using a continuum model at nanometer scale is an approximation, it is the only approach available that includes multicomponent chemistry with precipitation and dissolution at this scale. Using this model the compositional gradients reproduced are: (1) Li release from the glass; (2) hydrogen migration into the glass (glass hydration) from the solution and (3) boron release from the glass. The Li and H concentrations exhibit 15 nm wide gradients between the pristine glass and the hydrated glass layer that are anti-correlated (i.e., an interdiffusion layer). The B concentration defines a sharp profile ( $\sim 3$  nm width) located just outside (away from the pristine glass interface) of the Li/H interdiffusion layer. The  $K\mu C$  model incorporates the possible rate-controlling processes of (a) diffusion-limited glass corrosion, (b) affinity-controlled hydrolysis reactions based on TST rate laws, and (c) precipitation of secondary phases.

A key aspect of the model is that the primary dissolution reaction of the fresh glass is assumed to follow an affinity rate law, with a cubic dependence on the solution saturation state with amorphous silica. This approach reproduced the sharpness of the B release front and the position of the B release front outside of the Li-H interdiffusion front. The simulations predict a linear rate of front propagation over time once the initial period has passed. Sensitivity analyses with the  $K\mu C$  model indicate that the amount of glass degradation that occurs is dependent on the fluid compositional boundary condition. Virtually no corrosion of the glass was calculated for amorphous silica saturated fluid (1936  $\mu M$ ) as the boundary condition versus the 10  $\mu M$  composition that results in much larger glass degradation.

In summary, the rate-limiting step for the experiment on SON68 glass corrosion appears to be the rate of diffusion of H (via water) into the pristine glass. An explicit Passive Reactive Interface (PRI) zone is not required. The linear rate that is predicted by the simulations follows from the fact that the amorphous silica gel corrosion layer that forms on the glass is not itself a diffusion barrier, consistent with the constant width of the layer. The glass corrosion model proposed is one in which the rate of dissolution depends on the rate of diffusion of hydrogen for glass hydration. In addition, as solution dissolved silica concentrations rise to near equilibrium with respect to amorphous silica, glass corrosion rates should decrease dramatically.

The Glass Corrosion Modeling Tool (GCMT; Section 2.3) has been developed for several purposes: (1) to examine efficiently the goodness of fit of a variety of glass corrosion models to specific experimental datasets, (2) to provide easy access and evaluation of an extensive database of glass alteration experimental results (consisting primarily of single pass flow through tests—i.e., ALTGLASS), with the potential to use this database to derive new glass dissolution constitutive equations, and (3) to provide a platform for the newly developed Diffusive Chemical Reaction (DRCx) model. The DRCx model, like the  $K\mu C$  model, is intended to be used to evaluate the detailed concentration profiles dataset from TOF-SIMS and APT analyses of glass corrosion interfaces. Within the GCMT, the user can choose to implement various other models such as the Aagaard-Helgeson (AH) model with residual rate, the Grambow-Muller (GM) model and the Glass Reactivity with Allowance for the Alteration Layer (GRAAL) model. The ALTGLASS datasets could be used within the GCMT to develop new glass degradation constitutive equations. To facilitate this usage, a graphical user interface has been constructed in the GCMT to make selection of datasets from the ALTGLASS database a streamlined and transparent process.

Initial GCMT model results using the DRCx model show that, for the TOF-SIMS data on SON68 glass degradation, the DRCx model adequately describes Na, Si, and B profiles but is less useful for describing the behavior of Al and Li. Two detailed examples of using the GCMT to evaluate glass corrosion datasets

have been generated. In the first example, the long-term residual rate corrosion of low-activity waste (LAW) glass are analyzed using the AH model and optimize parameters are provided. In the second example, time dependent species concentrations for SON68 glass degradation are analyzed with the GRAAL model. Although the GRAAL model does not provide a close approximation to the specific dataset used in the example, it has been used to closely reproduce other relevant experimental data. The GCMT provides a flexible method to evaluate several different models using a large range of data reported for experiments on glass corrosion.

## 5.2 Metallic Waste Form Modeling Activities

A multistep conceptual corrosion model for the release of Tc from any candidate alloy (e.g., Fe-Tc) waste form is described (Section 3.1). There are three viable rate-limiting mechanisms for Tc release: (1) cation vacancy annihilation at the metal/oxide interface, (2) transport of Tc through the oxide film, and (3) dissolution of Tc at the oxide/environment interface. Initial molecular-scale first-principles modeling has focused on applying DFT calculations to investigate the relative stability of different Fe-Tc oxides and the diffusion of Tc incorporated into vacancy defect sites in a range of Fe-oxide crystals. To validate the DFT approach used, the relative stabilities of Tc oxides were calculated and predicted properties were compared to measured values. The two oxides ( $\text{TcO}_2$  and  $\text{Tc}_2\text{O}_7$ ) calculated to be the most stable are the only two Tc oxides that have been synthesized and characterized experimentally. Calculated lattice constants, crystal formation energies, and bulk moduli compared reasonably well to experimental measurements. To evaluate potential behavior of Tc in oxide films of a corroding alloy, models of Fe-oxide structures were designed with care to incorporate the magnetic ordering of the Fe atoms. Calculations of the energies for Tc incorporation into simple Fe vacancies in three Fe-oxide crystal structures were completed. In addition, for the first time, the migration energy barrier for Tc diffusion along one channel in  $\alpha\text{-Fe}_2\text{O}_3$  (hematite) was calculated. The calculated results show that Tc incorporation into FeO is endothermic, Tc incorporation into  $\alpha\text{-Fe}_2\text{O}_3$  is energetically preferred, and the preference for Tc incorporation into  $\text{Fe}_3\text{O}_4$  is site dependent. The energy barrier for Tc migration via vacancies is calculated to be larger than for Fe, suggesting slower Tc diffusion than Fe diffusion within hematite. Additional calculations evaluated energetics of Tc incorporation into three spinel phases (potential waste forms) of different crystal structures ( $\text{Fe}_3\text{O}_4$ ,  $\text{CaFe}_2\text{O}_4$ , and  $\text{YFe}_2\text{O}_4$ ) and predict that magnetite is the most stable form to host Tc atoms with concentrations of up to 33%, forming a  $\text{TcFe}_2\text{O}_4$  spinel.

Integrating modeling efforts focused on larger-scale simulations using kinetic Monte Carlo and force field methods. Preliminary results suggest that the corrosion morphologies and rates would be different for Tc-Fe, Tc-Mo, and Tc-Ni candidate alloy waste forms. The rate of Tc-Fe corrosion decreases with increasing Tc concentration up to 10%. Finally, integrated with the modeling effort, electrochemical corrosion experimental studies have been performed on Tc metal in pH 3.2  $\text{H}_2\text{SO}_4$  solutions. Several experiments were performed to determine if a passivating film forms on Tc metal, but so far all measurements suggest the films formed are not passivating.

Additional molecular-scale first-principles modeling work (Section 3.2) is focused on investigating the incorporation of Tc into an iron oxyhydroxide (goethite,  $\alpha\text{-FeOOH}$ ) phase that could represent oxidized corrosion products of the metallic waste form or those of the waste package internal components. These calculations also constrain Tc affinity for bulk goethite versus goethite surface sites, and determining Tc stability on (in) goethite in the presence of adsorbates such as water, oxygen, hydrogen and hydrogen peroxide. The method used to date is unrestricted Hartree Fock (UHF), which should successfully capture the localized electron behavior in goethite. Detailed research has been performed to establish appropriate calculation parameters, assure that the goethite structure used is antiferromagnetic, and create supercells that allow Tc incorporation at experimentally-relevant levels. Three different Tc incorporation schemes are proposed: (1) coupled Tc(IV)/Fe(II) substitution for two lattice Fe(III), (2) Tc(IV)

substitution of one Fe(III) and one H<sup>+</sup> balance, and (3) interstitial Tc(IV) addition and removal of four nearest neighbor H<sup>+</sup> for charge balance. The energetics for these three schemes is under investigation.

### **5.3 Waste Form Model Integration into PA Models**

Development of an idealized strategy for integrating glass and metallic waste forms degradation process models with PA model approaches to analyze generic disposal environments includes parametric connections/couplings needed for direct incorporation into PA models (Section 4). This is based in the methodology developed for integration of the used fuel degradation model into the PA model. The approach begins with basic physical parameter couplings from the PA model with fractional degradation rate feedback to the PA model. However, it is an ongoing task to delineate in the implementation specifics of how these process models will couple to other EBS process submodels (e.g., chemical environment evolution, radionuclide transport) within the PA model for generic disposal environments and evaluations of the safety case. Additional more idealized coupling options are outlined that have fewer open constraints on implementation specifics and provide flexible options for incorporating additional coupling detail as needed.